Partially Filled Radial Power Combiner with Port Isolation

by

Hendrik J. du Toit

Dissertation presented for the degree of Doctor of Philosophy in Electronic Engineering in the Faculty of Engineering at Stellenbosch University

Supervisor: Prof. D.I.L de Villiers

March 2020

Declaration

By submitting this dissertation electronically, I declare that the entirety of the work contained therein is my own, original work, that I am the sole author thereof (save to the extent explicitly otherwise stated), that reproduction and publication thereof by Stellenbosch University will not infringe any third party rights and that I have not previously in its entirety or in part submitted it for obtaining any qualification.

Date: .....March 2020.....

Abstract

Keywords - radial transmission line, power combiner, radial power combiner, passive isolation, graceful degradation

This dissertation documents the design and testing of a partially filled radial power combiner with a passive peripheral isolation network, at 4 GHz. A review of available literature on power combiners highlights the advantages of radial combiners. The theory of radial transmission lines is presented, and such a power combiner without an isolation network is designed first. A printed circuit board is utilised at the bottom of the radial line cavity to aid in transitions at the central and peripheral ports. The centre transition into a coaxial connector consists of a shunt capacitance realised by an annular ring on the PCB. This also acts as a base for the coaxial connector.

At the periphery, inductive posts couple energy from the radial cavity into microstrip lines. This approach is taken for compatibility with the ensuing planar passive isolation network at the peripheral ports. Broadside hybrid quadrature couplers are arranged around two almost identical radial combiners to implement the isolation.

Testing the non-isolated combiner yielded an input reflection level at the centre ports of less than -15 dB over 20% relative bandwidth. Amplitude and phase balances were also close to other designs in literature. These parameters are ± 0.3 dB and $\pm 2.5^{\circ}$, respectively.

A passive isolation network is then added. This structure makes use of two back-to-back 16-way radial combiners and the aforementioned couplers to electrically isolate the peripheral input ports of the complete device. With the addition of this isolation network, the central input reflection level was reduced to at most -18 dB across more than 45% of the fractional bandwidth. This is a wider bandwidth than many radial combiners combiners found in literature. Combiners that are significantly better matched are mostly complex coaxial and conical combiners.

The isolated combiner showed some improvement in peripheral signal balances over a 40% bandwidth as well. In this range, the amplitudes are within ± 0.2 dB, and phases within $\pm 2^{\circ}$ of each other. This is on par with most other axially symmetric combiners considered.

This is also the first axially symmetric combiner that incorporates a passive

isolation network among the peripheral ports. As such, the average isolation performance is significantly better than other axially symmetric combiners described in literature. Isolation was measured among all the peripheral ports, and an average calculated for each set of electrically symmetric peripheral ports. The least isolated set shows a minimum isolation of 21.8 dB across the analysed 50% bandwidth, and this threshold increases to 27 dB over a narrower 40% bandwidth. The graceful degradation properties of the structure, analysed by simulation, show that it degrades as well as theory predicts when a number of inputs fail.

The complete structure, however, incurs slightly more transmission losses than axially symmetric combiners are known for. Much of this is attributed to the coaxial links to the external isolation quadrature coupler between the centre ports of the radial structures.

It was necessary to tune the prototypes of both iterations to achieve satisfactory input reflection performance. Using an improved centre transition should further improve the transmission loss of the isolated combiner, since much of the energy that would be reflected is redirected into the isolation loads and counted loss.

Opsomming

Sleutelwoorde - radiale transmissielyn, drywingkombineerder, radiale drywingkombineerder, isolasie, grasieuse degradering

Hierdie proefskrif beskryf die ontwerp en toets van 'n gedeeltelik gevulde radiale kombineerder met 'n passiewe isolasie netwerk, by 4 GHz. Die voordele van radiale kombineerders blyk uit die oorsig van beskikbare literatuur. Na 'n uitleg van die betrokke teorie word 'n poging aangewend om eerstens 'n radiale kombineerder te ontwerp sonder die isolasie netwerk. Die middel konnektor termineer op 'n koper ring, uitgeëts op 'n dielektriese substraat.

Daar word gebruik gemaak van induktiewe penne en mikrostrook lyne by die poorte aan die omtrek van die kombineerder. Sodoende is die kombineer gepas vir uitbreiding met 'n planêre isolasie netwerk. Díe netwerk bestaan uit 'n rangskikking van 3-dB breësy kwadratuurkoppelaars wat twee eenderse radiale kombineerders aanmekaar haak.

Meetresultate van die nie-geïsoleerde kombineerder het 'n intreeweerkaatskoe"ffisient by die sentrale poort van laer as -15 dB opgelewer, oor 'n relatiewe bandwydte van 20%. Amplitude- en fasebalans metings plaas die seine by die periferale poorte binne ± 0.3 dB en $\pm 2.5^\circ$ van mekaar.

Die toevoeging van die isolasie netwerk het gelei na 'n middelpoort weerkaatskoe"ffisient onder -18 dB oor meer as 45% bandwydte. Dit is 'n wyer band as meeste soorgelyke, veral radiale, ontwerpe. Strukture wat aansienlike beter bandwydtes toon is die meer ingewikkelde koaksiale en koniese kombineerders. Daarby het die periferale seinbalans ook verbeter na ± 0.2 dB en $\pm 2^\circ$ tussen mekaar, oor 40% relatiewe bandwydte.

Hierdie is die eerste radiale kombineerder wat 'n passiewe isolasie netwerk het om periferale poorte van mekaar te isoleer. Dus is die gemiddelde isolasie tussen periferale poorte merkwaardig. Die koppeling tussen al die periferale poorte is gemeet en 'n gemiddeld is bereken vir elke stel van elektries simmetriese poorte. Analiese van hierdie gemiddeldes dui op 'n isolasie van minstens 21.8 dB tussen enige kombinasie periferale poorte. Hierdie isolasievlak strek oor die hele 50% bandwydte wat analiseer is. In die 40% band van 3 - 4.6 GHz is die isolasie hoër as 27 dB. Simulasies van die nuwe kombineer in 'n stelsel met foutiewe intree poorte dui op grasieuse degradering gelykstaande aan die beste geval voorspel in teorie.

Die volledige toestel toon wel effense hoër transmissie verliese as ander aksiaal simmetriese kombineerders. Analiese van die metings ken die meerderheid van die verliese toe aan die koaksiale lyne wat die eksterne kwadratuurkoppelaar tussen die middelpunt poorte verbind.

Dit was nodig om beide iterasies te verstel sodat die resultate voldoende is. As die middel-oorgange verbeter word kan dit ook die transmissie verliese verminder. Energie wat tans weerkaats is deur die oorgange, word absorbeer in die isolasie laste en is dan gereken as verliese.

Acknowledgements

Without the continual support from those around me, this work would not have been possible. My heartfelt gratitude to those involved:

- My supervisor, Prof. Dirk de Villiers (and Dr. Ryno Beyers in the early days), for endless insight and support.
- Computer Simulation Technology and National Instruments for the use of their software.
- Wessel Croukamp and Gift Lecholo for the invaluable design advice and manufacturing of the prototypes.
- The team at TraX Interconnect for assisting with the design and manufacture of the PCB components.
- Anneke Bester for assisting with the RF measurements of the prototypes.
- My parents for their wisdom, phone calls, and the grit to get through this project.
- The Fourie's for giving me a home away from home – warm hearts, bike rides, cappuccinos and a fire place.
- My love Yadah for always having more faith in me than I did in myself.
- My friends, ever ready to make me forget about crashing simulations.
- Everyone else that offered motivation and support.

Contents

List of Figures

List of Tables

Chapter 1

Introduction

Recent decades witnessed high frequency semi-conductor technologies develop rapidly. Solid state amplifiers have increased in power handling with better cooling and improved efficiency, while continually shrinking in size. These characteristics make semi-conductor amplifiers an attractive alternative to the classic travelling wave tube (TWT) amplifier in high frequency applications. A notable disadvantage of the latter is that the amplification stages are spread along the propagation direction, which leads to a large structure for numerous stages. Catastrophic failure also occurs when any of the amplifier stages break down, since the TWT becomes wholly inoperative.

At high frequencies and power, though, solid state amplifiers do exhibit their own set of drawbacks. Amplifiers tailored to overcome, for example, the lower efficiency or higher noise levels at high frequencies are expensive, and sometimes bulky. As such, it seldom occurs that a single solid state amplifier package drives high frequency systems at higher power levels. Alternative methods are therefore sought to increase the power handling of an amplifier system, without significantly hampering other performance metrics.

Power combiners have found a very practical application in this regard. Signals from a number of lower power, well-performing amplifiers can be combined to produce a desired output power. Many amplification systems that utilise power combiners also allow for graceful degradation. This allows the system to still operate at a practical level when some of its amplifiers fail, which is a significant advantage over the TWT.

Most power combiners are also reciprocal. This allows for them to used as power dividers as well. Applications of this nature range from antenna arrays to splitting signals for amplification as described above.

1.1 Overview of Power Combiner Designs

Given the important role of power dividers in modern high power microwave devices, its development has received much attention over the years. A well-

known design is the resistive Wilkinson divider [1]. A network of resistors absorbs asymmetric modes among the input ports, which offers perfect isolation among said ports, at least in the ideal circuit model. This technique can be implemented as a planar structure [2] for a maximum of three input ports. For more input ports, connecting the isolating resistors among ports make it impossible to be implemented on a single layer printed circuit board (PCB).

The Gysel divider in [3] brought significant improvement to the design. Isolation resistors in the updated version can be relocated via transmission lines. In doing so, termination loads could replace the resistors. This resulted in better heat and power dissipation termination options. These devices tend to escalate in complexity as the number of combining ways increase, and as such, current literature documents at most $N = 8$ way Gysel combiners [4], [5]. Numerous designs of $N \leq 4$ exist, however [6]–[9].

Due to the simplicity and economy of planar technology, some designs focus on implementing more input ports on a single layer. A popular method to accommodate more input ports is to use corporate or chain type combiners. These typically have multiple combining stages [10] or sequentially add input ports along the same dimension [11]. An issue with these designs is that their size grow substantially as the number of input ports increases. This commonly results in higher insertion losses due to the longer signal path, usually inside a lossy dielectric.

As such, more alternatives exist that aim to limit the combiner size growth, and consequently reduce insertion loss. One of these is the so-called superplanar N-way design in [12]. The combining stage is a parallel plate transmission line section, with the inputs along one end, and the output at the opposite end. The inputs and outputs are 50 Ω microstrip transmission lines. A noticeable caveat is the narrow operating bandwidth of this design. The simulated reflection coefficient at the combining port is better than -10 dB over an estimated fractional bandwidth of only 6% at 1.33 GHz. This is quite narrow compared to other PCB based work [13].

Another important metric is the phase balance among input signals. This affects how efficiently the signals are combined at the output. Due to the limited multiway symmetry achievable in its geometry, the phase balance in [12] is 5°. Axially symmetric combiners, on the other hand, achieve a phase balance of close to $\pm$ 1°[13], [14]. In this regard, axially symmetric combiners are in general superior to other form factors. These combiners have the combining port in the centre of some axially symmetric transmission line, and the inputs are evenly spaced in a circular fashion around the periphery of the combiner. The signal paths are shorter and the accompanying transmission losses are generally lower in axially symmetric combiners than in corporate N-way combiners for a large number of ports ($N > 8$) [14].

The examples so far have all been planar implementations of the various combiner types. A common problem with them is that the dielectric in the combiner introduces a transmission loss. This loss is dissipated as heat and

thereby limits the average power handling of the structure. Some application require lower average power handling, but higher peak power, and in these cases the higher breakdown strength of dielectrics (compared to air) is an advantage. For high average power applications, it is however favourable to use air-filled structures.

Axially symmetric combiners are commonly implemented as air-filled cavities as well. These are, however, quite complex structures that require precise manufacturing. One such combiner type is the coaxial combiner, wherein an oversized coaxial transmission line section is used to create the combining structure. The input ports are located around the outer conductor of the coaxial line. Early versions of this combiner were bulky, and significant work has been done to reduce the size of these combiners [15]. One such combiner is able to achieve an output reflection of less than -15 dB, over a relative bandwidth of 130% [16]. Another design [17] claiming a coaxial form presents simulation results with the same combining port reflection over a 100% bandwidth. It must be noted, however, that the geometry of the latter appears to be more like that of conical and radial line combiners.

Conical and radial line combiners are quite similar in form, but have important differences. For a constant angle between the conical faces, conical lines have a constant characteristic impedance along the radial direction . This allows predictable behaviour that is largely independent of wavelength. As such, these combiners can also be well-matched to input and output ports over a significant bandwidth. The example in [18] shows a maximum return loss at the centre port of -14.7 dB, over a 74% fractional bandwidth. The major drawback of these combiners are the tight manufacturing tolerances that relies on accurate CNC machining, which typically leads to escalated manufacturing costs.

Radial lines can be of a simpler geometry, but are then strongly dependent on wavelength. Most common radial combiners have parallel plate radial line sections as the main combining structure. These types of lines produce a significant reactive input impedance at the centre port. As such, the bandwidth of these combiners are limited. They are nonetheless still practical, with reflected power at the centre port less than -15 dB over approximately 25% fractional bandwidth [14], [19].

Another limitation of most of these reactive axially symmetric combiners is that their isolation performance is lacking. If the peripheral ports are not excited close to identically, more than -10 dB of energy can be coupled between peripheral ports across the operational bandwidth [18]. It therefore leaves some room for improvement on these types of combiners.

As an alternative to adding isolation resistors or external circulators to the reactive combiner, isolation can be improved through phase cancellation using hybrid quadrature couplers. Moving away from axially symmetric devices, the design in [20] exploits the quadrature nature of the Riblet coupler [21] in this way to achieve better isolation. The couplers are chained to achieve phase

cancellation for reflected asymmetric modes at input ports. Comparatively good isolation (below -20 dB) among input ports is a direct result of this.

A similar, but simpler, planar isolation network was developed earlier in [22]. This technique theoretically allows for perfect isolation among the input ports. Instead of the quadrature couplers realising the power combination, it has two identical N-way power combiners. The hybrid quadrature couplers are only added to implement isolation among the input ports. This isolation method has, however, not been demonstrated for combiners with a large number of combining ports ($N > 8$). It has also not been implemented using axially symmetric combiners.

To prove the capability of this network, a 4-way planar combiner was constructed and tested [22]. The broadside coupled quadrature couplers used in [23] were adapted. Both these designs [22], [23] were able to achieve a relative bandwidth of more than 50%, which make these couplers an attractive option for wideband operation. The isolation in [22] is then shown to be at least 25 dB over a 50% bandwidth. It is also noted that this technique maintains the reciprocity of the N-way combiners in the design, which is important in some applications.

1.2 Contributions

A fully isolated reactive radial power combiner is presented in this dissertation. First, a 16-way non-isolated partially-filled radial combiner is designed and built to test the approach used for the underlying N-way sections needed for the complete isolated combiner. This simple combiner showed symmetric output port reflection below -15 dB over 20% relative bandwidth at 4 GHz. Measured peripheral (input) signal balances are ± 0.3 dB and $\pm 2.5^{\circ}$, and total insertion loss lower than 0.5 dB. This version showed asymmetric input reflection below -5 dB and isolation just better than 10 dB.

A second version was then designed to include an integrated isolation network. The fully isolated prototype showed an output reflection of less than -18 dB over more than 40% bandwidth. The input port balance also showed a slight improvement to ± 0.2 dB and $\pm 2^{\circ}$. Crucial metrics for graceful degradation were vastly improved. Isolation among the input ports is more than 25 dB across 45% bandwidth, and the asymmetric input reflection is below -15 dB beyond the 50% bandwidth analysed. This is a significant improvement over the non-isolated combiner. Since the whole structure is larger and more complex than the first, the insertion loss is slightly higher at 0.8 dB across 25% bandwidth.

The main contributions of this dissertations are therefore

- The implementation of full input port isolation in an axially symmetric combiner [24].

- A new partially-filled radial combiner [25].

1.3 Dissertation Outline

Some practical aspects of radial combiners in literature and the necessary radial waveguide theory is considered in Chapter 2. Radial transmission line equations are derived and manipulated into practical design equations. From those derivations, Chapter 3 follows with the calculation of design parameters of the radial line section. Also covered in this chapter are the simulation analysis and prototype testing of the non-isolated partially filled radial combiner.

The preliminary design of the hybrid quadrature coupler of the peripheral isolation network starts in Chapter 4. These are then integrated with the radial combiner design, and the 3D simulation analysis of this process is documented here as well. Ending off Chapter 4 is the manufacture and measurement results of the isolated radial combiner.

A comprehensive simulation analysis of the graceful degradation performance is presented in Chapter 5. The dissertation concludes with Chapter 6, wherein the obtained results are discussed in the context of results from literature. Some possibilities for future work is also suggested.

Chapter 2

Background

From this point, radial combiners are considered in more detail. Some examples are presented to highlight important design points common to many radial combiners. Specific points stressed commonly in literature are the designs for the central port and peripheral ports. Another metric occasionally quoted, but specified even more seldom, is the isolation among peripheral ports. The first part of this chapter gives some information on the different dielectric media often used in radial combiners. After that, some implementations of the center and peripheral the port coupling are compared. Isolation methods applicable to radial combiners are then considered, and a detailed discussion is presented on the proposed method. In the last part, some radial transmission line theory is presented. Starting at the field equations, the derivation will follow through to useful design equations.

2.1 Dielectric Media

An early design choice regarding radial combiners is the dielectric medium. Most combiners are designed around either an air cavity, or a planar dielectric substrate. One main advantage of air cavities is higher average power handling [18], [26]–[28] compared to other media. Along with that, air causes less signal loss than other dielectric materials.

PCB based combiners, on the other hand, are usually simpler to manufacture. These combiners also integrate more easily into larger systems, due to ability to add other surface-mount components directly at the combiner [14].

The choice of medium then usually dictates the methods used to couple energy through the combiner. Some designs available in literature are compared here. These designed are compared based on the coupling methods used at the centre and the periphery, respectively, of the combiner.

2.2 Centre Port Designs

Due to compatible geometry, an air cavity radial combiner generally transitions to a coaxial line at its centre. A well known approach to this transition is to enter the radial line at a larger radius than the inner conductor of the coaxial line. It was found that this transition geometry is impedance matched over a wider frequency band for some cases [29]. Common implementations of these combiners simply have a step in the center conductor of the coaxial line, as shown in Figure 2.1(a). The capacitance of the step in radius compensates for inductance of the centre pin. This approach offers nearly 50% relative bandwidth, which is an improvement over transitions that kept the centre conductor homogeneous. The stepped coaxial transition is also not limited to air based combiners, but can be used in combiner designs with dielectric substrates [14], [30]. It entails the same idea as shown in Figure 2.1(a), except that the radial line exists in some PCB that is appropriately mated to the centre pin of the coaxial line.

Another approach is make use of a conical section in the transition, as shown in Figure 2.1(b). This also creates a relatively wideband transition. A center port reflection coefficient of less than -15 dB can be expected over a fractional bandwidth of at least 50% [19], [26].

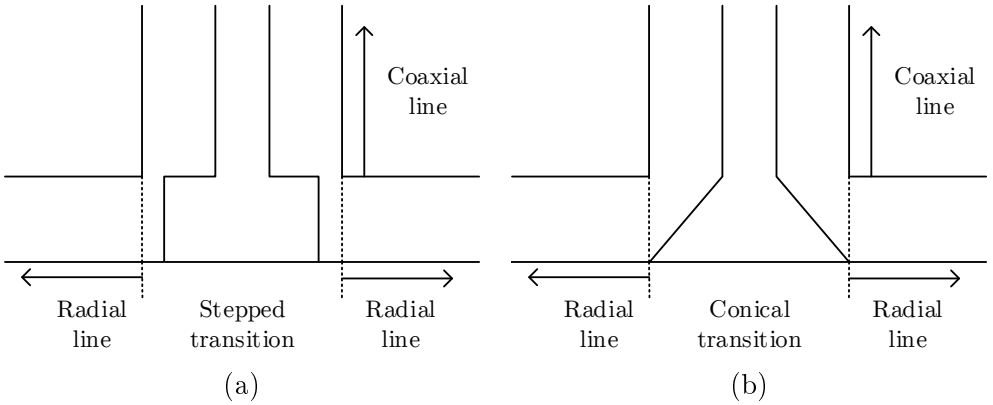

Figure 2.1: Cross-sections of the basic geometry of (a) a stepped inner conductor, and (b) a conical line transition from an air cavity radial combiner to a coaxial transmission line.

Moving on to substrate based radial combiner designs. An issue particular to these designs is the low characteristic impedance at the radial line center. This due to the small spacing between the radial combiner plates (as detailed in Section 2.5).

Where the coaxial lines contained the characteristic impedance matching in the previous designs, others incorporate this into the radial line section. One example employs a set of higher impedance microstrip lines running from the centre into the more typical radial line section [13]. Figure 2.2(a) shows this

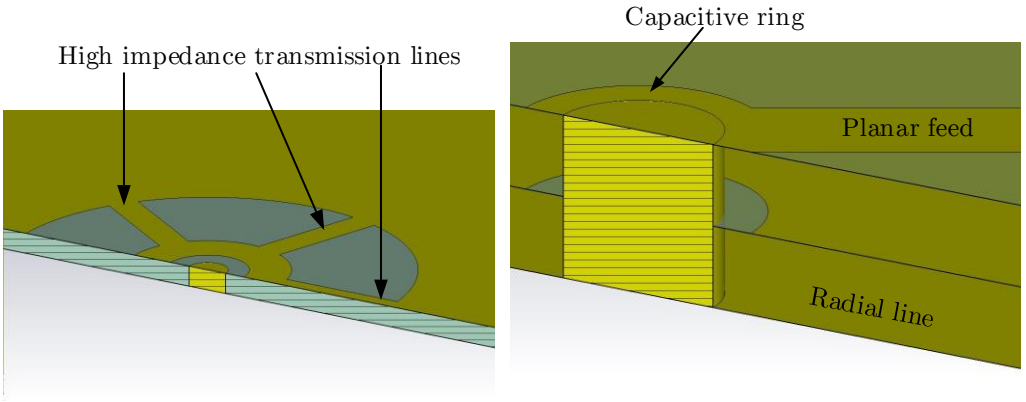

(a) (b)

Figure 2.2: Illustration of the geometry used in (a) a high impedance planar transition, and (b) a planar feed replacing the usual coaxial feed.

approach. The performance achieved for this design is a center port reflection coefficient below -10 dB, over a bandwidth of 29.4%

Substrate based combiners also allow some flexibility in matching the centre of the radial combiner to waveguides other than coaxial lines. In some of these cases, a planar transmission line is coupled to from the radial line using plated via holes [31], [32]. This principle, and the capacitive ring used to counteract the inductance of the via are illustrated in Figure 2.2(b). At the center port, these designs managed -15 dB reflection over estimated relative bandwidths of 15% and 19.4% , respectively.

2.3 Peripheral Port Designs

The peripheral ports are the multiple ports situated on, or close to, the outer edge of the radial line section. These ports are in most cases located in a circle concentric with the center port.

Radial combiners built around a PCB substrate in the radial line section are commonly terminated by splitting the radial line into multiple microstrip lines. This is illustrated in Figure 2.3(a). Depending on the application, these lines are then terminated in various ways. Some combiners include the surface mount active components as part of an amplifier system [14], [30] . Others are only run to the substrate edge where connectors can be added [13], [31].

The peripheral ports of radial combiners designed around an air cavity are more involved. There are some options the terminate the radial line in a number of waveguide apertures [26], [33]. An important aspect mentioned in those works, is that the waveguide ports must be carefully designed in order to

have the field modes in the peripheral waveguides match the mode propagating in the radial section. The reason for this is the TEM mode of the radial wave, discussed in Section 2.5, that needs to be matched to TE or TM modes in the peripheral waveguides.

A more common peripheral port transition in air filled radial combiners is a set of posts that run into coaxial transmission lines. Each post is connected to the inner conductor of the coaxial line, while the outer conductor and radial line plate are electrically continuous, as shown in Figure 2.3(b). Recent examples of this type of coupling [19], [34], [35] also add different types of capacitive loading to the posts. This aids the impedance matching of the transition over a wider bandwidth. Another, peripheral transition found on air cavity radial combiners makes use of microstrip probes mounted in the radial cavity [36], [37].

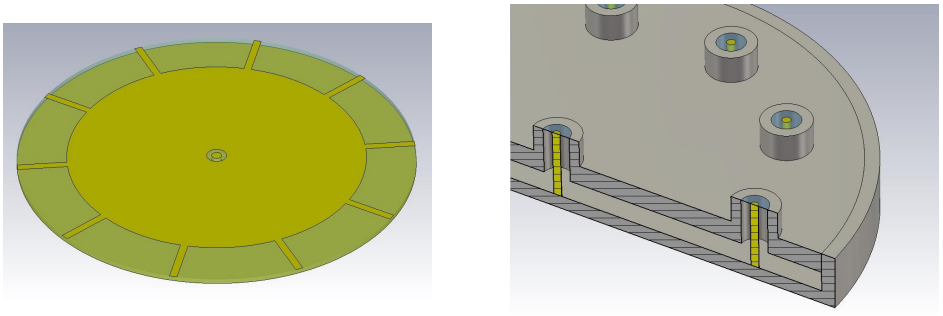

(a) (b)

Figure 2.3: Two common peripheral coupling designs for (a) planar and (b) cavity based radial combiners.

2.4 Isolation Techniques

Isolation makes an N-way combiner robust against asymmetric input signals. In the case of the radial combiner, these signals are expected when not all of the peripheral ports are excited identically. The ideal N-way combiner would offer perfect combination at the centre (port 1) of signals from ports 2 up to N+1. It would also prevent any other interaction among the peripheral ports 2 to N+1.

There are a number of challenges in efficiently isolating ports in a multi-way power combiner. Using ferrite isolators at each port, as in [19], adds significant bulk to the final device. Other common isolation implementations make use of resistors [1], [14], [30], [38] or resistive inserts [39], [40] to dissipate circumferential modes in the combiner. Possible limitations to these are the limited power handling due to the concentrated heat energy inside the device

once asymmetric modes are excited. A better solution would be to dissipate the unwanted energy outside the structure.

The chain of Riblet couplers presented in [20] is one example that functions in that way. The 90° phase difference between ports of each coupler cause cancellation of signals at certain ports, and combination at other ports. Selective measurement results are published in [41], and show isolation performance of better than 20 dB over approximately 25% bandwidth. This appears to be the isolation performance of one coupler, and not necessarily among input ports. Nonetheless, individual couplers must exhibit sufficient isolation for the complete network to function. The complexity of this device, however, restricts production to additive manufacturing. With that, the couplers also affect the N-way power combination, so this method can not be applied to another type of combiner. A more general approach is therefore investigated.

2.4.1 General N-way Port Isolation

The principle presented in [22] can be applied to a wider spectrum of power combining topologies. Two (ideally) identical power combiners are linked by 3-dB hybrid quadrature couplers at the input ports. The magnitude and phase responses introduced by the couplers result in the desired cancellation and combination of signals. This approach is more general in that the only requirement is for the combiner to efficiently interface with a set of 3-dB hybrid quadrature couplers. A schematic of such a network is shown in Figure 2.4. It illustrates how two N-way combiners are linked through 3-dB hybrid quadrature couplers.

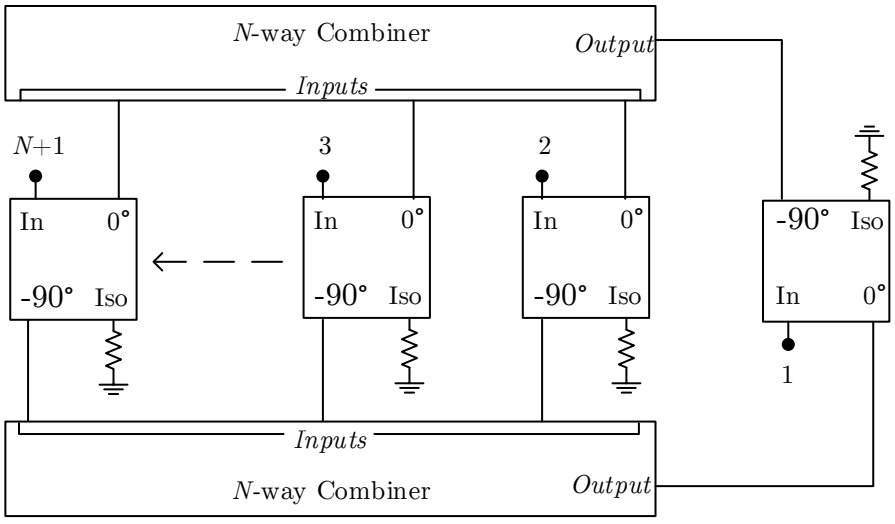

Figure 2.4: Schematic of a general N-way isolation network [22].

Assuming ports 2 to $N+1$ are simultaneously excited with identical sources, the total fields in the combiners are such that all the energy from the input

ports propagate to the combining ports in phase. This operation can be extrapolated by tracing the path from a driven port through to the combining port. An applied time-harmonic signal, indicated by the short blue arrows at the input ports in Figure 2.5, passes through one quadrature coupler before entering the radial combiners. The signal, now split into two equal amplitude signals, enters the radial combiners; with the red signal lagging the blue by 90°. The output coupler is connected inversely relative to the input couplers. This introduces a 90° lag into the blue signal portion as well. The contribution at the output of the complete network (port 1) is then the sum of two identically phase shifted signals, which is the full input signal from ports 2 to $N+1$. Assuming reciprocity in the N-way and quadrature sections, this is also true for the dividing case where port 1 is the input and ports 2 to $N+1$ are the outputs.

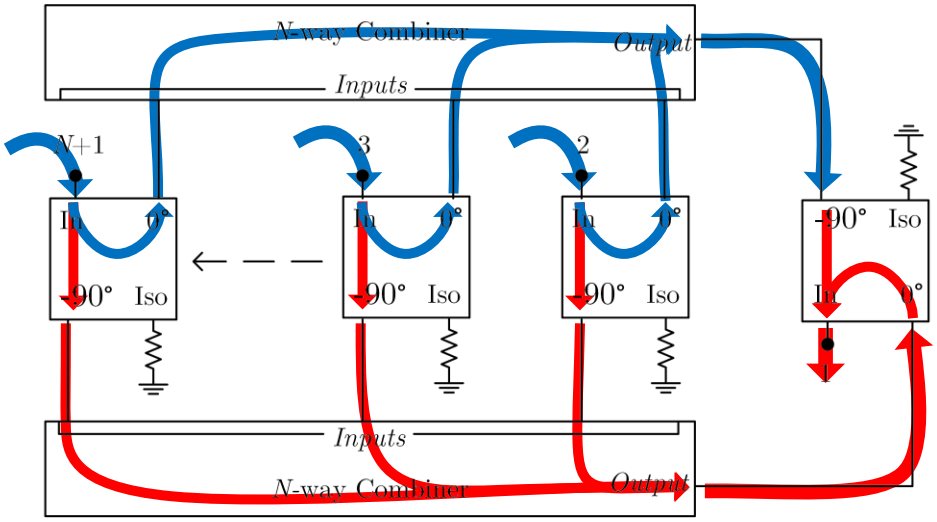

Figure 2.5: Schematic of Figure 2.4 showing the progression of signal phase delays for the symmetrically excited case. Blue arrows have equal phase (no phase delay) and red arrows have equal phase (90° phase delay with respect to blue).

Now, isolation is important when the full system is driven asymmetrically at any port $2 < n < N+1$. This causes unwanted signals appear at the remaining peripheral ports of the radial sections. To analyse these, the signal paths from one input port ($N+1$) to others (2 and 3) are considered with the aid of Figure 2.6. The input signal is again split at the first hybrid coupler into equal amplitude signals, the red again lagging the blue by 90°. Passing through the coupler at the input section for port 3, another 90° phase lag is added red signal. The orange signal is thus lagging the blue by 180°. This creates a sum of two signals of equal amplitude, but 180° phase difference, at port 3. One signal portion is therefore exactly the negative of the other, and

their contributions are cancelled. It is clear then that none of the power from port $N+1$ reaches port 3. The interaction in the hybrid coupler at port 2 in Figure 2.6 illustrates how the load terminations receive the power instead of another input port. In this way, the input ports are isolated from one another and remain impedance matched even under asymmetric inputs.

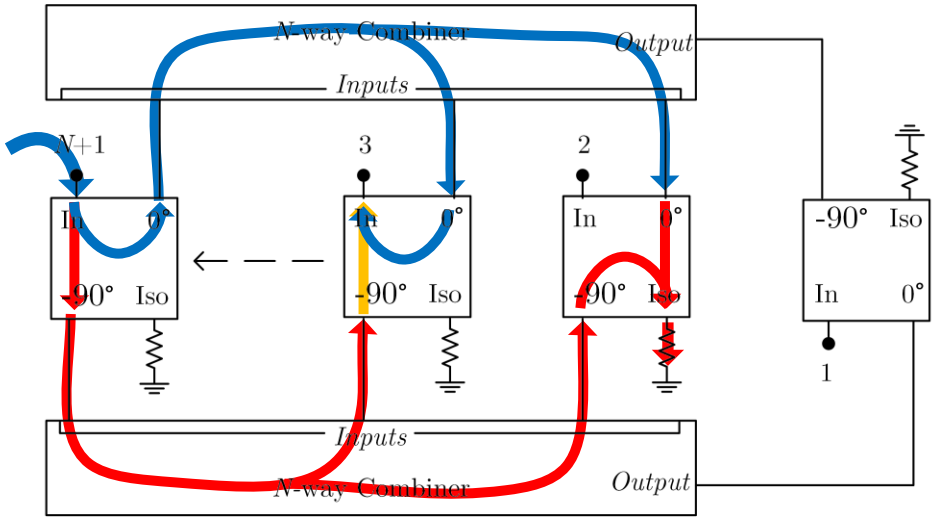

Figure 2.6: Schematic of Figure 2.4 showing the progression of signal phase delays for the asymmetrically excited case. Blue arrows have equal phase (no phase delay) and red arrows have equal phase (90° phase delay with respect to blue). The orange signal is delayed by 90° with respect to red and by 180° relative to blue.

2.4.2 S-Parameter Proof of General Isolation Network

A more robust proof using scattering parameters is presented here. This proof leans heavily on the work in [42]. First, all the isolated combiner components are grouped into only 2 components. The two N-way combiners are grouped into one component, and the $N+1$ quadrature couplers are grouped into another component. Figure 2.7 outlines the relationship of these new components to the underlying elements.

The port numbers are allocated in a way to simplify the matrix algebra [43] required to calculate the cascaded S-parameters of the fully isolated N-way combiner. The S-matrix of the group of couplers is

$$\mathbf{S}_Q = \begin{bmatrix} \mathbf{0} & \begin{bmatrix} \mathbf{C} & \mathbf{T} \\ \mathbf{T} & \mathbf{C} \end{bmatrix} \\ \begin{bmatrix} \mathbf{C} & \mathbf{T} \\ \mathbf{T} & \mathbf{C} \end{bmatrix} & \mathbf{0} \end{bmatrix}, \tag{2.1}$$

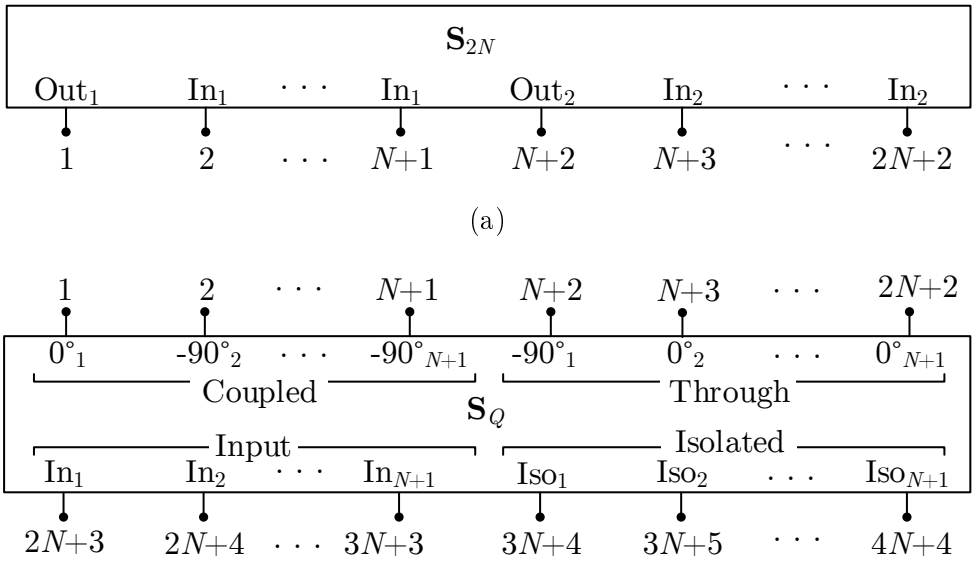

Figure 2.7: Grouped blocks containing (a) the N-way sections and (b) the hybrid quadrature couplers.

with

$$\mathbf{C} = \frac{1}{\sqrt{2}}\begin{bmatrix} 1 & \mathbf{0} \\ \mathbf{0} & -j \cdot \mathbf{I}_N \end{bmatrix} \text{ and } \mathbf{T} = \frac{1}{\sqrt{2}}\begin{bmatrix} -j & \mathbf{0} \\ \mathbf{0} & \mathbf{I}_N \end{bmatrix}, \tag{2.2}$$

where $\mathbf{I}_N$ is the $N \times N$ identity matrix.

The two underlying N-way combiners are contained in the S-matrix

$$\mathbf{S}_{2N} = \begin{bmatrix} \mathbf{S}_N & \mathbf{0} \\ \mathbf{0} & \mathbf{S}_N \end{bmatrix} \tag{2.3}$$

where

$$\mathbf{S}_N = \begin{bmatrix} S^N_{(1,1)} & \cdots & S^N_{(1,N+1)} \\ \vdots & \ddots & \vdots \\ S^N_{(N+1,1)} & \cdots & S^N_{(N+1,N+1)}) \end{bmatrix} \tag{2.4}$$

is the scattering parameters of a single N-way combiner. The cascading operation then joins ports 1 to $2N+2$ of the grouped couplers (Figure 2.7(b)) to the corresponding port numbers on the grouped N-way sections (Figure 2.7(a)) to yield [43]

$$\begin{aligned} \mathbf{S}_{\text{Full}} &= \begin{bmatrix} \mathbf{C} & \mathbf{T} \\ \mathbf{T} & \mathbf{C} \end{bmatrix} \cdot \mathbf{S}_{2N} \cdot \begin{bmatrix} \mathbf{C} & \mathbf{T} \\ \mathbf{T} & \mathbf{C} \end{bmatrix} \\ &= \begin{bmatrix} \mathbf{S}_1 & \mathbf{S}_2 \\ \mathbf{S}_2 & \mathbf{S}_1 \end{bmatrix}, \end{aligned} \tag{2.5}$$

with

$$\mathbf{S}_1 = \mathbf{C}\mathbf{S}_N\mathbf{C} + \mathbf{T}\mathbf{S}_N\mathbf{T} = \begin{bmatrix} 0 & S^N_{(1,2)} & \cdots & S^N_{(1,N+1)} \\ S^N_{(2,1)} & 0 & \cdots & 0 \\ \vdots & \vdots & \ddots & \vdots \\ S^N_{(N+1,1)} & 0 & \cdots & 0 \end{bmatrix} \tag{2.6a}$$

and

$$\mathbf{S}_2 = \mathbf{C}\mathbf{S}_N\mathbf{T} + \mathbf{T}\mathbf{S}_N\mathbf{C} = \begin{bmatrix} S^N_{(1,1)} & 0 & \cdots & 0 \\ 0 & S^N_{(2,2)} & \cdots & S^N_{(2,N+1)} \\ \vdots & \vdots & \ddots & \vdots \\ 0 & S^N_{(N+1,2)} & \cdots & S^N_{(N+1,N+1)} \end{bmatrix}. \tag{2.6b}$$

The component defined by $\mathbf{S}_{\text{Full}}$ has $2N+2$ ports that correspond to ports $2N+3$ to $4N+4$ on $\mathbf{S}_Q$ in Figure 2.7(b). In other words, all the coupler *Input* and *Isolated* ports are available for interfacing with the new combiner. Moreover, from (2.6a) it is clear that perfect input port isolation now exist among ports in the set from 2 to $N+1$, and those from $N+3$ to $2N+2$. All the ports are also perfectly matched.

At this point the full new combiner is still completely lossless and reciprocal (given that $\mathbf{S}_N$ describes a lossless and reciprocal combiner). However, a network that is matched at every port, and has perfect isolation among the input ports, cannot be lossless [44]. With the goal to design some isolated N-way combiner (with $N+1$ ports in total), ports $N+2$ to $2N+2$ of the full combiner can be terminated in isolation loads. These effectively become the losses internal to the network. A perfectly isolated N-way combiner is thus created, and can be characterised by the scattering matrix

$$\mathbf{S}_{\text{Iso}} = \mathbf{S}_1 = \begin{bmatrix} 0 & S^N_{(1,2)} & \cdots & S^N_{(1,N+1)} \\ S^N_{(2,1)} & 0 & \cdots & 0 \\ \vdots & \vdots & \ddots & \vdots \\ S^N_{(N+1,1)} & 0 & \cdots & 0 \end{bmatrix}. \tag{2.7}$$

The only limitation to this isolation network is that the hybrid quadrature couplers must be compatible to the underlying N-way combiners. A significant advantage is that the terminations used for isolation loads can be placed outside the structure. This opens possible applications in high power systems. Given the number of combining ways efficiently achievable with axially symmetric combiners, this network is especially attractive as a means to significantly improve the isolation on these structures.

2.5 Radial Transmission Line Theory

This section will provide some theoretical background on the analysis of electromagnetic fields in radial transmission lines. This section is based on the more detailed work done in [45]–[47].

The first Maxwell equations for time harmonic fields can be written in differential form as

$$\nabla \times \mathbf{E} = -j\omega\mu\mathbf{H} \tag{2.8}$$

$$\nabla \times \mathbf{H} = j\omega\epsilon\mathbf{E} \tag{2.9}$$

in a source free region of an isotropic and lossless medium. This requires the solution of two equations in two unknowns. These are the electric $\mathbf{E}$ and magnetic $\mathbf{H}$ field vectors. The process for $\mathbf{H}$ closely follows that of $\mathbf{E}$, thus only one will be considered here. Substituting (2.9) into the curl of (2.8) yields an equation only in $\mathbf{E}$,

$$\nabla \times \nabla \times \mathbf{E} = -j\omega\mu\nabla \times \mathbf{H} = \omega^2\mu\epsilon\mathbf{E}. \tag{2.10}$$

Simplifying (2.10) using the vector identity

$$\nabla \times \nabla \times \mathbf{A} = \nabla(\nabla \cdot \mathbf{A}) - \nabla^2\mathbf{A}, \tag{2.11}$$

and noting that $\nabla \cdot \mathbf{E} = 0$ in a source free region, results in the vector wave equation

$$\nabla^2\mathbf{E} = -\beta^2\mathbf{E}. \tag{2.12}$$

where $\beta = \omega\sqrt{\mu\epsilon}\ m^{-1}$ is the wave number, or phase constant. Solutions to (2.12), also known as the Helmholtz equation for $\mathbf{E}$, will now be considered.

2.5.1 Direct Approach to Field Solutions

The geometry of a radial transmission line lends itself to analysis in the cylindrical coordinate system as shown in Figure 2.8. A general solution to (2.12) in this coordinate system is assumed to take the form

$$\mathbf{E} = E_\rho(\rho, \phi, z)\hat{\boldsymbol{\rho}} + E_\phi(\rho, \phi, z)\hat{\boldsymbol{\phi}} + E_z(\rho, \phi, z)\hat{\mathbf{z}}. \tag{2.13}$$

Another form of (2.12) can be found through the vector identity (2.11) such that

$$\nabla(\nabla \cdot \mathbf{E}) - \nabla \times \nabla \times \mathbf{E} = -\beta^2\mathbf{E}. \tag{2.14}$$

Substituting (2.13) into (2.14), and simplifying in cylindrical coordinates, results in the following set of scalar equations

$$\nabla^2 E_\rho + \left(-\frac{E_\rho}{\rho^2} - \frac{2}{\rho^2}\frac{\partial E_\phi}{\partial \phi}\right) = -\beta^2 E_\rho \tag{2.15a}$$

$$\nabla^2 E_\phi + \left(-\frac{E_\phi}{\rho^2} - \frac{2}{\rho^2}\frac{\partial E_\rho}{\partial \phi}\right) = -\beta^2 E_\phi \tag{2.15b}$$

$$\nabla^2 E_z = -\beta^2 E_z. \tag{2.15c}$$

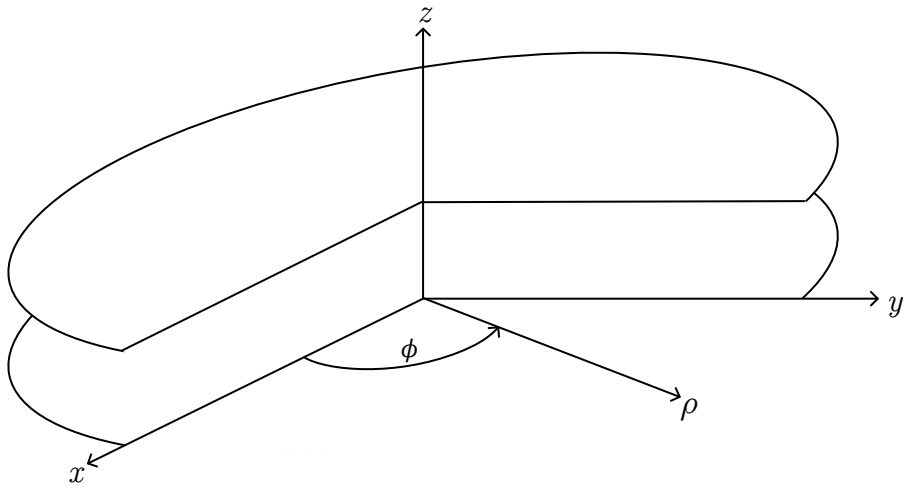

Figure 2.8: Description of the parallel plate radial line in the cylindrical coordinate system.

Coordinates (ρ, ϕ, z) have been omitted from E_ρ, E_ϕ and E_z for the sake of brevity, but dependence thereon is implied. The Laplacian of a scalar function ψ, $\nabla^2\psi(\rho, \phi, z)$, that appear in (2.15a) to (2.15c) is expressed in cylindrical coordinates as

$$\begin{aligned}\nabla^2\psi(\rho,\phi,z) &= \frac{1}{\rho}\frac{\partial}{\partial\rho}\left(\rho\frac{\partial\psi}{\partial\rho}\right) + \frac{1}{\rho^2}\frac{\partial^2\psi}{\partial\phi^2} + \frac{\partial^2\psi}{\partial z^2} \\ &= \frac{\partial^2\psi}{\partial\rho^2} + \frac{1}{\rho}\frac{\partial\psi}{\partial\rho} + \frac{1}{\rho^2}\frac{\partial^2\psi}{\partial\phi^2} + \frac{\partial^2\psi}{\partial z^2}.\end{aligned} \tag{2.16}$$

Equations 2.15a and 2.15b are coupled differential equations, and solving them in this form is an excruciating exercise. A more preferred solution involving potential functions will be looked at later. On the other hand, (2.15c) is an uncoupled differential equation, which can be solved directly. Assuming a separable field component solution of the form

$$\psi(\rho, \phi, z) = f(\rho)g(\phi)h(z) \tag{2.17}$$

and expanding (2.15c) with (2.16) and (2.17) results in

$$gh\frac{\partial^2 f}{\partial\rho^2} + gh\frac{1}{\rho}\frac{\partial f}{\partial\rho} + fh\frac{1}{\rho^2}\frac{\partial^2 g}{\partial\phi^2} + fg\frac{\partial^2 h}{\partial z^2} = -\beta^2 fgh. \tag{2.18}$$

The partial derivatives can be replaced by ordinary derivatives after dividing both sides of (2.18) by fgh, which gives

$$\frac{1}{f}\frac{d^2 f}{d\rho^2} + \frac{1}{f}\frac{1}{\rho}\frac{df}{d\rho} + \frac{1}{g}\frac{1}{\rho^2}\frac{d^2 g}{d\phi^2} + \frac{1}{h}\frac{d^2 h}{dz^2} = -\beta^2. \tag{2.19}$$

The last term on the left-hand side of (2.19) is a function of only z, and can be set equal to a constant such that

$$\frac{1}{h}\frac{\partial^2 h}{\partial z^2} = -\beta_z^2 \Rightarrow \frac{d^2 h}{dz^2} = -\beta_z^2 h. \tag{2.20}$$

Another constant can be introduced on the substitution of (2.20) into (2.19), and multiplying both sides of the result by ρ^2 so that

$$\frac{\rho^2}{f}\frac{d^2 f}{d\rho^2} + \frac{\rho}{f}\frac{df}{d\rho} - m^2 + (\beta^2 - \beta_z^2)\rho^2 = 0, \tag{2.21}$$

where

$$\frac{1}{g}\frac{d^2 g}{d\phi^2} = -m^2 \Rightarrow \frac{d^2 g}{d\phi^2} = -m^2 h. \tag{2.22}$$

Then, introducing the constraint equation

$$\beta^2 - \beta_z^2 = \beta_\rho^2 \tag{2.23}$$

and multiplying both sides of (2.21) by f gives

$$\rho^2\frac{d^2 f}{d\rho^2} + \rho\frac{df}{d\rho} + \left[(\beta_\rho\rho)^2 - m^2\right] f = 0. \tag{2.24}$$

Equation (2.24) is known as the Bessel differential equation. At this point there are three differential equations with known solutions. Solutions to (2.24) take the form

$$f_1(\rho) = A_1 J_m(\beta_\rho\rho) + B_1 Y_m(\beta_\rho\rho) \tag{2.25a}$$

or

$$f_2(\rho) = C_1 H_m^{(1)}(\beta_\rho\rho) + D_1 H_m^{(2)}(\beta_\rho\rho). \tag{2.25b}$$

In (2.25a) J_m and Y_m are the Bessel functions of the first and second kind, respectively, of order m. These are used to represent standing waves in the respective $+\rho$ and $-\rho$ directions. $H_m^{(1)}$ and $H_m^{(2)}$ are Hankel functions of the first and second kind of order m, and represent travelling waves in the respective $+\rho$ and $-\rho$ directions. Solutions to (2.22) and (2.20) take the respective forms

$$g_1(\phi) = A_2 e^{-jm\phi} + B_2 e^{+jm\phi} \tag{2.26a}$$

or

$$g_2(\phi) = C_2\cos(m\phi) + D_2\sin(m\phi), \tag{2.26b}$$

and

$$h_1(z) = A_3 e^{-j\beta_z z} + B_3 e^{+j\beta_z z} \tag{2.27a}$$

or

$$h_2(z) = C_3\cos(\beta_z z) + D_3\sin(\beta_z z). \tag{2.27b}$$

where the forms $e^{\pm jm\phi}$ and $e^{\pm j\beta_z z}$ represent travelling waves, and $\sin/\cos(m\phi)$ and $\sin/\cos(\beta_z z)$ denote standing waves.

2.5.2 Vector Potential Solutions

The direct approach yielded coupled differential equations (2.15a) and (2.15b). Solutions to these field components can be obtained using vector potential functions [45]. Due to magnetic flux density being solenoidal ($\nabla \cdot \mathbf{B} = 0$) in a source free region, it can be expressed as the curl of another vector and will satisfy the vector identity

$$\nabla \cdot (\nabla \times \mathbf{A}) = 0. \tag{2.28}$$

The definition of $\mathbf{A}$ is such that

$$\mathbf{B_A} = \mu \mathbf{H_A} = \nabla \times \mathbf{A}, \tag{2.29}$$

where $\mathbf{A}$ is called the magnetic vector potential and the subscript $_\mathbf{A}$ denotes the field quantity attributed to it. Substituting (2.29) into Faraday's law (2.8) and rearranging gives

$$\nabla \times (\mathbf{E_A} + j\omega \mathbf{A}) = 0. \tag{2.30}$$

The vector identity

$$\nabla \times (-\nabla \psi_e) = 0 \tag{2.31}$$

is incorporated into (2.30) to yield

$$\mathbf{E_A} = -\nabla \psi_e - j\omega \mathbf{A}, \tag{2.32}$$

where ψ_e is an arbitrary scalar electric potential function, dependent on position. In a homogeneous medium, taking the curl of both sides of (2.29) and applying the vector identity (2.11) yields

$$\mu \nabla \times \mathbf{H_A} = \nabla(\nabla \cdot \mathbf{A}) - \nabla^2 \mathbf{A}. \tag{2.33}$$

Substituting (2.32) into (2.9) and setting it equal to (2.33) gives

$$\nabla^2 \mathbf{A} + \beta^2 \mathbf{A} = \nabla(\nabla \cdot \mathbf{A} + j\omega\mu\epsilon\psi_e), \tag{2.34}$$

alternatively expressed in a source free region through (2.11) as

$$\nabla \times \nabla \times \mathbf{A} - \beta^2 \mathbf{A} = -j\omega\mu\epsilon \nabla \psi_e. \tag{2.35}$$

To uniquely define the vector $\mathbf{A}$, the divergence of $\mathbf{A}$ must be defined in addition to the above definition of the curl. With the divergence of a vector independent of the curl, the divergence of $\mathbf{A}$ is defined such that (2.34) is simplified. As such, the divergence of $\mathbf{A}$ is defined as the Lorenz gauge

$$\nabla \cdot \mathbf{A} = -j\omega\mu\epsilon\psi_e. \tag{2.36}$$

Substituting (2.36) into (2.34) results in the vector wave equation

$$\nabla^2 \mathbf{A} + \beta^2 \mathbf{A} = 0 \tag{2.37}$$

and (2.32) becomes

$$\mathbf{E_A} = -j\omega\mathbf{A} - \frac{j}{\omega\mu\epsilon}\nabla(\nabla\cdot\mathbf{A}). \tag{2.38}$$

The electric vector potential $\mathbf{F}$ follows the same logic, since the electric flux density is also solenoidal ($\nabla\cdot\mathbf{D}=0$) in a source free region. From (2.28) $\mathbf{F}$ is defined as

$$\mathbf{D_F} = \epsilon\mathbf{E_F} = -\nabla\times\mathbf{F}, \tag{2.39}$$

where the field quantity attributed to $\mathbf{F}$ is denoted by the subscript $_\mathbf{F}$. Expressing (2.9) in terms of (2.39) and the identity (2.11) produces

$$\mathbf{H_F} = -\nabla\psi_m - j\omega\mathbf{F}. \tag{2.40}$$

Here ψ_m is an arbitrary scalar magnetic potential function of position. Following the preceding argument for $\mathbf{A}$, the results in terms of $\mathbf{F}$ are

$$\nabla\times\nabla\times\mathbf{F} - \beta^2\mathbf{F} = -j\omega\mu\epsilon\nabla\psi_m, \tag{2.41}$$

$$\nabla^2\mathbf{F} + \beta^2\mathbf{F} = 0 \tag{2.42}$$

and finally

$$\mathbf{H_F} = -j\omega\mathbf{F} - \frac{j}{\omega\mu\epsilon}\nabla(\nabla\cdot\mathbf{F}). \tag{2.43}$$

The total fields are then determined by superposition of the fields due to the respective vector potential functions, such that

$$\mathbf{E} = \mathbf{E_A} + \mathbf{E_F} = -j\omega\mathbf{A} - \frac{j}{\omega\mu\epsilon}\nabla(\nabla\cdot\mathbf{A}) - \frac{1}{\epsilon}\nabla\times\mathbf{F} \tag{2.44}$$

$$\mathbf{H} = \mathbf{H_A} + \mathbf{H_F} = \frac{1}{\mu}\nabla\times\mathbf{A} - j\omega\mathbf{F} - \frac{j}{\omega\mu\epsilon}\nabla(\nabla\cdot\mathbf{F}). \tag{2.45}$$

2.5.3 Fundamental TEM$^\rho$ Field Mode

Some foreknowledge of the expected field behaviour is necessary to choose the appropriate field solution. The lowest order non-trivial field mode that can exist inside the finite cavity will vary along only one direction. With the combiner guiding energy outward (inward) from the centre (periphery), the lowest order mode would have to vary along ρ. It is then expected that the electric field will only have a z component, and the magnetic field will only have a ϕ component. The result is illustrated in Figure 2.9, where TEM$^\rho$ waves propagate with cylindrical fronts concentric to the z-axis. To simplify the derivation, the solution will be approached by first seeking a solution for the TM^z mode. It will then be shown to satisfy the TEM$^\rho$ condition for no field variation along z and ϕ.

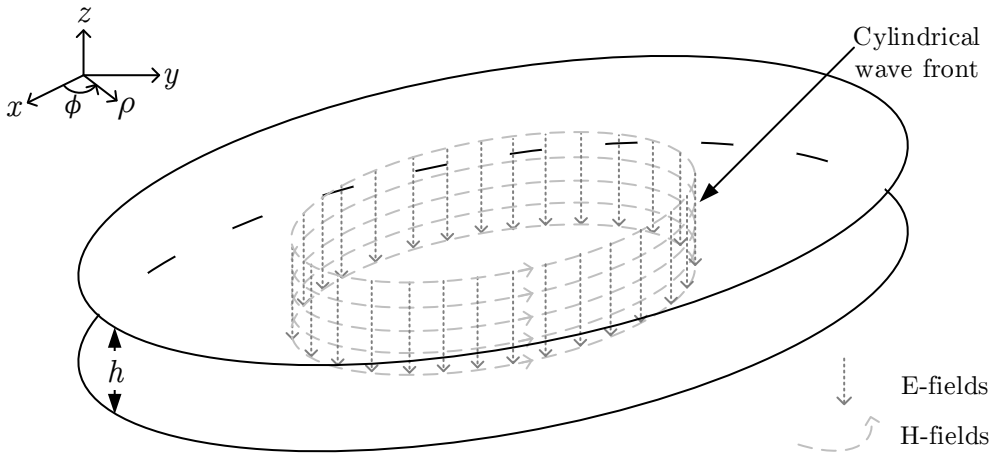

Figure 2.9: Cylindrical wave-front of the dominant TEM^{ρ} mode.

Choosing the vector potentials A and F as

$$\mathbf{A} = A_z \hat{\mathbf{z}} \tag{2.46a}$$

$$\mathbf{F} = 0, \tag{2.46b}$$

and substituting into (2.44) and (2.45) yields

$$\mathbf{E} = -j\omega A_z \hat{\mathbf{z}} - \frac{j}{\omega\mu\epsilon} \nabla \left(\frac{\partial A_z}{\partial z} \right) \hat{\mathbf{z}} \tag{2.47}$$

$$\mathbf{H} = \frac{1}{\mu} \left(\frac{1}{\rho} \frac{\partial A_z}{\partial \phi} \hat{\boldsymbol{\rho}} - \frac{\partial A_z}{\partial \rho} \hat{\boldsymbol{\phi}} \right). \tag{2.48}$$

From the axial symmetry of the problem, no variation along ϕ is expected in the fundamental mode, which requires that $\frac{\partial}{\partial \phi} A_z = 0$. Additionally, the lowest order mode fields are also expected to not vary along z, in turn requiring that $\frac{\partial}{\partial z} A_z = 0$. From (2.47) and (2.48) it is clear that enforcing these requirements will result in a single component for each of $\mathbf{E}$ and $\mathbf{H}$.

Since $\mathbf{A}$ must satisfy (2.37), the solutions derived in Section 2.5.1 are valid options for $\mathbf{A}$ as well. Using the separable approach again, $\mathbf{A}$ can be expanded as

$$A_z(\rho, \phi, z)\hat{\mathbf{z}} = f(\rho)g(\phi)h(z)\hat{\mathbf{z}}. \tag{2.49}$$

Appropriate solutions are selected from (2.25) to (2.27) so that

$$\begin{aligned} A_z(\rho, \phi, z) = &\left[C_1 H_m^{(1)}(\beta_\rho \rho) + D_1 H_m^{(2)}(\beta_\rho \rho) \right] \\ &\times \left[C_2 \cos(m\phi) + D_2 \sin(m\phi) \right] \\ &\times \left[C_3 \cos(\beta_z z) + D_3 \sin(\beta_z z) \right]. \end{aligned} \tag{2.50}$$

This set of solutions configures A_z as a travelling wave along ρ, with standing waves in the ϕ and z directions. Furthermore, variation along the ϕ and z

directions can be eliminated by setting $m = \beta_z = 0$, so that

$$\left.\frac{\partial A_z}{\partial \phi}\right|_{m=0} = A_z^1(\rho, z)\frac{d}{d\phi}\Big[\cos(m\phi) + \sin(m\phi)\Big]_{m=0} = 0 \tag{2.51a}$$

$$\left.\frac{\partial A_z}{\partial z}\right|_{\beta_z=0} = A_z^2(\rho, \phi)\frac{d}{dz}\Big[\cos(\beta_z z) + \sin(\beta_z z)\Big]_{\beta_z=0} = 0, \tag{2.51b}$$

where A_z^1 and A_z^2 represents the parts of A_z unaffected by the respective partial derivation operations. This leaves A_z to be dependent only on the ρ position, such that

$$A_z(\rho) = C_1 H_0^{(1)}(\beta_\rho \rho) + D_1 H_0^{(2)}(\beta_\rho \rho)\ . \tag{2.52}$$

The constants C_2 and C_3 from (2.50) are absorbed into C_1 and D_1 in (2.52). Equation (2.48) is then left with the partial derivative $\frac{\partial}{\partial \rho}A_z$, which requires defining derivatives of the Hankel functions in (2.24). One of the definitions is given as

$$\frac{d}{dx}\left[H_m(\alpha x)\right] = -\alpha H_{m+1}(\alpha x) + \frac{m}{x}H_m(\alpha x), \tag{2.53}$$

where H can be any of the Bessel (J_m, Y_m) or Hankel $(H_m^{(1)}, H_m^{(2)})$ functions. Substituting (2.51) and (2.52) into (2.47) and (2.48), and applying (2.53), the field solutions to the dominant mode in a parallel-plate type radial transmission line become

$$\mathbf{E} = -j\omega\left[C_1 H_0^{(1)}(\beta_\rho \rho) + D_1 H_0^{(2)}(\beta_\rho \rho)\right]\hat{\mathbf{z}} \tag{2.54}$$

$$\mathbf{H} = \frac{\beta_\rho}{\mu}\left[C_2 H_1^{(1)}(\beta_\rho \rho) + D_2 H_1^{(2)}(\beta_\rho \rho)\right]\hat{\boldsymbol{\phi}}. \tag{2.55}$$

These solutions can now be used to determine the input impedance of the transmission line.

2.5.4 Characteristic Impedance of a Partially Filled Radial Line

To calculate the input impedance using Ohm's law, the voltage and current along ρ must be calculated. For a radial combiner with height h as in Figure 2.9, these are

$$V = -\int_0^h E_z dz = \omega h\left[jE_z^f(\rho)\right]\ \text{V} \tag{2.56a}$$

and

$$I = \oint_0^{2\pi} H_\phi \rho d\phi = \frac{\beta_\rho}{\mu} 2\pi\rho\left[H_\phi^f(\rho)\right]\ \text{A}, \tag{2.56b}$$

where

$$E_z^f(\rho) = C_1 H_0^{(1)}(\beta_\rho \rho) + D_1 H_0^{(2)}(\beta_\rho \rho) \tag{2.57a}$$

$$H_\phi^f(\rho) = C_2 H_1^{(1)}(\beta_\rho \rho) + D_2 H_1^{(2)}(\beta_\rho \rho) \tag{2.57b}$$

$$\beta_\rho = \beta = \omega\sqrt{\epsilon\mu}. \tag{2.57c}$$

The resultant impedance at some point ρ along the radial line is then given by

$$Z(\rho) = \frac{V}{I} = \frac{\eta h}{2\pi\rho}\left[j\frac{E_z^f(\rho)}{H_\phi^f(\rho)}\right] \ \Omega, \tag{2.58}$$

with the wave impedance denoted by $\eta = \sqrt{\mu/\epsilon}$.

Now, the definition of the characteristic impedance of a radial transmission line from circuit theory is given by [47], [48]

$$Z_r(\rho) = \sqrt{\frac{L}{C}} = \eta\frac{h}{2\pi\rho} \ \Omega, \tag{2.59}$$

where L and C are the inductance and capacitance, respectively, per unit length of the transmission line. Accounting for a single medium in the radial cavity is straight forward. The permittivity in the wave impedance becomes $\epsilon = \epsilon_0\epsilon_r$, where ϵ_r is the relative dielectric constant of the medium. The design presented in Section 3.1, however, employs a partially filled radial cavity. Not much information was found about the effective dielectric properties of partially filled radial transmission lines. This necessitated a brief derivation thereof for the parallel plate type radial line.

The capacitance per unit length is assumed to be analogous to the capacitance of a circular parallel plate capacitor. This assumption is based on the geometrical correlation between the two structures. The capacitance of a circular parallel plate capacitor is given by

$$C = \frac{\epsilon A}{h} = \frac{\epsilon\pi r^2}{h} \ \mathrm{F}, \tag{2.60}$$

where A is the area and r is the radius of each plate. The distance between the plates is denoted by h. To get the capacitance per unit length, the derivative is taken along the transmission direction. In this case, it is along the radius r, and the result is

$$C_r = \frac{\epsilon}{h}2\pi r \ \mathrm{F/m}. \tag{2.61}$$

Another assumption is that the capacitances resulting from the air and the substrate form a set of series capacitances. Combining these capacitances, C_0

and C_s, in this way, results in the total capacitance per unit length of

$$\begin{aligned} C_T &= \left(\frac{1}{C_a} + \frac{1}{C_s}\right)^{-1} \\ &= \left(\frac{h-d}{\epsilon_0 \cdot 2\pi r} + \frac{d}{\epsilon_0 \epsilon_s \cdot 2\pi r}\right)^{-1} \\ &= \frac{\epsilon_0 \cdot 2\pi r}{h - d(1-\epsilon_s^{-1})} \text{ F/m}, \end{aligned} \tag{2.62}$$

where ϵ_s is the relative dielectric constant of the substrate.

Lastly, the permeabilities of both materials are assumed to be equal to that of free space. Following the same logic as for (2.61), the inductance per unit length is defined as

$$L = \frac{\mu_0 h}{2\pi r} \text{ H/m}. \tag{2.63}$$

It then follows, by substituting (2.62) and (2.63) into (2.59), that the characteristic impedance of the partially filled radial line is

$$\begin{aligned} Z_r &= \sqrt{\frac{\mu_0 h}{2\pi r} \cdot \frac{h - d(1-\epsilon_s^{-1})}{\epsilon_0 \cdot 2\pi r}} \ \Omega \\ &= \frac{h}{2\pi r}\sqrt{\frac{\mu_0}{\epsilon_0}}\sqrt{1 - \frac{d}{h}(1-\epsilon_s^{-1})} \ \Omega \end{aligned} \tag{2.64}$$

Incorporating the last square root term in (2.64) into a single variable allows an effective relative dielectric constant ϵ_e to be defined. This definition follows as

$$\sqrt{\frac{1}{\epsilon_e}} = \sqrt{1 - \frac{d}{h}(1-\epsilon_s^{-1})} \ . \tag{2.65}$$

Note that equation (2.65) is not dependent on the geometry normal to the transmission line height. It should therefore, although derived for the radial case, hold for the rectangular parallel plate transmission line as well. The closed form in (2.65) is tested against a 3D model simulated in CST Microwave Suite [49]. The model used is a rectangular partially filled parallel plate transmission line, as shown in Figure 2.10. The ratio d/h is incremented through the non-trivial domain $0 < d/h < 1$ and the results evaluated. Figure 2.11 shows the correlation of (2.65) with results from the 3D simulations. Each mark from the simulation is the value CST computed as the effective relative dielectric constant in the port aperture at 4 GHz.

This substantiates the closed form expression in (2.65), and the relationship between the radial and rectangular parallel plate transmission lines. Although this closed form expression neglects any material losses, it will be useful during the design of the partially filled radial combiner.

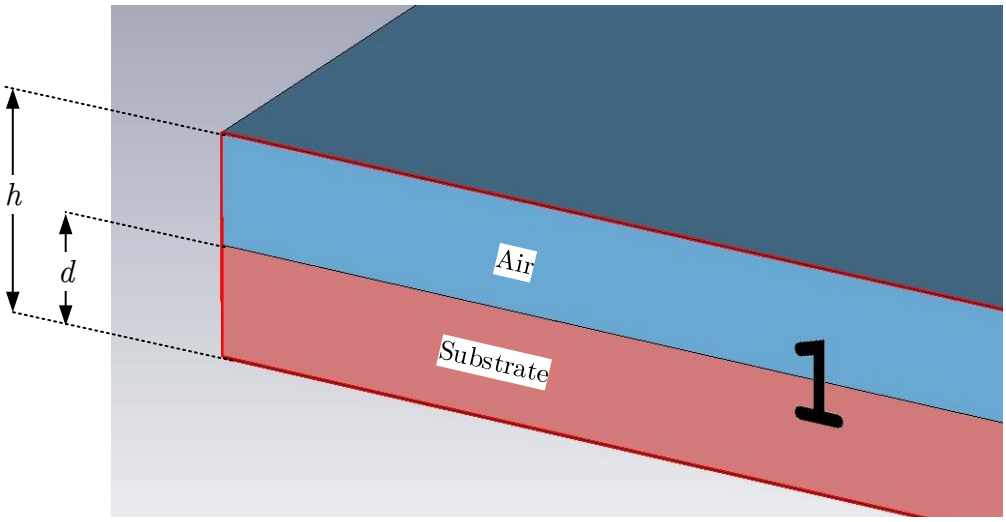

Figure 2.10: The model used to validate the closed form effective relative dielectric of a partially filled parallel plate transmission line.

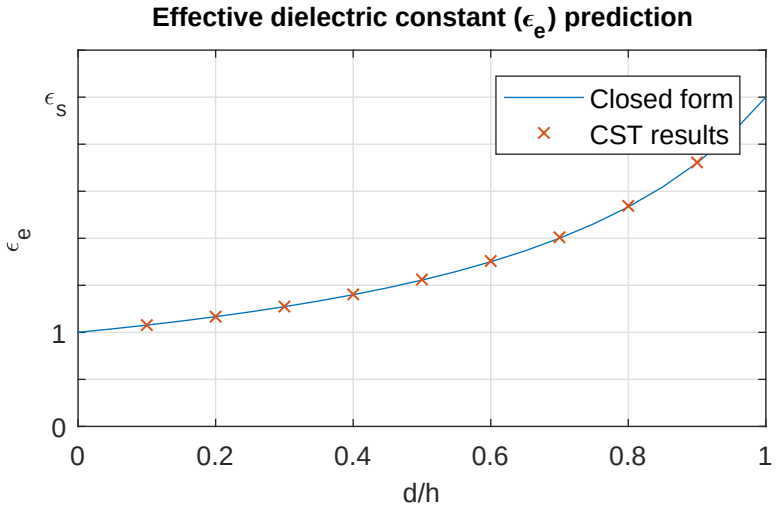

Figure 2.11: Correlation between 3D simulation and the closed form definition of the effective relative dielectric constant of a parallel plate radial transmission line.

Chapter 3

Design of a Radial Combiner

A non-isolated combiner is designed first to confirm the functionality of the proposed radial combiner topology before embarking on the more involved task of implementing the passive isolation network. This chapter elaborates on the design of a suitable, partially-filled, non-isolated N-way radial power combiner. Each major feature of the combiner design is discussed in detail. Operational specifications are to achieve a centre port reflection coefficient of $|S_{1,1}| < -15$ dB over a minimum relative bandwidth of 20%. After determining the parameters for the correct characteristic impedance, attention will be directed to matching the coaxial connection to the centre of the combiner. Following on that is the design of the peripheral ports. All the components are then merged into the final design of the radial combiner. The last part of the section details the results of manufacturing and testing a prototype.

3.1 Radial Line Characteristic Impedance

A section of a parallel plate radial transmission line will be used as the main component of the combiner. This radial line section, in many radial combiners, has a characteristic impedance at the centre that is significantly lower than the 50 Ω impedance common to RF interfaces. The radii of the coaxial-to-radial line transition, r_2 and r_3 in Figure 3.1, are usually chosen to create a coaxial characteristic impedance equal to that of the radial line at r_2. Modern designs include one or more impedance matching sections between the low impedance coaxial transition and some standard interface. Such a section is indicated with radius r_4 in Figure 3.1

This popular technique usually relies on carefully machining the inner conductor of the coaxial matching section. Since the inner conductor is relatively small in diameter, it requires tight manufacturing tolerances to achieve the desired functionality. As such, this approach tends to complicate the manufacturing process. It will therefore be avoided to reduce manufacturing complexity. The characteristic impedance at the centre of the radial line is instead

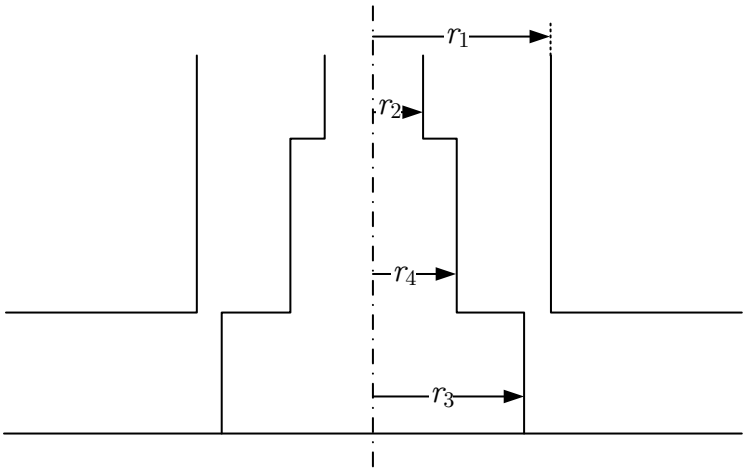

Figure 3.1: Basic stepped transition from a coaxial line into the centre of the radial line introduced in [29].

designed to closely match a standard 50 Ω connector.

The external radius of a threaded SMA connector, used as interface at the centre port, will be the start of the radial line section. This radius is taken from [50] as $r_{SMA} = 3.175$ mm. The radial characteristic impedance at this radius is chosen as $Z_r(r_{SMA}) = 50\,\Omega$.

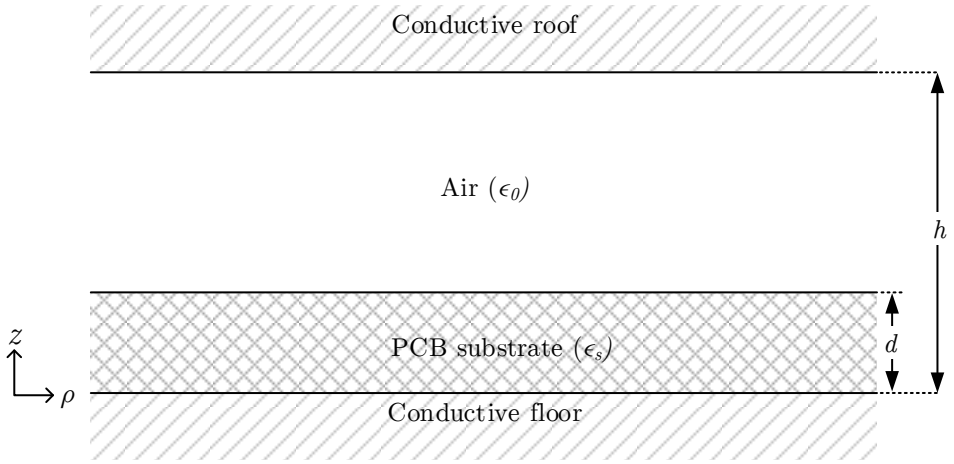

Figure 3.2: A cross section in the ρz-plane of the partially filled radial waveguide geometry.

The substrate choice will determine important variables still present in (2.64). Factoring in the cost and low claimed dielectric loss, Mercurywave 9350 will be used as the substrate for this design [51]. The relevant material parameters are the relative dielectric constant of $\epsilon_s = 3.5$ and the chosen substrate

thickness of $d = 0.508$ mm. The height for $Z_r(r_{SMA}) = 50\Omega$ can be determined by rearranging (2.64) to yield the quadratic equation

$$h^2 - hd(1 - \epsilon_s^{-1}) - (Z_r(r_{SMA}) \cdot 2\pi r_c)^2 \frac{\epsilon_0}{\mu_0} = 0 \tag{3.1}$$

and then substituting all the known variables. The practical solution to (3.1) gives the combiner height as $h = 2.835$ mm. This height is indicated in Figure 3.2.

These values are tested through simulation by approximating an infinitely short angular section of the radial line with a section of parallel plate transmission line. This relationship is illustrated, where the curved aperture A-A in Figure 3.3(a) is approximated by the flat aperture A'-A' in Figure 3.3(b). The parallel plate approximation stems from the similarity in geometry and the ensuing characteristic impedance equations of the two transmission line types.

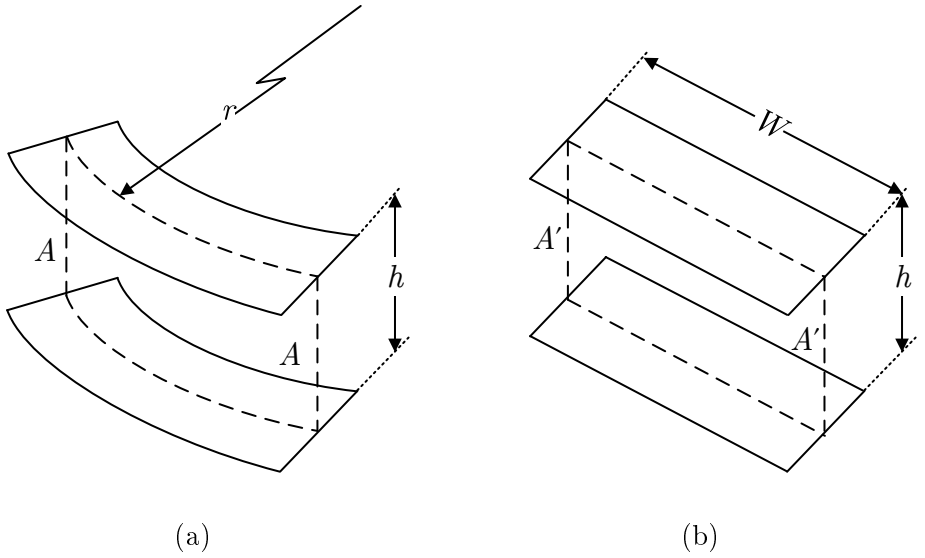

Figure 3.3: The approximation of an angular segment of radial transmission line (a) with an equivalent parallel plate section (b).

There exists a commonality between radial lines and parallel plate transmission lines, such that the only difference in their characteristic impedance formulae are the terms $2\pi r$ and W, respectively. More than that, the gradient of the circumference curve is also small at a large radius. The radial line, along a cylindrical plane at some large radius, can therefore be represented in a piecewise fashion by a number of parallel plate waveguides.

This approach is taken because the 3D simulation software only allows waveguide ports to exist in flat planes. In the ideal case the simulation would have been excited by finite cylindrical waveguide ports at the necessary radii.

In this example, the radius is taken to be $r_p = 50.8$ mm, the point where $Z_r(r_p) = 50/16 = 3.125\Omega$. This way the radial line characteristic impedance will be closely matched to the 16 parallel ports with $Z_0 = 50\Omega$ each. The circumference is divided by the number of ports $N = 16$ to give the equivalent width of a single parallel plate transmission line port. The impedance of one of the equivalent parallel plate lines is then expected to be $Z_{pp} = N \times Z_r(r_p) \approx 50\ \Omega$.

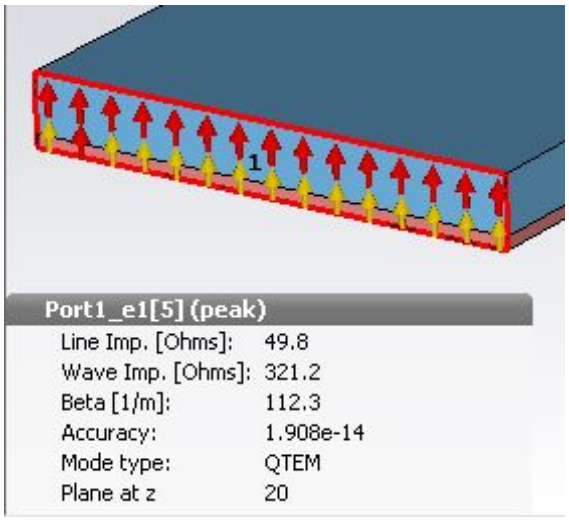

Figure 3.4: Simulation model and results of the parallel plate approximation.

The model in Figure 3.4 has dimensions $h = 2.835$ mm, $W = \frac{2\pi\ r_p}{N} = 19.95$ mm and substrate thickness $d = 0.508$ mm. The parallel plate characteristic impedance is found to be $Z_{pp} = 49.8\ \Omega$ from the simulation model. Therefore, given an appropriate relationship between the angle and radius of the angular radial line section, this design approximation is an acceptably accurate model of the circumferential apertures. It substantiates the characteristic impedance calculations and will again be used in Section 3.4 to analyse the peripheral ports of the combiner.

3.2 Complex Input Impedance

Along with the characteristic impedance of the radial line, the complex input impedance at the centre must also be compensated for. This complex input impedance depends on various geometric factors. Some of these are the height and central entry radius, as considered for the characteristic impedance in Section 3.1. Another factor is the termination at the periphery of the radial line.

Two useful peripheral termination options are considered. These are a matched load condition and a short circuit condition. A matched load scenario

is of course useful to predict the operation for energy being coupled through the combiner. On the other hand, a short circuit is a practical method to physically terminate the radial line section at its periphery. Besides the type of termination, the radius at which either of those are implemented also influences the complex input impedance of the radial line. This is the input impedance if one were to enter the radial line at some radius $r < r_p$, and look outward to r_p.

The input impedance is calculated from the admittance description of radial lines in [47]. This gives the input impedance at some radius $r < r_p$, for a matched periphery at r_p defined as $Z(r_p) = Z_r(r_p)$, to be

$$Z_{in}(r) = Z_r(r)\frac{j\zeta(\beta_\rho r, \beta_\rho r_p) + \mathrm{Ct}(\beta_\rho r, \beta_\rho r_p)}{j - \mathrm{Ct}(\beta_\rho r, \beta_\rho r_p)}, \tag{3.2a}$$

where

$$\mathrm{Ct}(\beta_\rho r, \beta_\rho r_p) = \frac{J_1(\beta_\rho r_p)Y_0(\beta_\rho r) - Y_1(\beta_\rho r_p)J_0(\beta_\rho r)}{J_1(\beta_\rho r)Y_1(\beta_\rho r_p) - Y_1(\beta_\rho r)J_1(\beta_\rho r_p)} \tag{3.2b}$$

$$\zeta(\beta_\rho r, \beta_\rho r_p) = \frac{J_0(\beta_\rho r)Y_0(\beta_\rho r_p) - Y_0(\beta_\rho r)J_0(\beta_\rho r_p)}{J_1(\beta_\rho r)Y_1(\beta_\rho r_p) - Y_1(\beta_\rho r)J_1(\beta_\rho r_p)}. \tag{3.2c}$$

For this case, as shown in Figure 3.5, the reactive component of the complex input impedance is seen to have an oscillating nature versus the radius. This is at the midband frequency of 4 GHz. One can also see a correlation between the characteristic impedance and the amplitude of the reactive part of the impedance. The radial position of the minimum and maximum points on the complex input impedance curve are strongly influenced by the radius at which the line is terminated. A good impression is formed of what can be expected when the peripheral termination is applied at varying radii.

The short circuit will be applied approximately one quarter-wavelength behind the peripheral ports, at a radius $r_s > r_p$. This will naturally create an open circuit condition along the radial line at the peripheral ports. Ideally, the signal will then couple completely to the peripheral ports, as they are in parallel with an open circuit. The effect of short circuit peripheral termination on the input impedance at r_p is described, again from [47], by the equation

$$Z_{in}(r_p) = jZ_r(r_p)\left[\frac{J_0(\beta_\rho r_p)Y_0(\beta_\rho r_s) - Y_0(\beta_\rho r_p)J_0(\beta_\rho r_s)}{J_1(\beta_\rho r_p)Y_0(\beta_\rho r_s) - Y_1(\beta_\rho r_p)J_0(\beta_\rho r_s)}\right]. \tag{3.3}$$

Figure 3.6 shows that the physical short circuit at one quarter-wavelength further creates the desired open circuit condition at r_p with $r_s \approx 70.8$ mm.

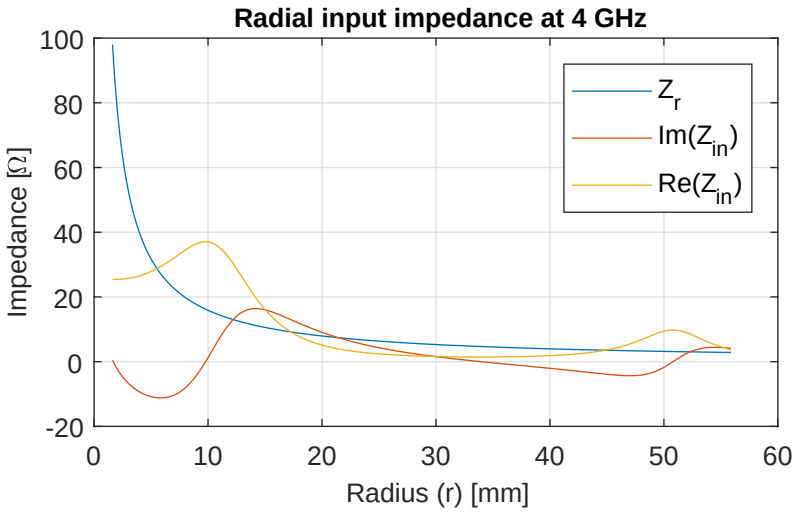

Figure 3.5: Input and characteristic impedance with $r_p = 50.8$ mm and the radial line terminated in $16 \times 50\ \Omega$ ports.

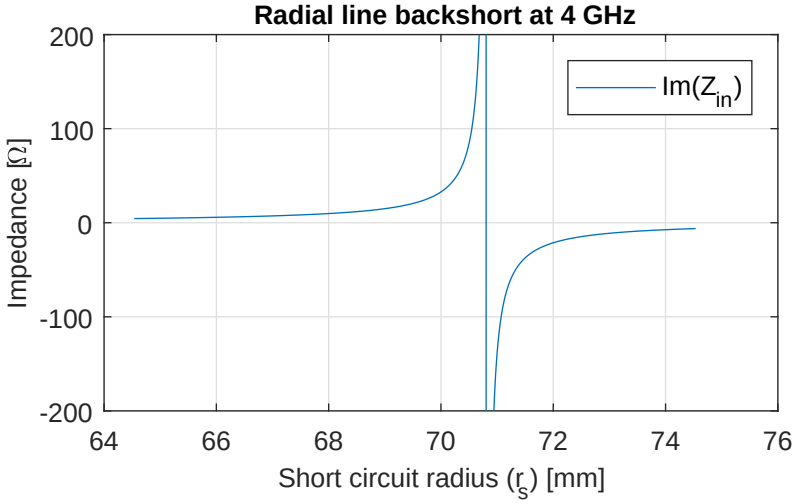

Figure 3.6: The input impedance at $r_p = 50.8$ mm (looking in the direction of increasing radius) as a function of the short circuit radius r_s.

3.3 Centre Port

The geometry of the centre transition lends itself to a capacitive matching at the centre. If the central connector stops flush with the substrate, it provides a controlled environment on which the matching can be tuned. A matching element can be realised with an annular ring etched on top of the substrate at the bottom of the combiner as shown in Figure 3.7. The ring then also acts as a seat for the SMA connector used at the center port. This combination should allow sufficiently precise control over the input impedance, without drastically complicating the manufacturing.

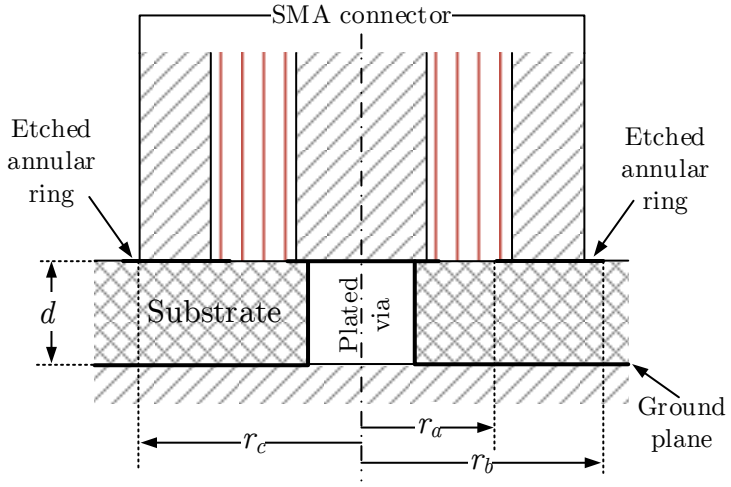

Figure 3.7: Geometry of the transition from the coaxial connector to the radial transmission line.

Since the input impedance is influenced strongly by the peripheral termination radius, the imaginary minimum at $r \approx 5$ mm in Figure 3.5 can be adjusted by altering the radius where the peripheral ports sit. If the peripheral port radius r_p is shortened appropriately, the reactive input impedance can be tuned to become positive (inductive) at the entry radius $r_c = 3.175$ mm. Changing the peripheral radius to $r_p = 46$ mm produces the desired effect, as shown in Figure 3.8. This procedure reaches a compromise between matching the characteristic impedance of the peripheral ports, and matching the complex input impedance of the central port.

The inner radius of the ring is chosen as $r_a = 1.8$ mm, slightly smaller than the outer radius of the SMA dielectric. This leaves the ring's outer radius r_b to be calculated. The resultant shunt capacitance should offset the radial line inductance in the vicinity of r_c.

Figure 3.8 shows that for 1.8 mm $< r <$ 3 mm, the inductance forms a relatively flat local minimum. The real part of the input impedance is also shown to vary only moderately over the radius range of interest.

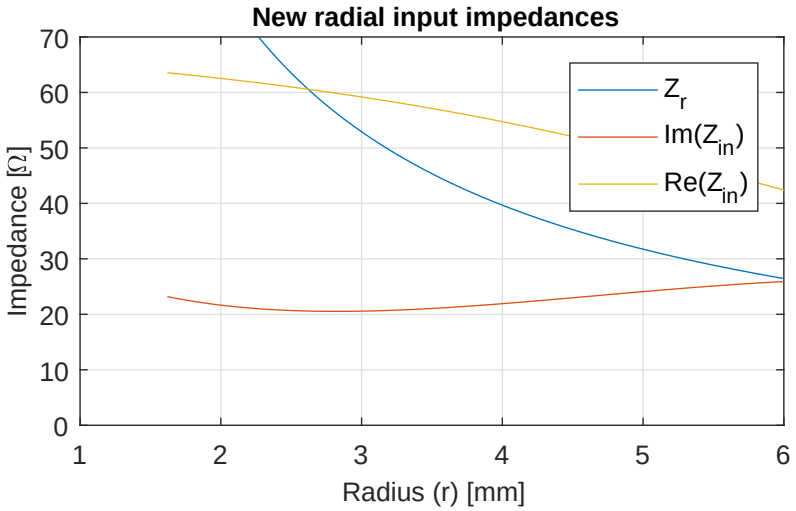

Figure 3.8: Input and characteristic impedance curve with $r_p = 46$ mm.

The transition will be designed by a trial-and-error method in 3D simulation software, starting from a very simple setup. Initially, the central SMA connector with an unaltered body will press on the PCB through the roof of the combiner. Both the centre conductor and dielectric is considered to end flush with the connector body. The conduction path from the centre conductor of the connector will extend to the floor of the radial line through a plated via.

In conjunction with varying other parameters, the outer radius of the connector body will be reduced if necessary. Iterations of this will run until a practical result is obtained in terms of operation and preliminary manufacturing restrictions. Once that is achieved, a capacitive ring will be designed and etched on the PCB. Its purpose is to act as a seat for the connector body. The etched seat allows fine-tuning accuracy beyond the relatively high tolerances permitted in the machining of the connector body.

A cross section of a simple center port configuration is shown in Figure 3.9. It consists of the radial combiner enclosure, the PCB substrate, vacuum layer, and the center connector. All conducting materials are perfect electric conductors (PEC) at this stage. Using the standard SMA specifications [50], the centre conductor diameter is 1.28 mm, and the inside diameter of the connector body is 4.08 mm. The dielectric between the connector conductors is lossless PTFE (Teflon) with relative dielectric constant $\epsilon_{coax} = 2.1$.

The centre conductor makes contact with a plated via through the substrate, modelled here as a conducting cylinder with a diameter of 1 mm. Lastly, the outer radius of the threaded connector body is swept between 2.2 mm $\leqslant r_c \leqslant$ 3.175 mm. The centre port is designated by Port 1.

It is necessary to elaborate on the peripheral ports used in the simulation at this point. Ideally one would want a waveguide aperture that spans the cylindrical plane at radius r_p. As mentioned, this is not possible in the full wave simulation suite used. It is required to make use of the parallel plate

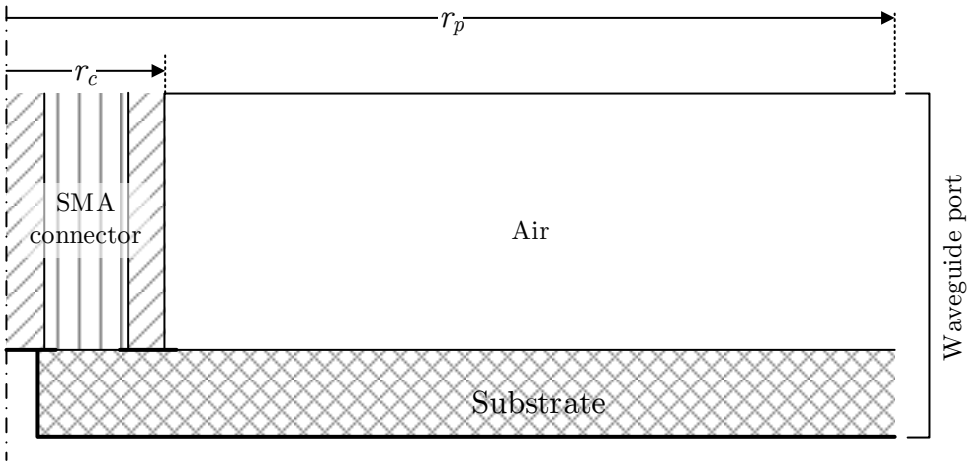

Figure 3.9: A cross section of the geometry used to model the coaxial-to-radial line transition.

waveguide approximation.

These ports are then set up around the circumference of the radial line at the terminating radius. This setup is shown in Figure 3.10, where the vacant space in the model is considered PEC. The upper and lower boundaries of the port are the conducting planes of the radial combiner. The side boundaries are set to be magnetically shielded in the port options window. This is implemented by forcing tangential magnetic fields to zero along the appropriate port boundaries. Their cumulative field pattern would closely match the fundamental quasi TEM^r mode that exits inside the radial combiner. While this setup is not completely axially symmetric, it provides the necessary geometry from which the design can be developed. The top and bottom simulation boundaries are grounded PEC, and the lateral boundaries outside the peripheral ports are chosen to absorb incident waves.

The S-parameter results in Figure 3.11 show that this implementation is rather well matched for $r_c = 2.5$ mm. Figure 3.11(a) indicates an input reflection level under -15 dB across a fractional bandwidth of more than 25%. One can see from Figure 3.11(b) that the complex input impedance behaves as expected. As the outer radius of the connector body is increased, the imaginary part of the input impedance becomes more capacitive.

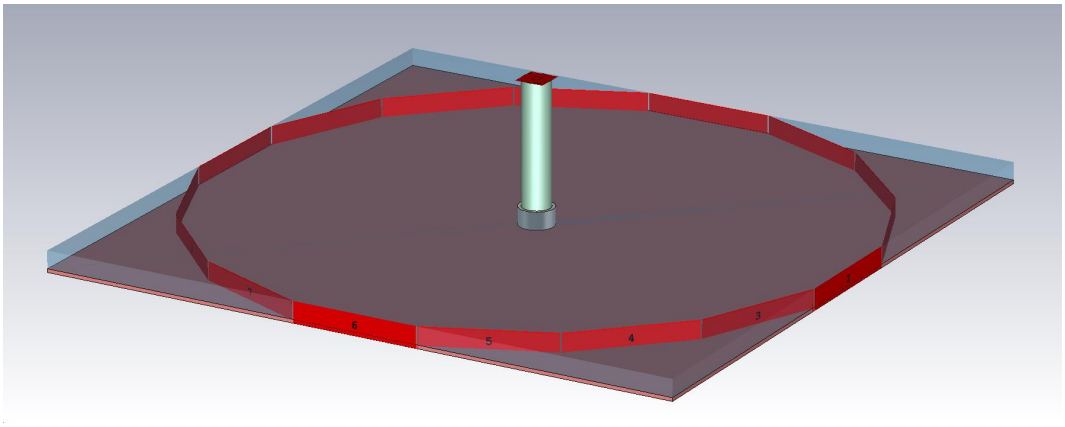

Figure 3.10: The basic radial line using waveguide ports along the circumference and a simple coaxial-to-radial line transition.

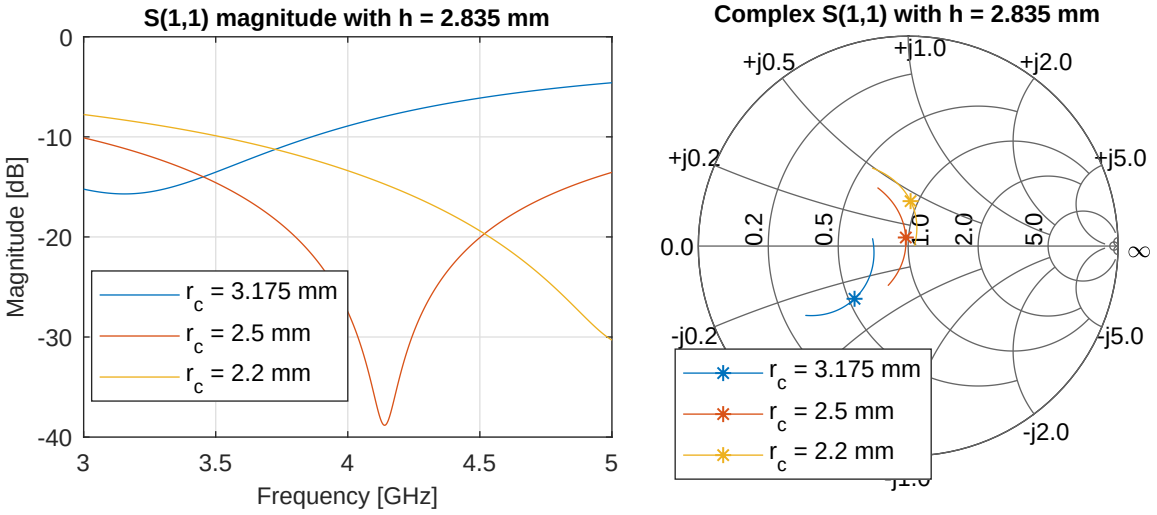

(a) (b)

Figure 3.11: (a) The magnitude in dB and (b) the complex S(1,1) results obtained by altering the outer radius of the centre SMA connector body.

3.4 Peripheral Ports

Traditionally, planar and cavity radial combiners make use of different methods to couple energy via the peripheral ports. Planar radial combiners usually split up from the radial transmission line section into multiple microstrip lines. The simplest cavity combiner coupling methods utilize inductive posts from the radial combiner into coaxial lines.

An option well suited to the current design is shown in Figure 3.12. Coupling is facilitated from the air cavity into microstrip lines by inductive posts. These posts extend from the roof of the combiner onto copper pads etched on the substrate. Each pad then runs into a microstrip line. This allows for great flexibility at the peripheral ports. Ports can simply be terminated in a connector at the edge of the combiner, or further planar elements can be added to the microstrip lines.

An advantage if this coupling combination is that the reactances of the post and pad compensate for one another. Another factor that affects the reactance at this point is the backshort of the radial line. If this short circuit is moved away from the point of an equivalent open circuit, its reactance can also be worked into the transition's performance. In that case, only the real part of the impedance still needs to be matched between the radial and microstrip lines. With the fall in characteristic impedance along the radial line, the parallel combination of the peripheral ports should already be matched fairly well.

Using the parallel plate approximation applied earlier, the peripheral transition can also be modelled separately. The width of the parallel plate line provides an equivalent characteristic impedance to that of a single port in the radial combiner as simulated above. Inside this parallel plate section shown in Figure 3.12, a PEC cylinder extends from the conducting roof of the radial line onto the substrate. On the substrate, a 50 Ω microstrip line runs from the post, into a hole in the short circuited end of the parallel plate section.

The ports are set up at first to de-embed the effect of transmission line lengths other than the short circuited parallel plate section. This way, the length of the microstrip line ought not to influence the analysis of the parallel plate back short length. The influence of the microstrip line will be incorporated at a later stage.

Figure 3.13 indicates that the post and microstrip combination is an effective coupling method. Reducing the radial backshort length from 20 mm to 14 mm behind the peripheral posts matches the two interfaces fairly well. The reflection is less than -20 dB and -15 dB over bandwidths of 850 MHz and 1.7 GHz, respectively. The design then continues by investigating the effects of the planned SMA connectors around the structure's periphery.

The model in Figure 3.14 is made from the dimensions in [50]. A volume of air is included to account for the angled drill tip cavity under the substrate. The boundaries are set up such that the top, bottom and SMA-side face are electrically conductive walls. Magnetic walls are placed at the sides of the

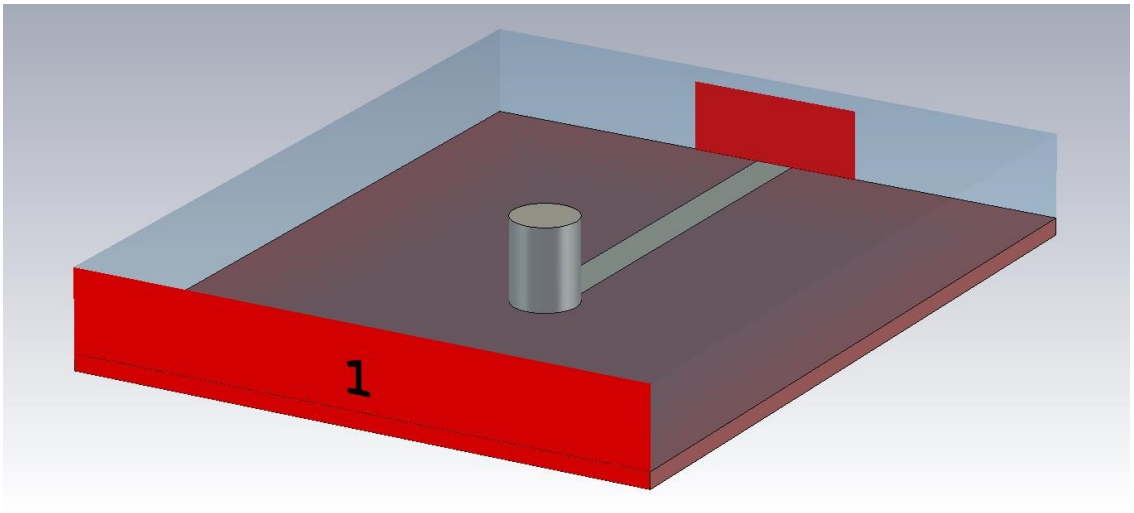

Figure 3.12: An approximation of the peripheral transition to microstrip transmission lines.

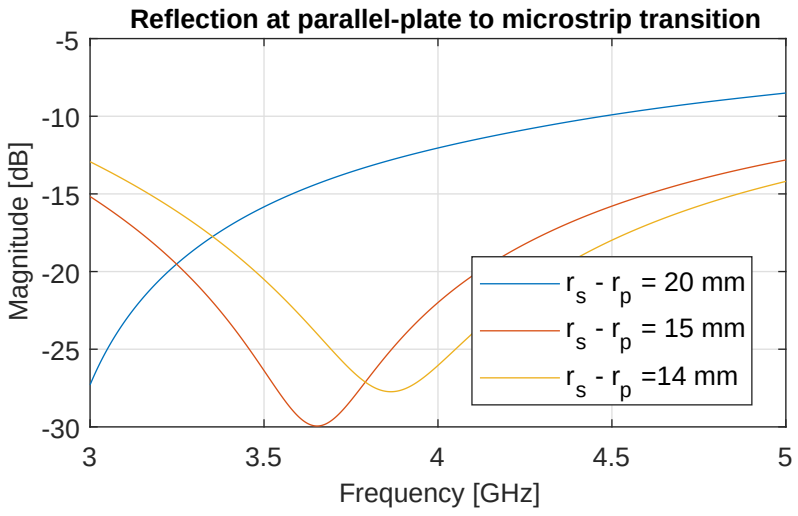

Figure 3.13: Simulation results of the approximated peripheral transition.

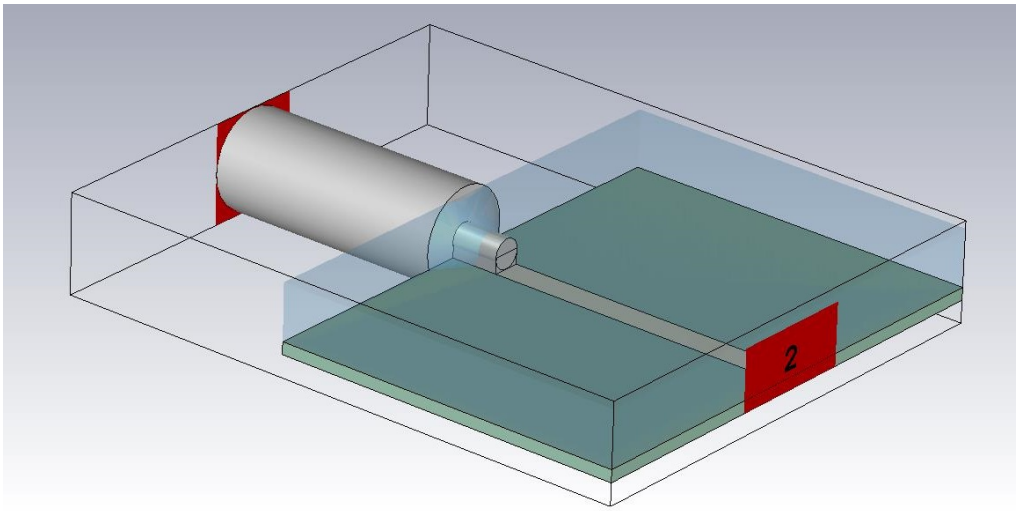

Figure 3.14: The transition from microstrip form factor into the coaxial geometry of an SMA connector.

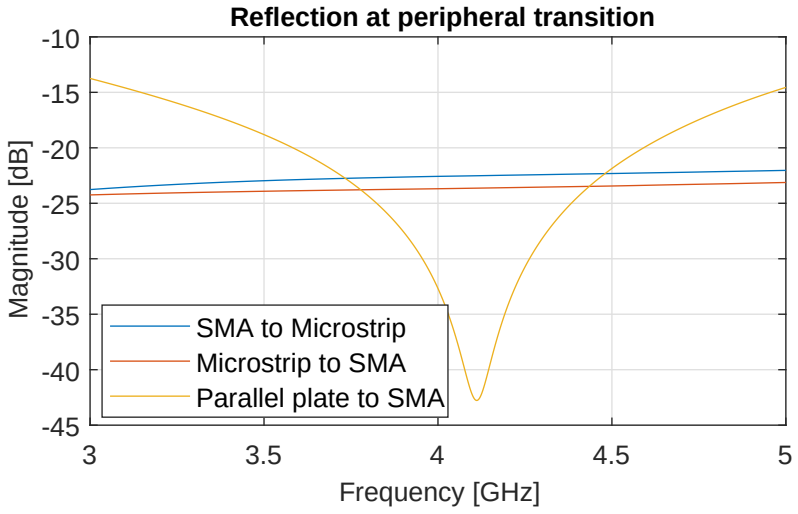

Figure 3.15: The reflection from each side of the microstrip to SMA transition.

substrate, to keep with the parallel plate setup for these piecewise simulation models. The microstrip port sits in an open boundary, so all energy outside the port in that direction is absorbed by the boundary.

The results in Figure 3.15 show that no matching elements are needed for the transition at this time. Reflection across the transition is less than -22 dB over the entire analysed frequency band. The reflection from the two sides differ due to the asymmetric nature of the model with regards to the simulation boundaries.

All the sections that make up each peripheral port are combined in Figure 3.16. An etched pad is included underneath the post, as would be in the manufactured version. This pad has a radius of 1.1 mm, slightly larger than

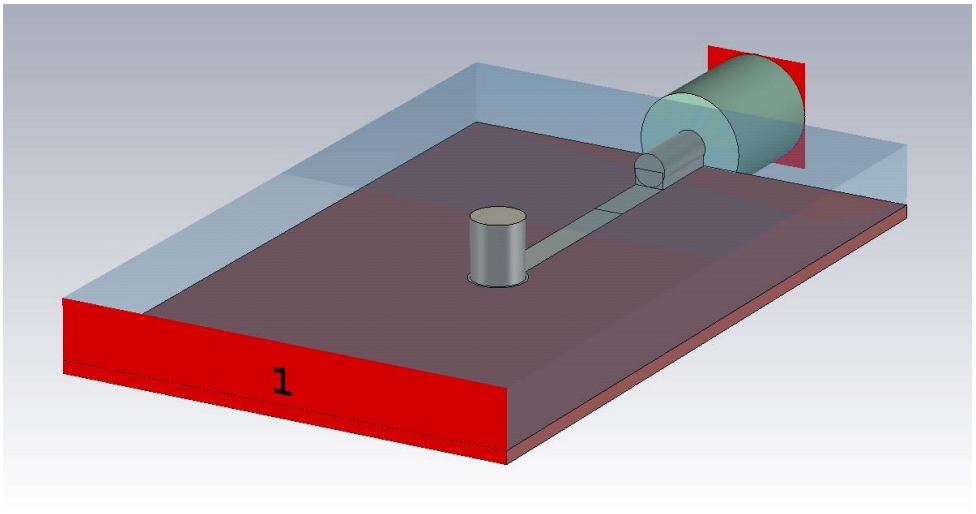

Figure 3.16: The complete peripheral port transition.

the planned 1 mm radius of the post. The posts will be implemented using screws through the top of the combiner. The results of the simulation are also shown in Figure 3.15. The point of minimum reflection from either side of the complete transition is above 4 GHz. The dimensions will however be kept as is for integration of these transitions with the radial section.

3.5 Simulation of the Complete Radial Combiner

Only the posts and microstrip sections will be added to the radial line model at first. This intermediate model is shown in Figure 3.17. Sections of the circular outside wall are flattened to accommodate the flat-plane restriction on the waveguide ports used. These are kept small to allow as much of the geometry to resemble the physical radial structure.

Figure 3.19 indicates that the structure up to this point performs well enough to continue expanding the peripheral ports. The SMA connectors are thus added to the simulation model. Also shown in Figure 3.19 is the result including the connectors. The -15 dB bandwidth is 1.2 GHz. This is 30% of the relative bandwidth, and well over the specified 20%.

A complete, but simplified model is shown in Figure 3.18. This model is expanded with models of the SMA connectors to be used. It is considered simplified because no practical manufacturing considerations have been included. The results are also shown in Figure 3.19. While the minimum reflection coefficient appears to be higher, the effective bandwidth is the same as before the SMA connectors were added. At this point the design needed to be discussed with a machinist to determine a practically realisable solution.

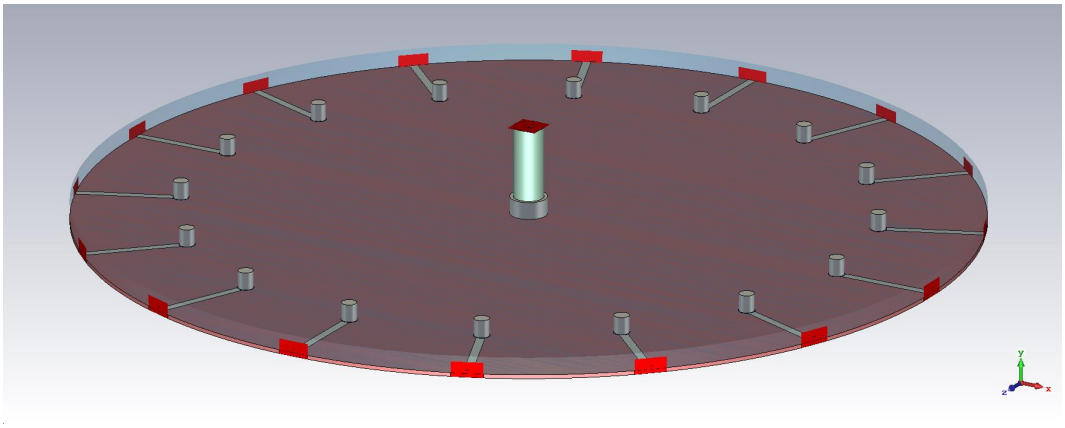

Figure 3.17: The radial combiner model including the posts and microstrip sections of the peripheral ports.

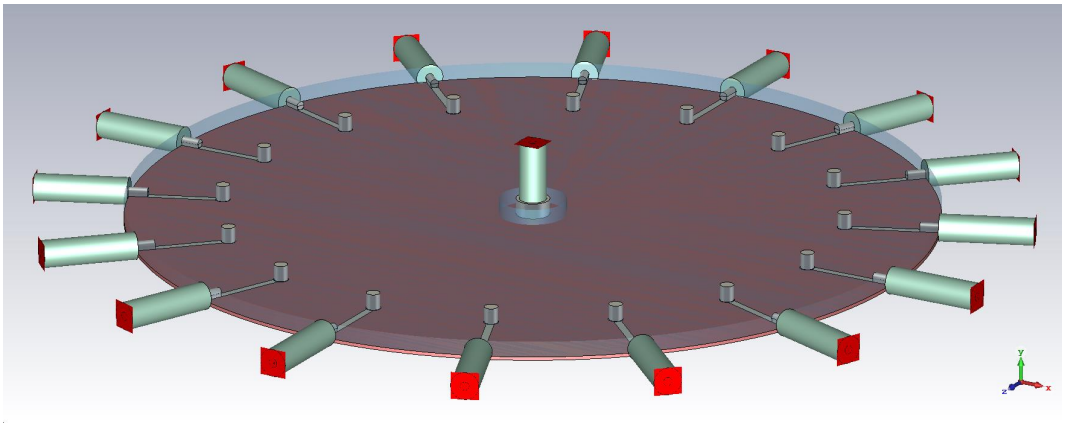

Figure 3.18: The radial combiner model with the complete peripheral transitions.

Most of the feedback from the machinist was related to the centre connector. A cross-section of the modified centre connector, the part inside the radial cavity, is shown in Figure 3.20. Instead of a straight connector body outside, it was suggested to machine away the least possible material from the connector body. This is to preserve structural integrity during the machining. The connector body is thus stepped to the required outside diameter at 1 mm from what would be the bottom end. One can also see the ring etched onto the PCB, which has a surface area slightly larger than the footprint of the connector. The centre via under the inside conductor of the connector is also extended with a pad larger than the face of the conductor.

Other modifications are the peripheral post diameter and the height of the combiner. The peripheral post diameter is adjusted from 2 mm down to 1.9 mm to resemble the actual diameter of M1.5 screws. This is the standard screw with an outside diameter closest to 2 mm. Due to the radial size of

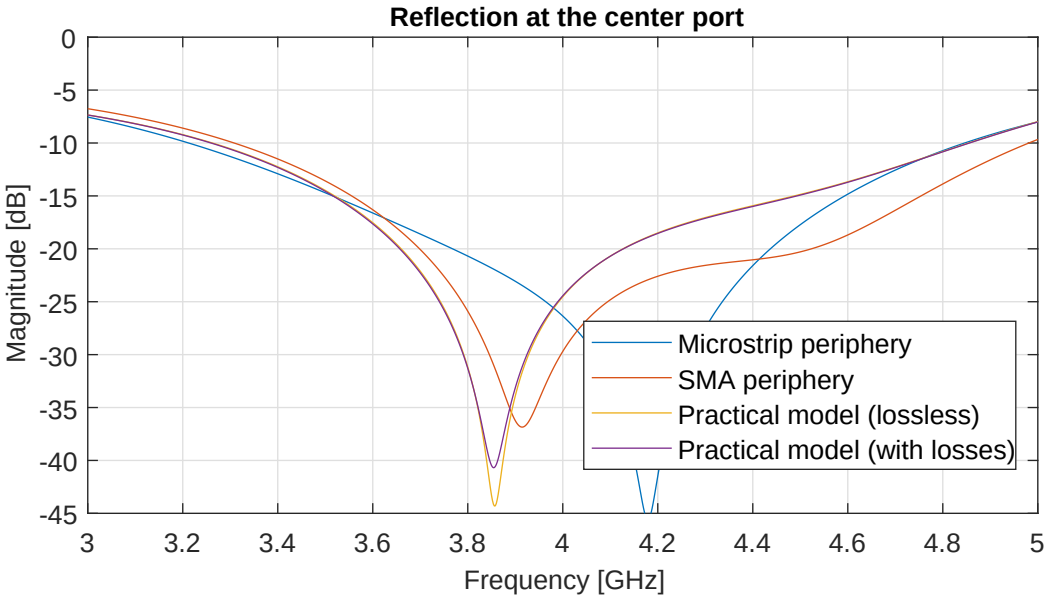

Figure 3.19: The input reflection magnitude at the centre for the progressions of the model.

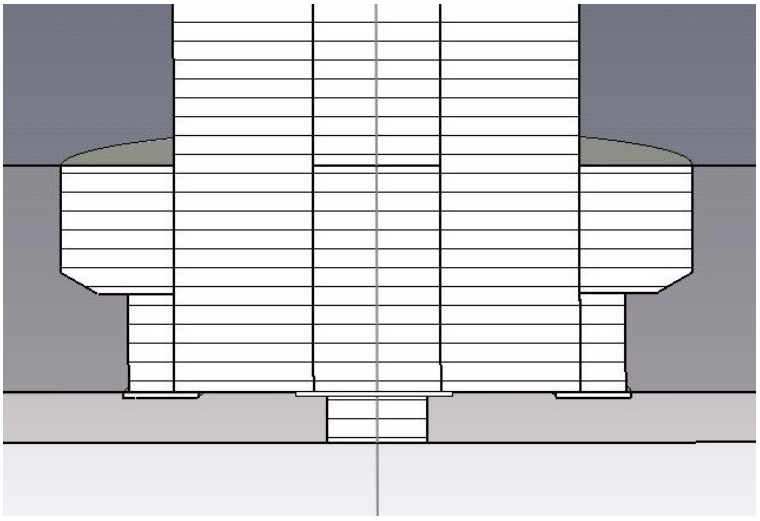

Figure 3.20: A cross-section view of the centre connector modified according to feedback from the machinist.

the combiner and using a manual lathe, the tolerances in the height of the combiner are relatively loose. It is therefore specified in steps of 0.5 mm, and so the current $h = 2.835$ mm is rounded up to $h = 3$ mm. The results of all these practical modifications are also shown in Figure 3.19.

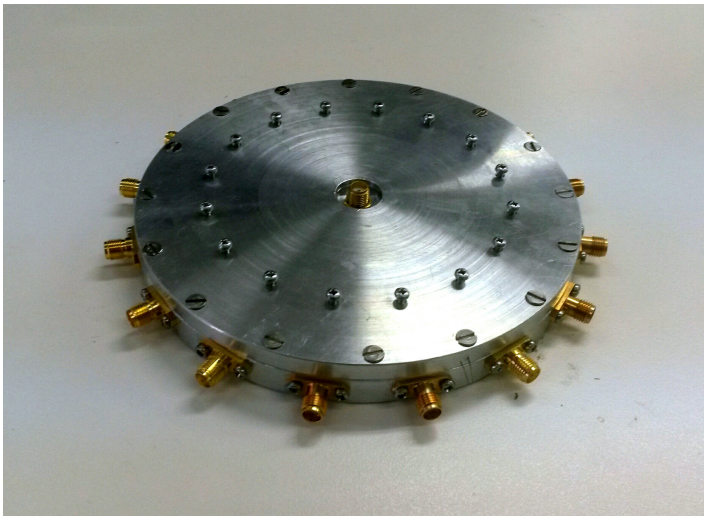

Figure 3.21: The manufactured partially filled radial combiner prototype.

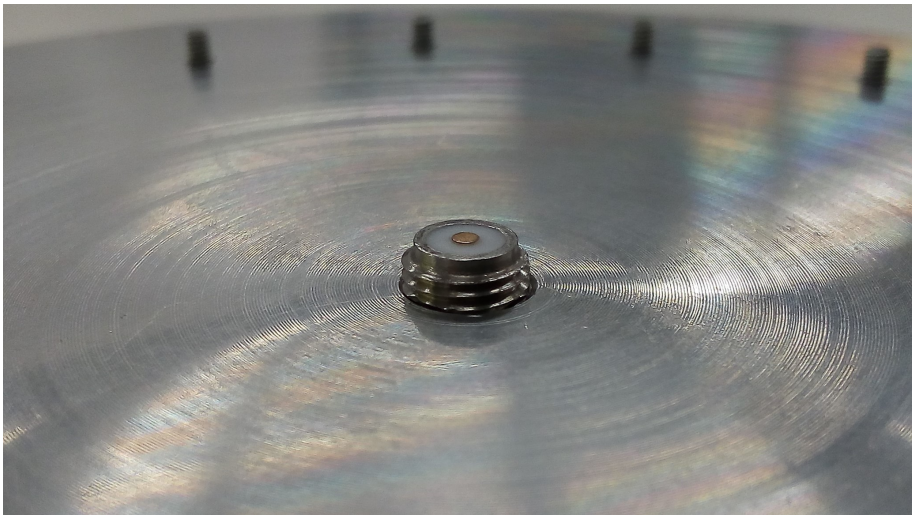

Figure 3.22: A close up view of the modified centre connector.

3.6 Prototype Testing

Figure 3.21 shows the manufactured prototype. The screws protruding the lid are the posts that connect the radial cavity to the microstrip lines. Other visible parts are the centre and peripheral SMA connectors. Photos of the centre connector, inside of the combiner lid, and the installed PCB are shown in Figures 3.22 through 3.24.

The results from testing the prototype will now be looked at. The initial results could be deemed functional, but it did not sufficiently meet the specifications set out in at the start of this chapter. After troubleshooting possible causes, modifications are made to the physical combiner to improve its operation. Significant improvement was made, but the simulated performance could

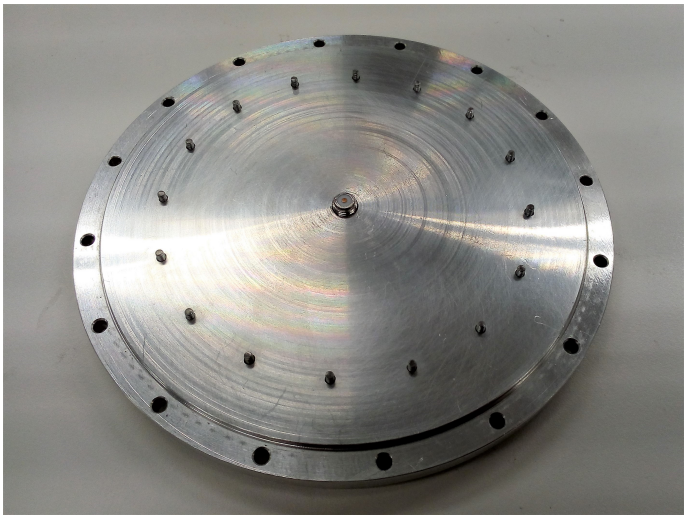

Figure 3.23: The inside of the combiner lid showing the peripheral post screws, centre connector en fastening holes.

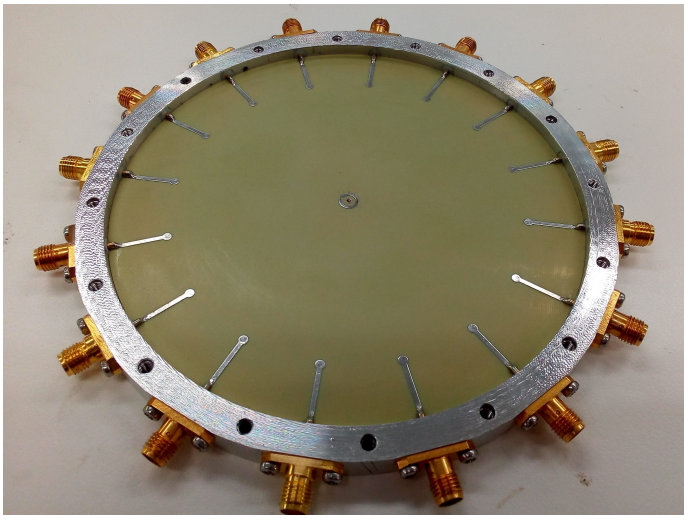

Figure 3.24: The PCB installed inside the radial cavity with the peripheral SMA connectors soldered on and fastened in place.

not be replicated with the physical device.

The initial centre port reflection coefficient ($S_{1,1}$) measurement is overlaid in Figure 3.25 with the expected result from the simulation. First off, the measured results indicates that the combiner achieves an $S_{1,1}$ of less than -15 dB at 4 GHz. The centre frequency is, however, at 3.87 GHz. Another notable concern is that the bandwidth is only 16%. These metrics are significantly lower than expected. It can, therefore, not yet be regarded as a successful execution of the radial combiner design.

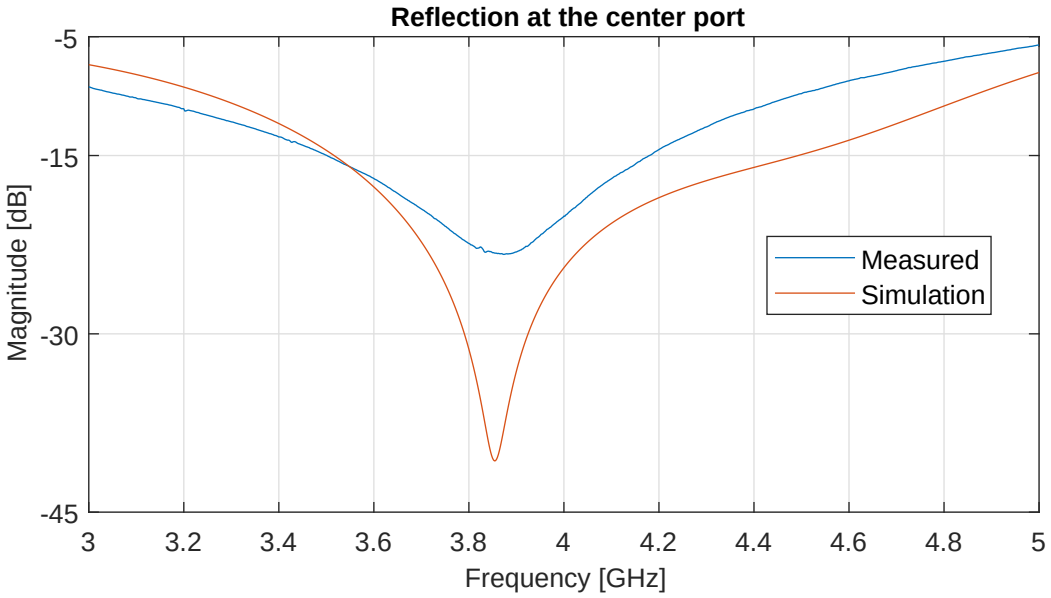

Figure 3.25: Initial measurement of the manufactured combiner.

In an attempt to improve the prototype operation, the simulation dimensions were modified and the results compared with the error in the measurements. Through this process, it appeared that varying the height of the air cavity caused an error that corresponds with the measured results.

The best fit simulation suggested that the air cavity is 0.2 mm too high. The height reduction was implemented in the manufactured model by lowering the cavity wall by 0.5 mm and then stacking shims underneath the combiner lid. This allowed flexibility to test other heights, and possibly revert to the original height if this proved not to be the issue. The measured results are presented in Figure 3.26, where the simulated error is indicated by e_h. It is clear that the cavity height does affect the results, but the inconsistency required further analysis.

Figure 3.27 shows some visible compression at the footprint etched on the PCB. This suggests that too much pressure was applied when fastening the SMA connector of the centre port. If it is assumed that the PCB dielectric underneath the footprint is compressed by this, the shunt capacitance of the

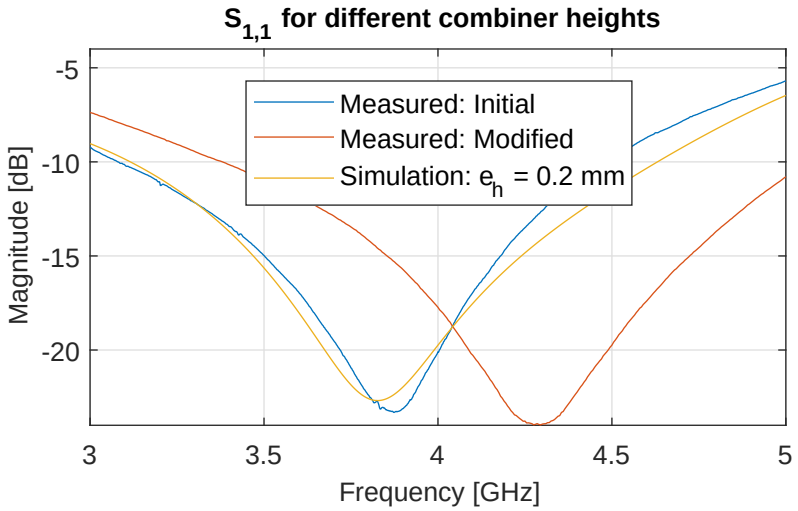

Figure 3.26: Simulation and measurement results of $S_{1,1}$ with varying cavity heights.

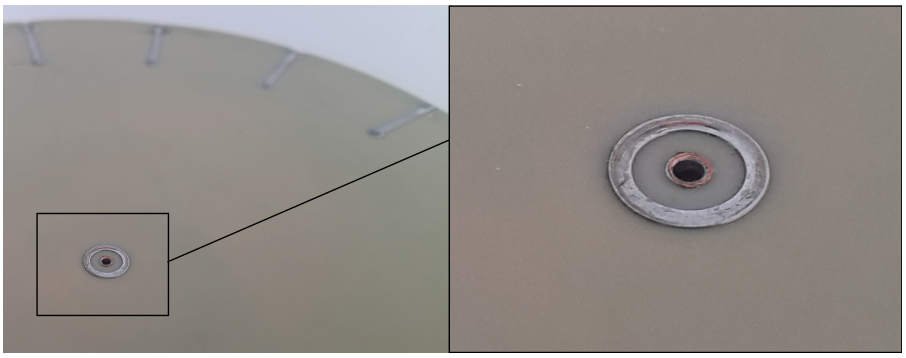

Figure 3.27: Visible compression at the capacitive footprint in the centre of the PCB.

transition is increased as a result. It could then lead to degraded performance of the transition.

To confirm the possible substrate damage, and its effect on the combiner's performance, a new substrate was installed. It must also be noted that different installation procedure was followed with the new substrate. The previous substrate was secured to the combiner with conductive epoxy, and the ground plane was trimmed slightly where the connectors are situated at the edges. These practices are usually applied to ensure correct operation. In an attempt to eliminate unknown factors, however, the new PCB was inserted as is. It is now soldered to the peripheral connector pins and clamped down by the centre connector.

The best result was obtained by reducing the height of the air cavity by 0.2 mm. This shifted the reflection coefficient minimum to 3.98 GHz, which is sufficiently close to 4 GHz. Using the new substrate also improved the final

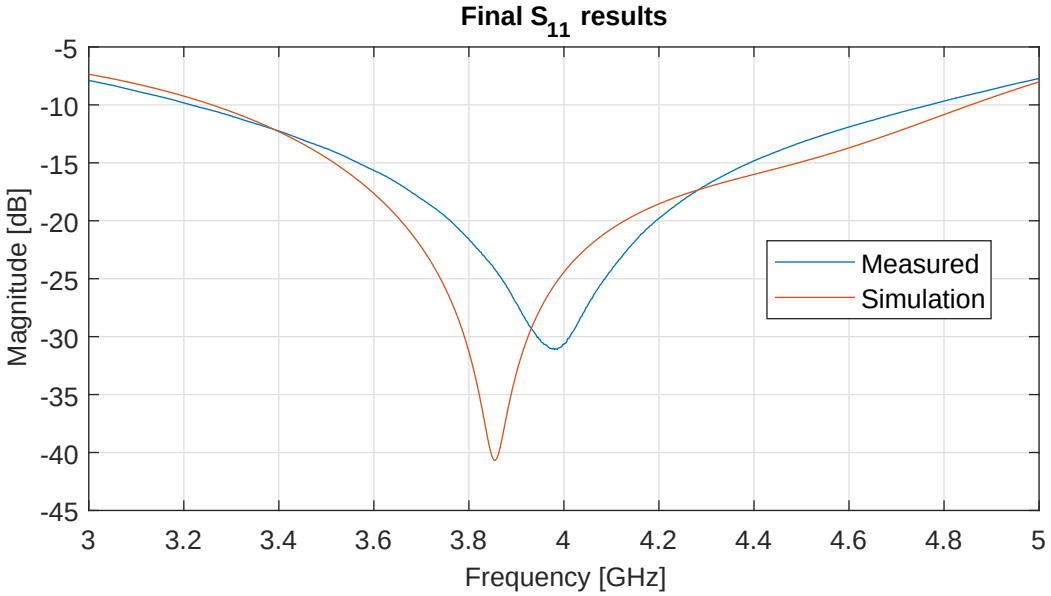

Figure 3.28: The final measured $S_{1,1}$ in dB, along with the simulation results.

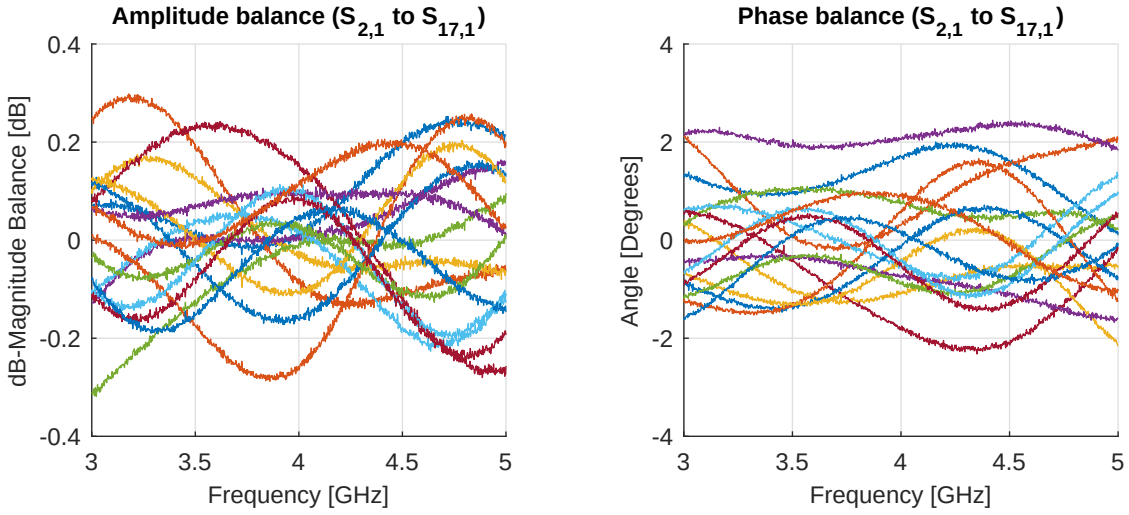

(a) (b)

Figure 3.29: (a) The magnitude balance in dB and (b) the phase balance measured at the peripheral ports of the prototype radial combiner.

measurements. The -15 dB $S_{1,1}$ bandwidth increased from the original 16% to just over 20%, as seen in Figure 3.28.

The subsequent amplitude and phase balances at the peripheral ports are shown in Figure 3.29. The phase balance is shown to be within $\pm 2.5^{\circ}$ and the amplitudes are within ± 0.3 dB. Both these results are well within acceptable bounds for N-way power combiners.

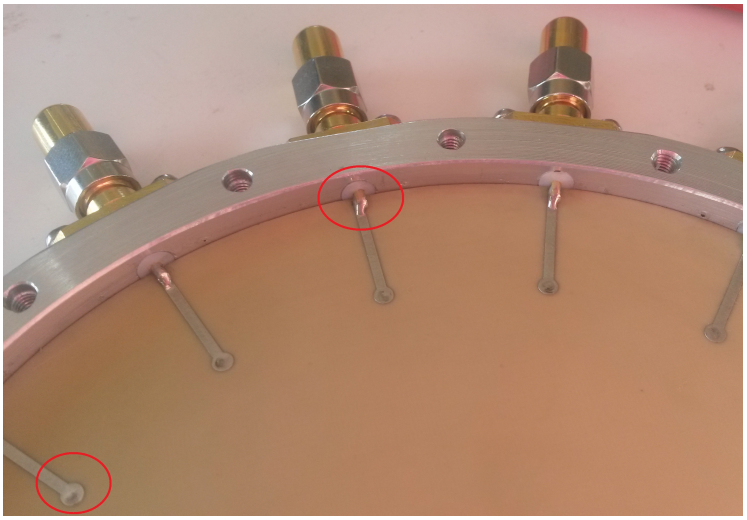

Figure 3.30: Examples of off-centre peripheral posts and SMA pins present in the combiner.

A difference in input reflection bandwidth is still evident between the original simulation model and the final prototype. This is likely due to many aspects in the manual manufacturing process. Some of the SMA pins do not line up exactly with the microstrip lines at the edge of the PCB. The marks on the pads where the screws press onto the PCB to transition from the radial geometry into microstrip also show some misalignment. Examples of these are shown in Figure 3.30.

Part of the degraded performance can still be attributed to the pressure in the centre of the substrate as well. Good electrical contact in this area necessitates firm mechanical contact between the centre SMA connector and the substrate. As such, minimal compression of the substrate is still expected below the capacitive ring. The pressure is kept to a minimum by fastening the centre connector incrementally tighter. With that, the alignment of the centre connector with the ring and via on the PCB is also not exact. Despite these inherent defects, the tuning possibilities afforded by adjusting the combiner height proved to be useful.

Chapter 4

Design of an Isolated Radial Combiner

The lack of isolation among peripheral ports of axially symmetric combiners is one of their major drawbacks. Another is the relatively high asymmetric input reflection. One peripheral port was excited on the non-isolated combiner prototype and the coupling to other peripheral ports measured. The results in Figure 4.1 indicates that, for an asymmetric excitation at the periphery, much energy is coupled to other peripheral ports. Figure 4.2 shows the accompanying asymmetric input reflection of the peripheral ports. The latter was measured by exciting only one peripheral port, while all other ports are terminated in matched loads.

A planar periphery in the radial combiner, as in Chapter 3, enables the use of the general N-way isolation technique in [22] to isolate the peripheral ports from each other. The same broadside diamond couplers from [23] will be used in this design.

An adaptation of the concept in Figure 2.4 for implementation in radial geometry is shown in Figure 4.3. The adaptation utilises two back-to-back radial combiners, with the bulk of the isolation network at the periphery of the configuration. Further details of the implementation will be developed as required.

Simulations of individual components will be run, after which the radial section is to be systematically augmented. All the components are then assembled into a 3D model of the complete isolated radial combiner. Once practical simulation results are obtained, a prototype will be manufactured to confirm the performance of the isolated radial combiner.

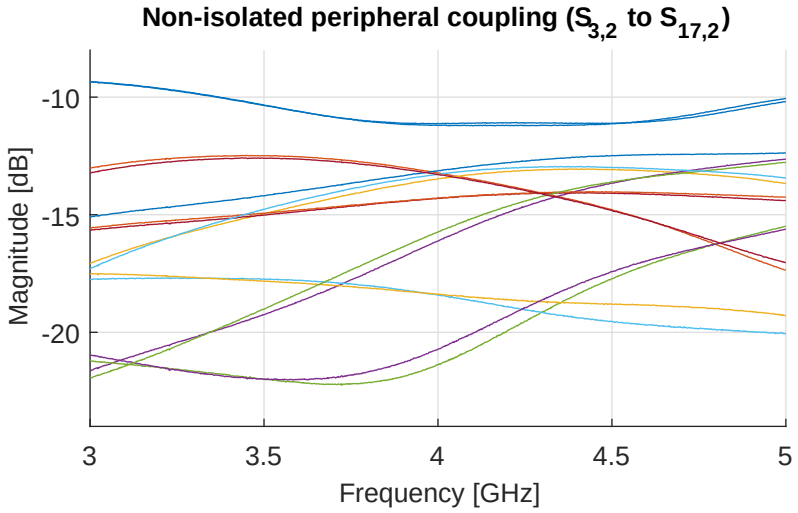

Figure 4.1: Measured coupling among peripheral ports of the non-isolated radial combiner.

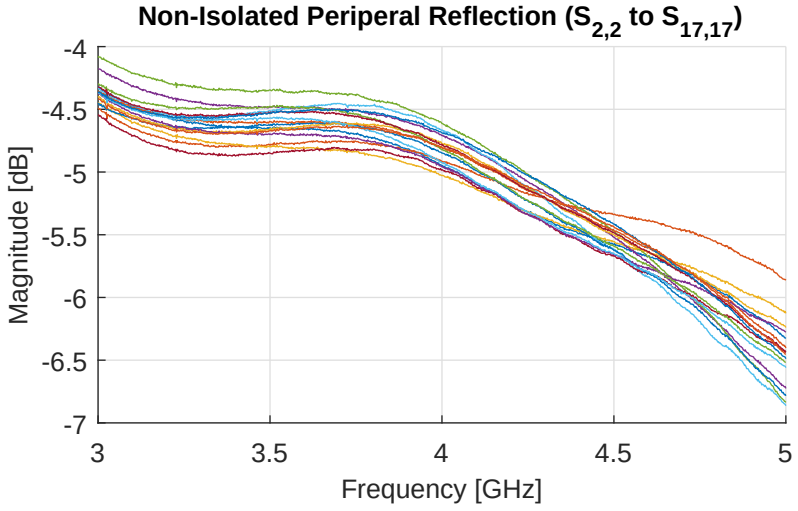

Figure 4.2: Measured reflection at peripheral ports of the non-isolated radial combiner.

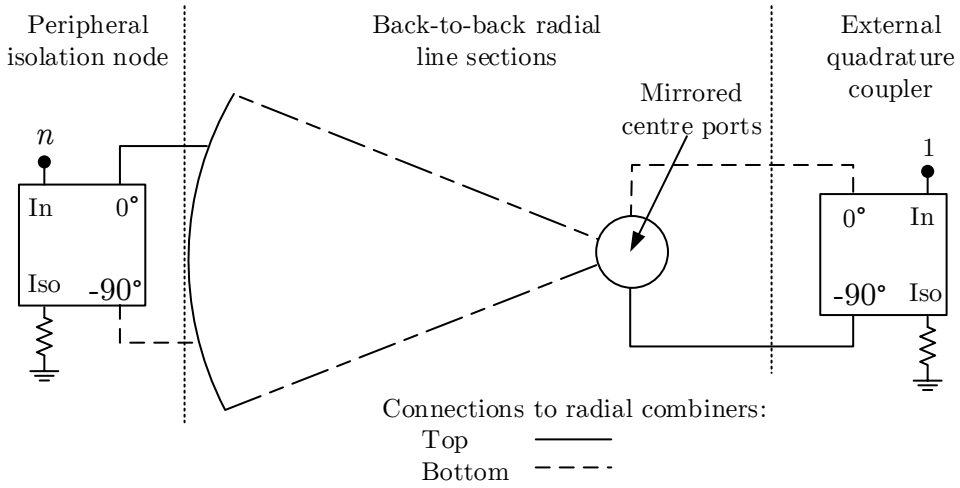

Figure 4.3: Concept layout of an isolation network based around the radial combiner.

4.1 Centre Port

The centre port of each radial sections is kept much the same as in Section 3.3. Figure 4.4 shows a sectioned view of the back-to-back SMA-to-radial transitions. Minor adjustments will made according to simulation analyses and practical suggestions from the machinist.

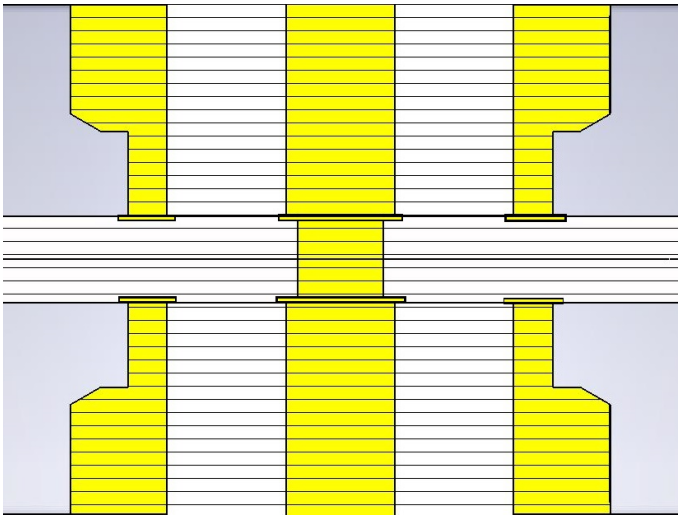

Figure 4.4: The mirrored centre ports of the two radial line sections.

One suggestion is to change the diameters of the capacitive ring. The final outer radius of the capacitive ring in Chapter 3 is only 0.05 mm wider than the connector body at that point. In contrast, the inner radius is 0.2 mm smaller. This will be evened out if the inner radius of the ring is enlarged to

1.9 mm. Simulations indicate that the new outer radius at this point should be 2.62 mm. This evens out the radial protrusion of the capacitive ring to ≈0.1 mm on both sides. The desired effect of this is slightly more tolerance to misalignment of the centre connector

4.2 Radial Line Wall

The peripheral coupling posts are kept as is, and attention is turned to crossing the radial line boundary. This is to let the signal pass between the radial line sections and the isolation network. Interference between these sections must also be kept to a minimum. To achieve this, the radial line sections should effectively be short circuited at their periphery, while allowing the individual microstrip lines to extend beyond this short circuit.

The simplest concept would be to cut away tunnels in the edge of the radial line where the microstrip lines can pass through. However, due to the manufacturing limitations, it would be most difficult to machine these tunnels. A solution is therefore sought using the technology available in PCB manufacturing process.

Figure 4.5 illustrates a possible passage out of the radial line section. The conductive wall that short circuits the radial line is effectively extended to the ground plane using plated through-hole vias. The microstrip line then transitions into stripline to pass under the surface of PCB and between the shorting vias. Once beyond the wall of the radial section, the transmission is converted back to microstrip line from where it can be connected to a broadside hybrid quadrature coupler. The performance of this transition is shown by the reflection across the boundary in Figure 4.6. It presents a reflection of less than -25 dB from either side of the boundary across the entire bandwidth of interest.

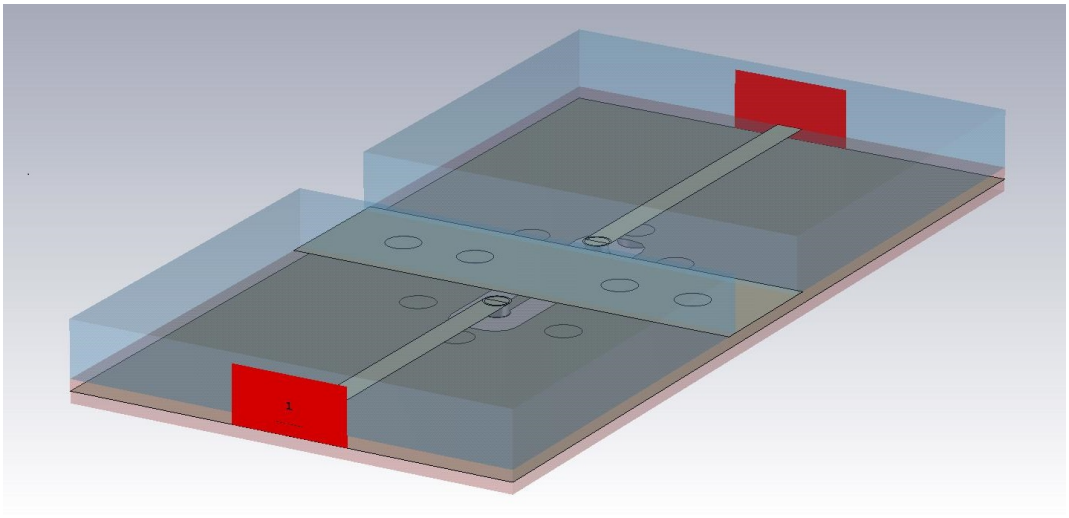

Figure 4.5: A parallel plate model of the stripline passing under the radial combiner wall.

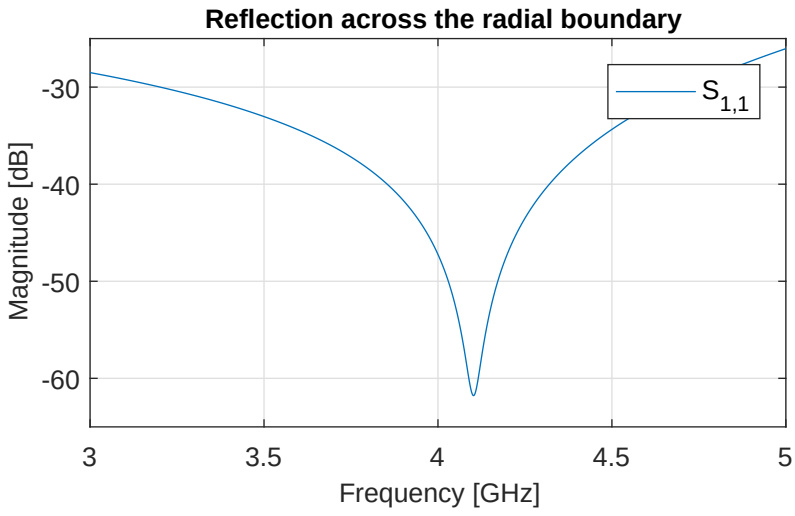

Figure 4.6: The reflected power across the radial line boundary.

4.3 3 dB Hybrid Quadrature Coupler

Now, the geometry and placement of the hybrid quadrature couplers can be designed. The dimensions for an older rectangular coupler [52] are determined as a first step. For a 3-dB coupling strength to the through and coupled ports, the required odd mode impedance is $Z_o = 20.7\,\Omega$. The substrate used in the design has a relative dielectric constant of $\varepsilon_r = 3.5$.

An equivalent parallel plate transmission line is used to represent the odd-mode coupler. The line height will be taken as the substrate thickness in the non-isolated iteration of the combiner, $d = 0.508$ mm. The rectangular patch width is then calculated as

$$w_p' = \frac{\eta d}{Z_o} = 4.939 \text{ mm}. \tag{4.1}$$

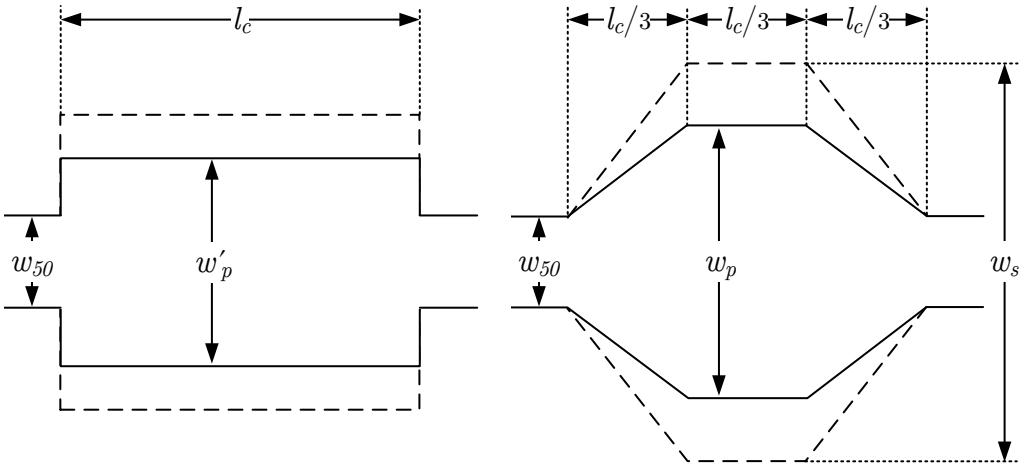

(a) (b)

Figure 4.7: Dimensions of the (a) rectangular [52] and (b) diamond shaped [23] broadside hybrid quadrature couplers.

The patch width is then translated to the diamond coupler setting the areas of both shapes equal [23], so that

$$w_p' l_c = w_p \frac{2}{3} l_c + w_{50} \frac{l_c}{3}. \tag{4.2}$$

The coupler length $l_c = \frac{\lambda}{4} = 10.015$ mm at midband, can be eliminated from (4.2). The diamond patch width shown in Figure 4.7, is then calculated by rearranging (4.2) to yield

$$w_p = \frac{1}{2}\left(3w_p' - w_{50}\right) = 6.834 \text{ mm}, \tag{4.3}$$

where $w_{50} = 1.15$ mm is the width of the 50 Ω microstrip transmission line.

The slot width determines the even-mode impedance of the coupler. Calculating this dimension is non-trivial and left for numerical calculation in the 3D simulations. As such, the slot width is not determined for the rectangular coupler, but will only be done for the diamond shaped coupler.

A 3D simulation is used to tune the dimensions of the coupler. The model used for these simulations are shown in Figure 4.8. Tuning stubs are added to improve the impedance matching of the couplers. Also note the orientation of the microstrip lines at each port of the coupler. This layout is a better representation of the ensuing implementation.

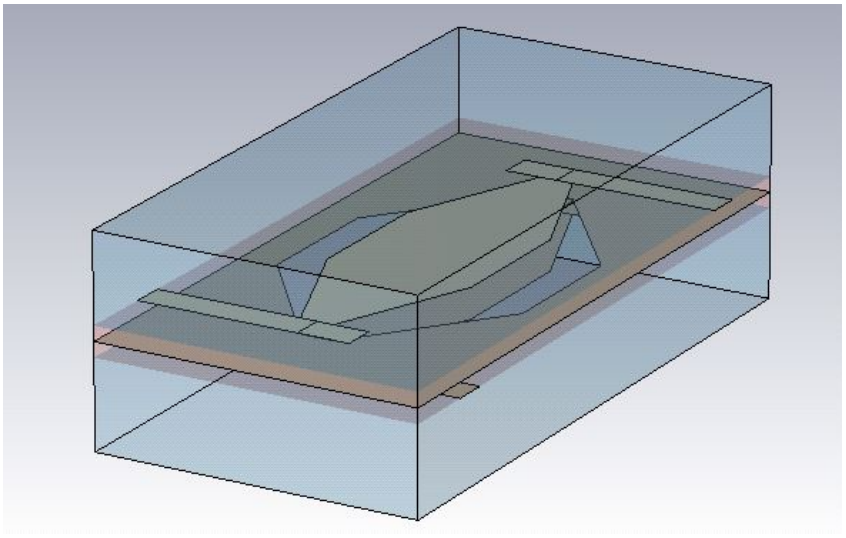

Figure 4.8: CST model of the hybrid quadrature coupler used in the N-port isolation network.

The through and coupled signals, $S_{2,1}$ and $S_{3,1}$ have a magnitude difference of less than 1 dB over the operating bandwidth. The power reflected at the input port and transmitted to the isolated port are well below -25 dB across a 20% relative bandwidth. These parameters are indicative that the coupler should perform as expected in the isolation network.

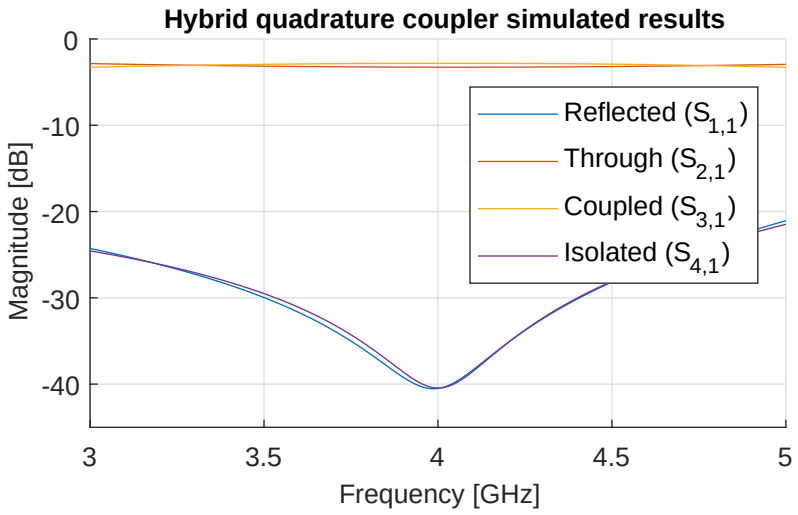

Figure 4.9: Simulated S-parameters of the hybrid quadrature couplers

4.4 Integrated Isolation Node

Before expanding the radial combiner with the peripheral isolation network, a parallel plate model of one peripheral node is tested. This node represents the signal path from the posts inside the radial cavity, through the stripline boundary crossing and across the hybrid coupler. The model is shown in Figure 4.10. Here the signal is expected to split across the coupler and appear at ports 2 and 3 as -3 dB signals offset with 90° from each other.

Results from the simulation are shown in Figures 4.11 and 4.12 The reflected power from either side of the node is at most -15 dB over a 20% fractional bandwidth, as seen in Figure 4.11. The parameter S_{41} in Figure 4.11 is an indication of the level of unwanted coupling between the two radial combiners at each node. This is well below -20 dB across the entire analysed bandwidth.

Figure 4.12 shows the subsequent quadrature performance of the coupler embedded in the node simulation. As expected, the coupling to ports 2 and 3 is within ±0.5 dB of each other, and the phase difference is consistently within 90±2.5°. The minimum coupling in the 20% bandwidth is -3.45 dB. This performance is considered sufficient to proceed with the design.

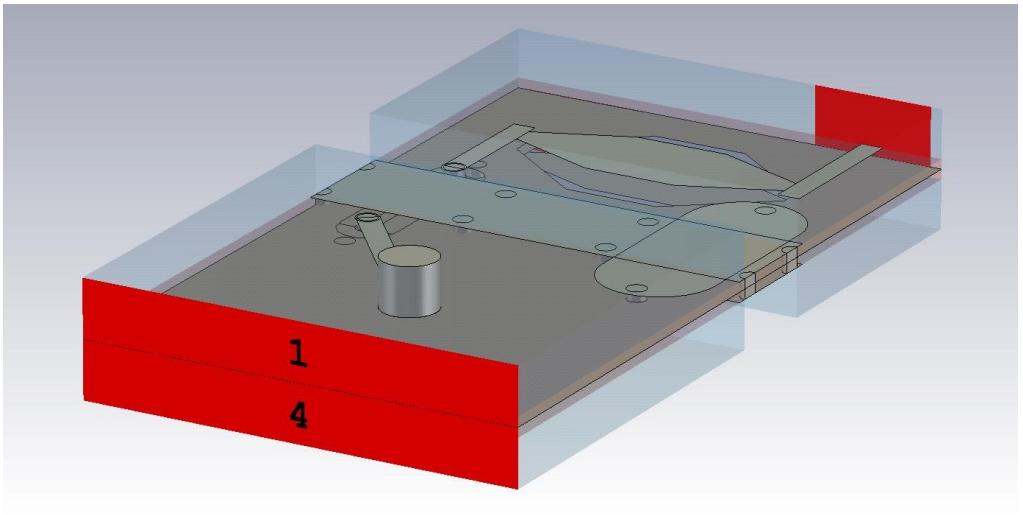

Figure 4.10: A parallel plate model of the transition to the hybrid quadrature coupler.

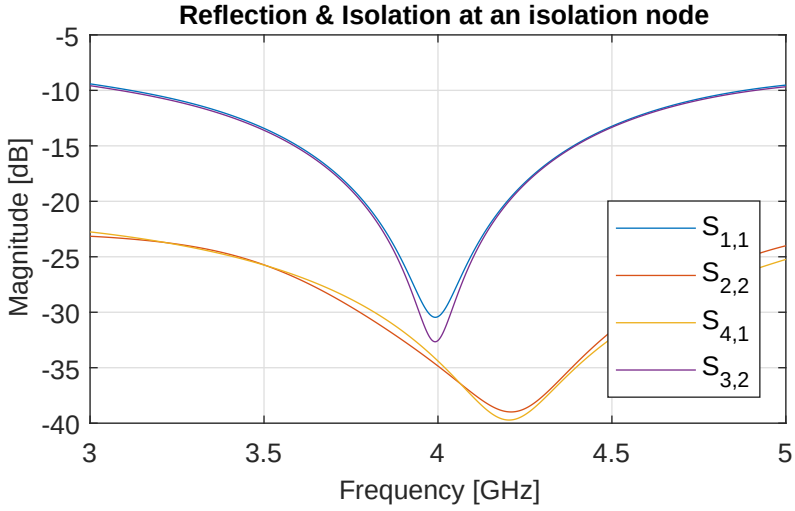

Figure 4.11: The reflection ($S_{1,1}$ and $S_{2,2}$) and isolation ($S_{4,1}$ and $S_{3,2}$) performance of the hybrid quadrature coupler embedded in the peripheral node.

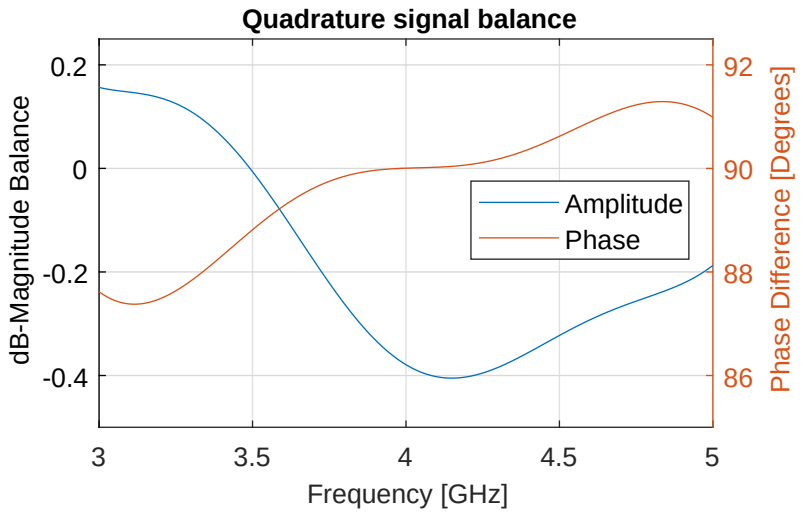

Figure 4.12: The amplitude and phase results of the simulated quadrature signals at the peripheral node.

4.5 Peripheral SMA Connector

The SMA connector transitions on the periphery will need modification for this version of the combiner. For the design in Chapter 3, anything protruding beyond the bottom of the PCB was shorted to ground by the combiner base. The isolation network, however, requires that two combiners be stacked back-to-back. As such, the dielectric of the SMA connectors can launch unwanted fields into one of the combiners.

Figure 4.13 shows a solution to guide the fields in the lower part of the connector into the microstrip line. The conductive ground plane in the middle of the substrate is the boundary between the two combiners. This plane has a section cut away at each SMA connector, as shown. An extra grounded patch is etched onto the respective outer surfaces of the substrate. These patches are connected to the ground plane using plated vias. The via underneath the microstrip line ends blind in the ground plane. Those closer to the edge are through-hole vias to aid conduction between the enclosure and the ground plane. The substrate is excluded from the image to expose the vias and extra ground patch.

The transition approximation model is set up to also measure the energy coupled into the wrong cavity. Energy absorbed at the third port is representative of that. The performance of the transition is displayed in Figure 4.14, where $S_{1,1}$ is representative of the reflection at both the microstrip and SMA ports, and $S_{3,1}$ indicates the amount of power transmitted into the wrong cavity. These simulation results suggest that the proposed SMA transition is functional.

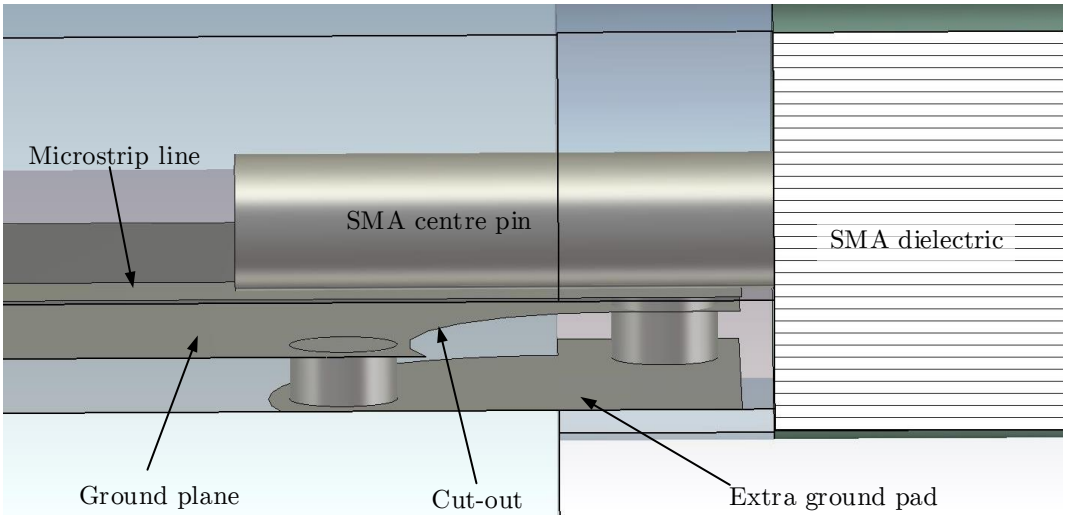

Figure 4.13: The adapted peripheral SMA transition.

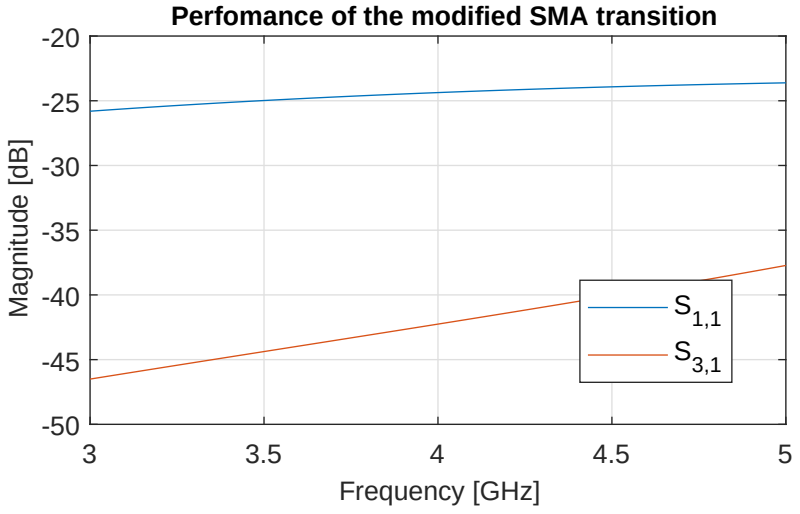

Figure 4.14: S-parameter simulation results of the microstrip to SMA transition for the multilayer PCB.

4.6 Complete Isolated Radial Combiner

Before the design could be manufactured, the PCB layout had to be modified. The layout used for the model of the peripheral node at this point consists of three copper layers, separated by two layers of substrate. This configuration is, however, impossible to manufacture at the available facility. The company advised that the design be changed to make use of four copper layers, separated by substrates as shown in Figure 4.15.

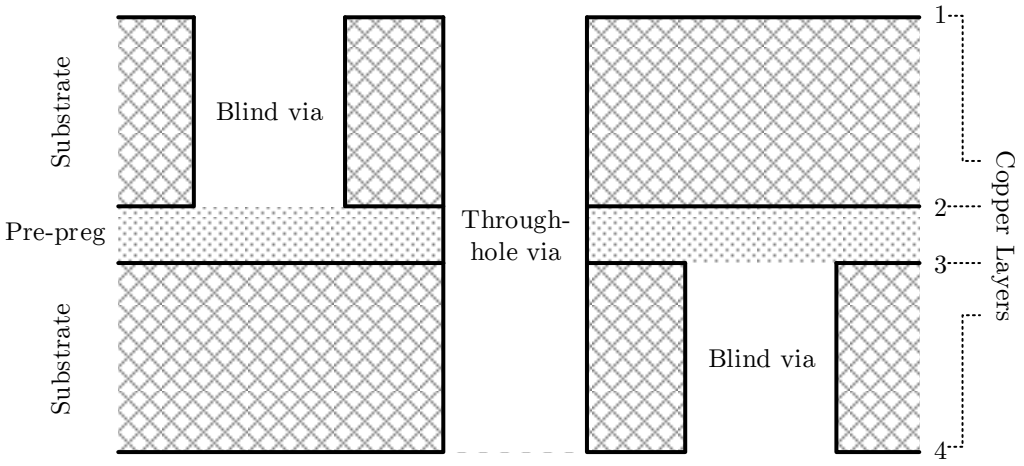

Figure 4.15: Substrate and copper layout as proposed by the PCB manufacturing company.

This way they can make the top and bottom sections, then stack them together with a layer of pre-impregnated adhesive. This middle layer is usually thin, less than 0.1 mm, but still significant in high frequency applications. Copper layer 2 is chosen as the ground plane that separates the combiners in this design. The centre transition ring and the microstrip lines of the bottom combiner, where the adhesive effectively adds to the substrate thickness, were thus widened appropriately.

The required substrate layout also brings about limits as to how vias can be routed. Blind vias can extend only between copper layers 1 and 2, or 3 and 4, respectively. Any other connection would require a through-hole via. This limitation is important in laying out the stripline sections at the radial line boundary. Furthermore, the manufacturing house advised to use as few blind vias as possible, as these are more complex to manufacture and drive up the cost. These factors were incorporated, and a top view of the modified peripheral node of the complete combiner is shown in Figure 4.16.

Notice the vias marked by a red 'x'. These were blind vias under the microstrip lines in Figure 4.10, now modified into offset though-hole vias for

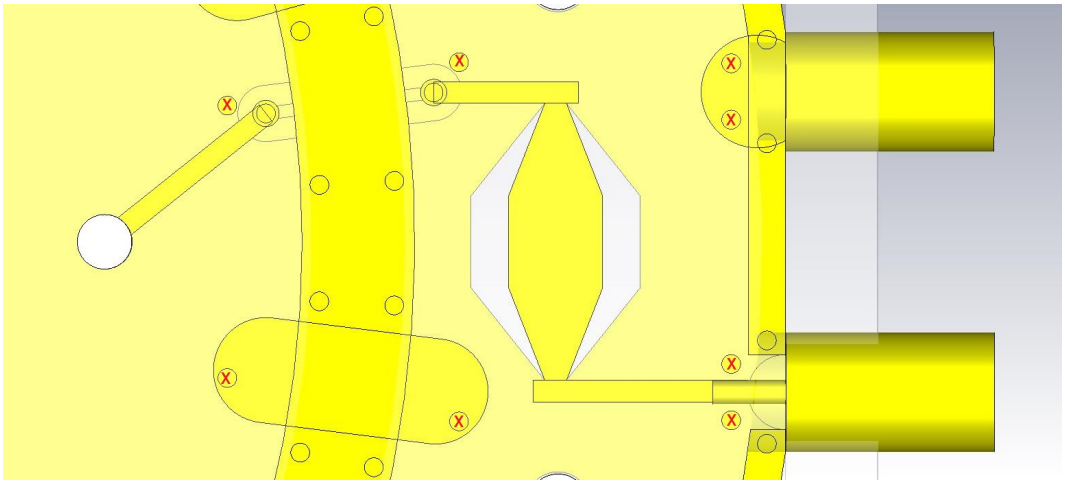

Figure 4.16: The peripheral node modified to accommodate the PCB limitations.

manufacturing. The minimum blind vias are kept only to connect the microstrip lines at the radial boundary to the respective striplines.

The bulk of the complete design is shown in Figure 4.17. The pins between the hybrid couplers represent screws that will be used to fasten the housing. A secondary purpose of the pins is to limit the possibility of a standing field being excited along that cavity.

Missing from the design is the external hybrid quadrature coupler that links the two centre ports of the combiners. This coupler and the coaxial transmission lines that link it will be off-the-shelf components. An ideal coupler and measured models of the transmission lines will be used to check the isolation performance of the complete system. The isolation will be checked in AWR Microwave Office [53] using a Touchstone model of the simulation in CST. This route saves time on the design and simulation of the external components of the isolation network.

The simulated results in Figure 4.18 show that each of the radial combiners in the compound design function well enough to proceed. Also shown in Figure 4.18 is the input reflection coefficient of the complete system analysed in AWR. The latter results are taken at the two ports on the external quadrature coupler. Then, Figure 4.19 shows the expected isolation among the peripheral ports. An improvement of at least -10 dB can be seen in the least isolated ports from the results in Figure 4.1 to that displayed in Figure 4.19.

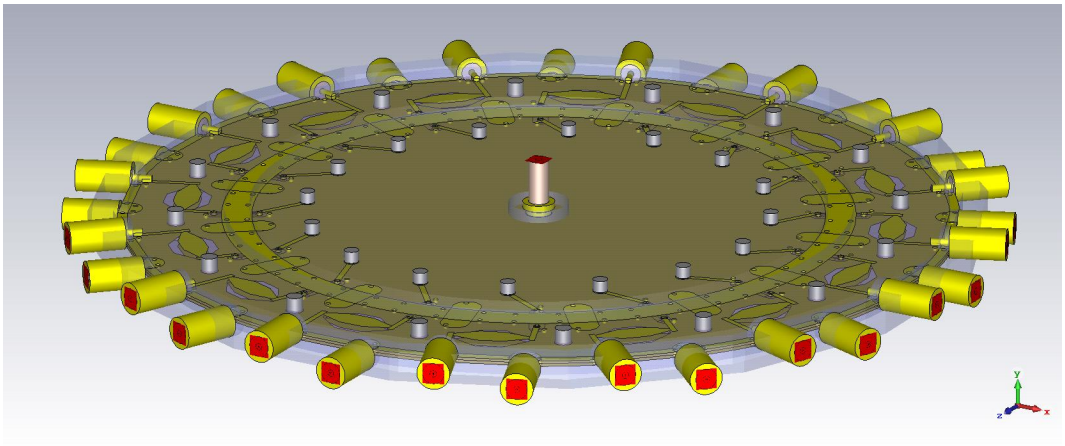

Figure 4.17: The simulation model of the back-to-back radial combiners and the internal components of the isolation network.

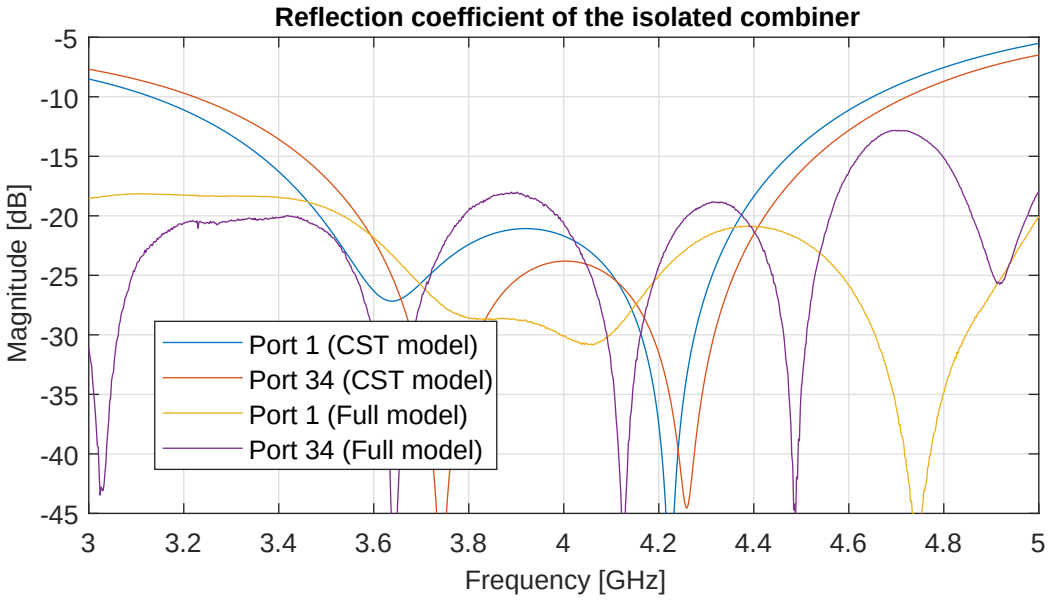

Figure 4.18: The simulated reflection results of the full isolated radial combiner.

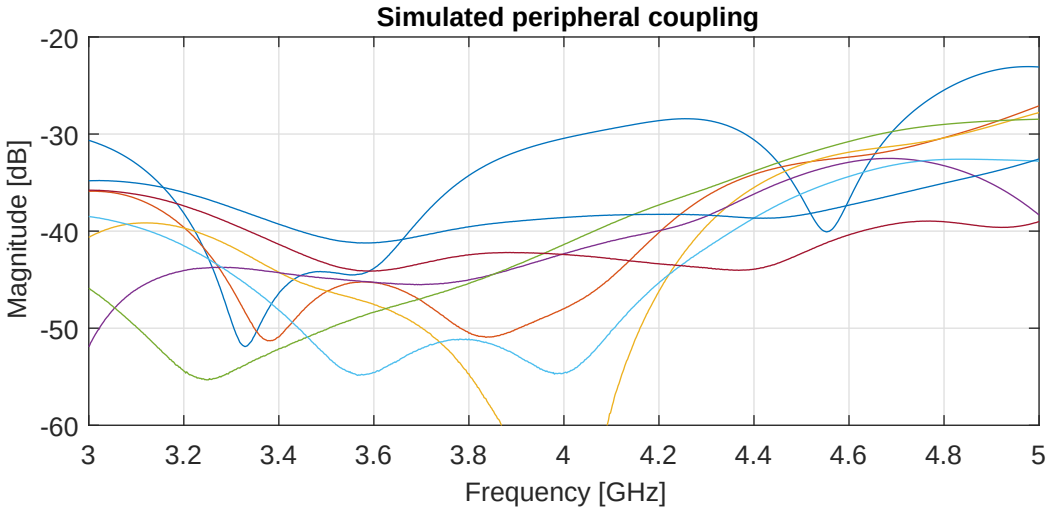

Figure 4.19: The peripheral isolation performance of the complete isolated radial combiner.

4.7 Prototype Testing

All the simulation results point to a functional isolated combiner, and so a prototype was again manufactured. The physical prototype is shown in Figure 4.20. Figure 4.20(a) shows the external coupler and cables that complete the isolation network. One side of the internal components is shown in Figure 4.20(b), where the integrated hybrid couplers, radial line crossing and peripheral posts can be seen.

The device is passive and exhibit reciprocity. As such, the measurements were obtained by testing the device as a power divider but are representative of its power combining capability. The combiner displays a functional input reflection in Figure 4.21, where $S_{1,1}$ is below -18 dB over more than 1.9 GHz of the 2 GHz bandwidth analysed. The average transmission from the centre port to each peripheral port is above -13.1 dB, over a fractional bandwidth of 27%. The transmission expected from an ideal 16-way combiner is -12 dB.

The isolation results of the prototype are on par with the simulations. For a better interpretation of the isolation results, the average coupling was calculated of sets of ports offset by the same number of positions. This is done because the symmetry of the device yields repetitions of various coupling patterns. As an example, the coupling between ports 2 and 4 resembles that between 6 and 8, and so forth. In Figure 4.22, it can be seen that weakest average peripheral isolation is above 21 dB, while the isolation across the required 20% bandwidth is better than 27 dB. Isolation is considered here to be the negative of the coupling strength in dB.

The improvement in peripheral port reflection when individually excited is also significant. Figure 4.23 shows that the isolated combiner has peripheral input reflection more than 10 dB less than that of the non-isolated combiner

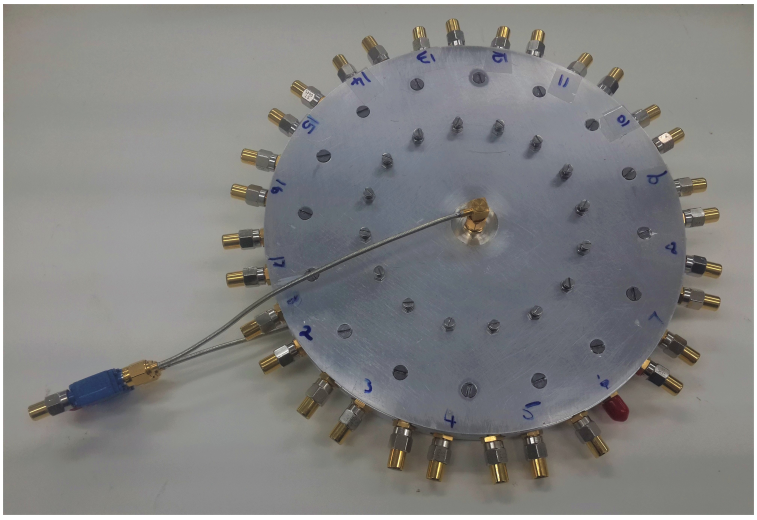

(a)

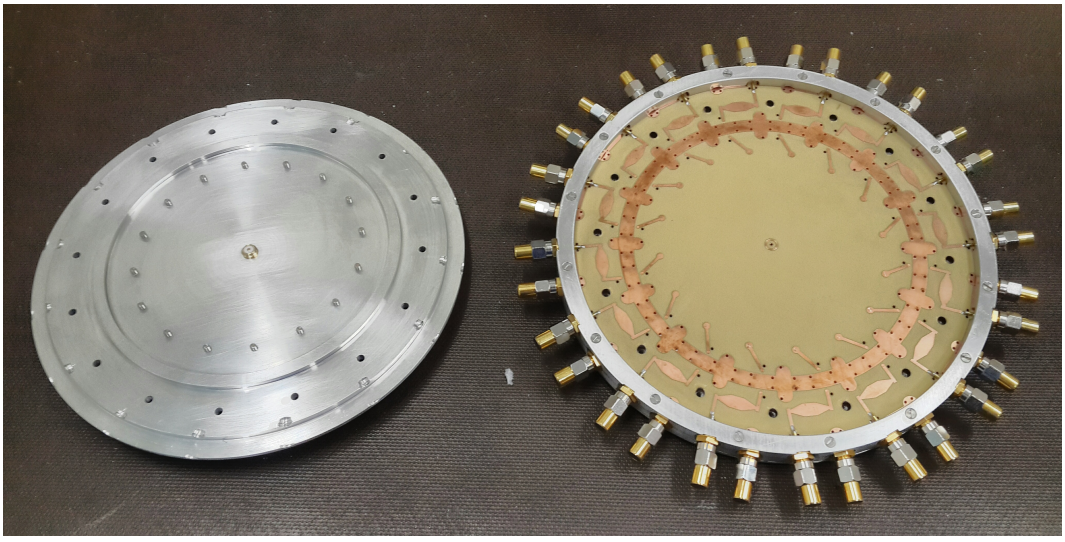

(b)

Figure 4.20: The completed prototype of an isolated radial power combiner, showing (a) the internal isolation components and (b) the fully assembled device.

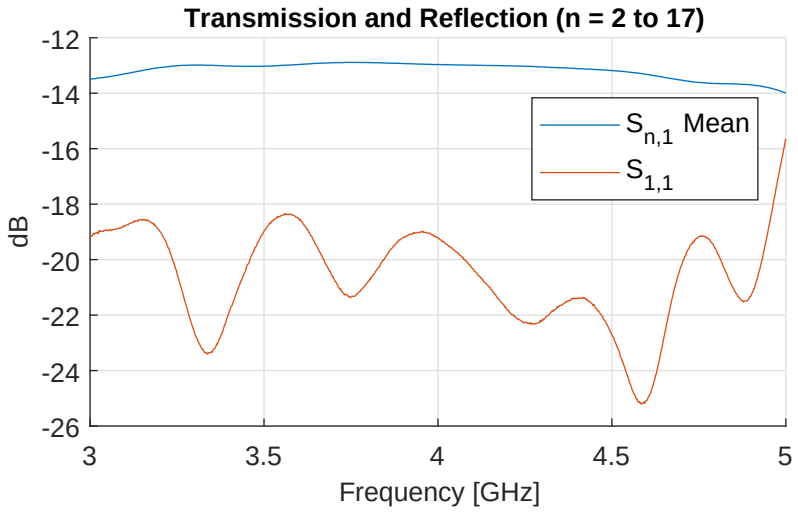

Figure 4.21: The transmission and reflection performance of the complete isolated combiner

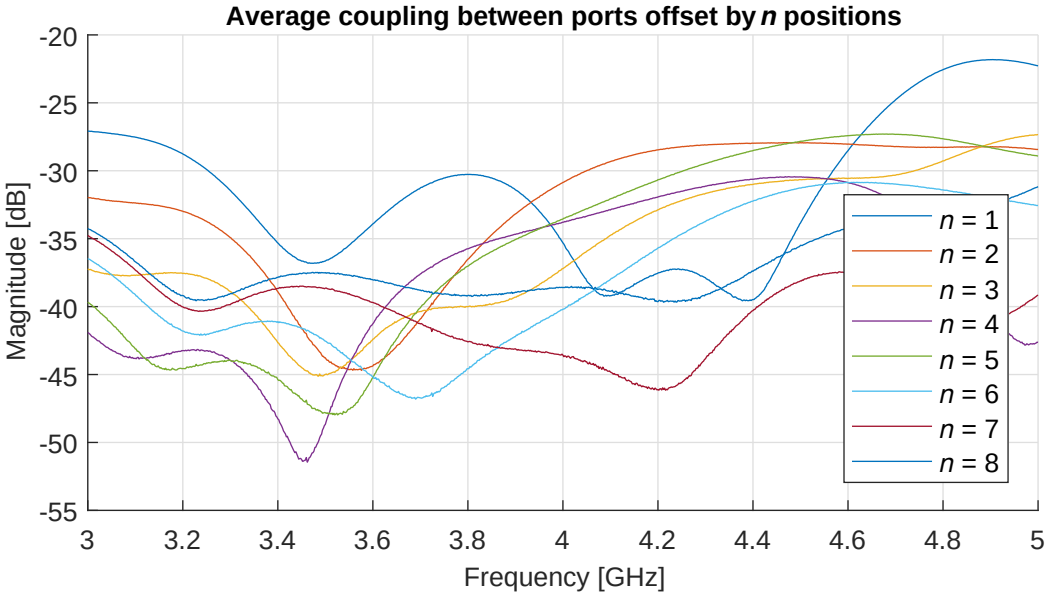

Figure 4.22: The average coupling measured between electrically symmetric sets of peripheral ports.

shown in Figure 4.2. The highest reflection among the measurements in Figure 4.23 is -14.7 dB, and the average of all the measurements is below -15 dB across 50% bandwidth.

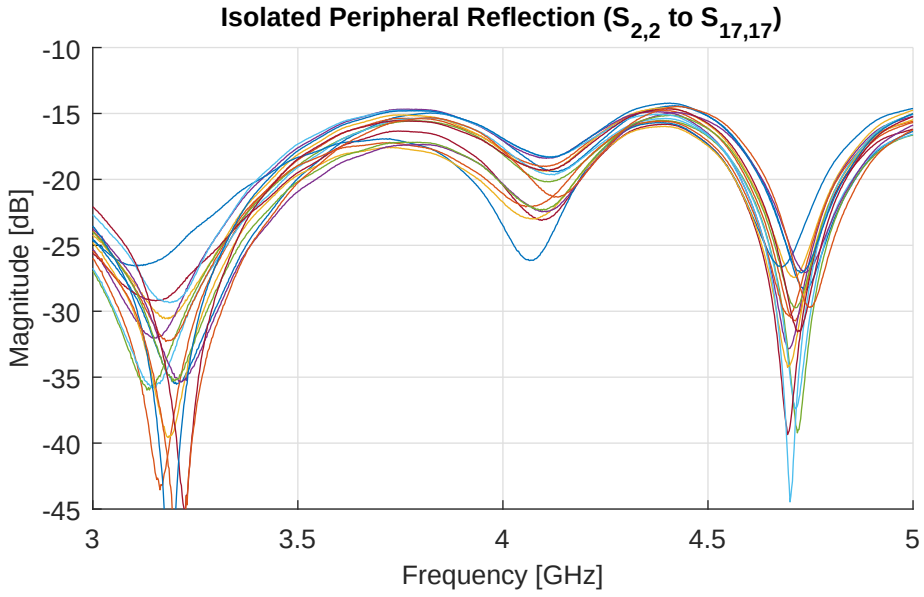

Figure 4.23: Reflection measured at each of the peripheral ports on the isolated combiner.

The results of the peripheral signal balances are also as expected. Figure 4.24 show that sufficiently good symmetry is achieved with the amplitude and phase balances at the peripheral ports. Amplitude balance is shown to be within ± 0.2 dB over 40% relative bandwidth, and the phase balance is within $\pm 2^{\circ}$ over the same bandwidth. These balances are calculated using the average of each quantity as the reference.

Another acclaimed advantage of axially symmetric combiners is their low losses for higher numbers of combined ports. While the focus of this design was not on minimizing losses, the results obtained are still notable and included for comprehensiveness. Figure 4.25 shows a loss of maximum 1 dB is observed over a 1 GHz bandwidth, 25% fractional bandwidth at the design frequency. This translates to a combining efficiency of 79% over that domain.

The loss in the radial line sections and incorporated hybrid quadrature couplers only pass the 0.5 dB threshold at 4.5 GHz, and reach a maximum of just 0.65 dB at 5 GHz. The external coaxial cables and off-the-shelf hybrid quadrature coupler were chosen for convenience. Figure 4.26 show that the coaxial cables contribute a significant amount of the energy lost. Nonetheless, the total loss throughout the combiner is still acceptably low.

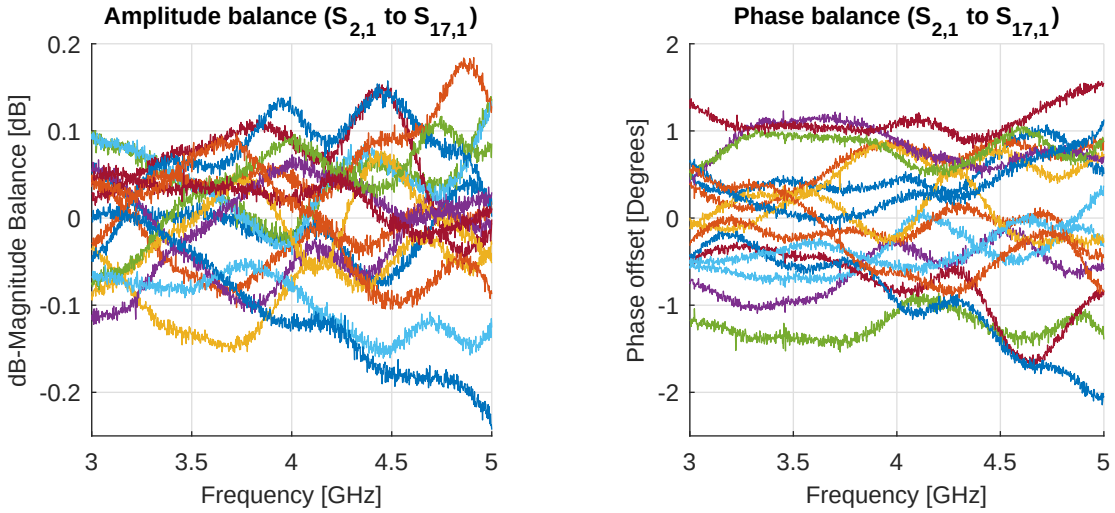

Figure 4.24: (a) The magnitude in balance in dB and (b) the phase balance measured at the peripheral ports of the prototype isolated radial combiner.

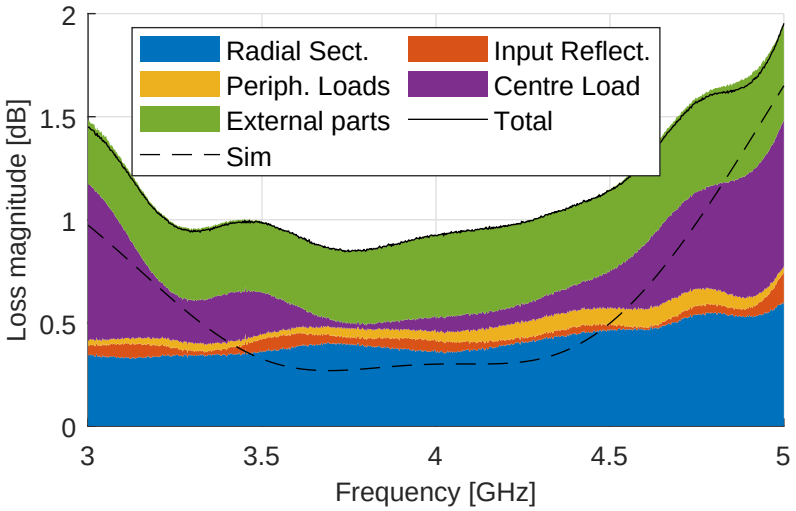

Figure 4.25: Various losses throughout the combiner

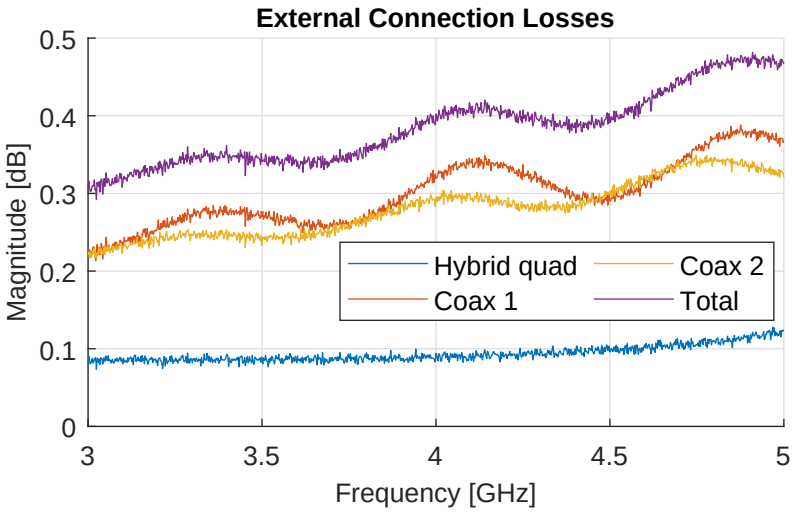

Figure 4.26: Losses in the external components of the isolation network.

Chapter 5

Graceful Degradation

The isolation network developed in Chapter 4 will be further analysed in terms of the graceful degradation achieved. Graceful degradation, as mentioned in Chapter 2, is the characteristic of a system to degrade in performance as the frequency or severity of a fault condition increases. The counterpart is catastrophic failure. In the latter case, the entire system must either be shut down or suffers critical damage due to a relatively small fault. Graceful degradation is therefore a desirable quality in microwave power combination.

Graceful degradation will be analysed based on the magnitude and phase of the power at various points in a typical divider-amplification-combiner arrangement. The points at which power will be analysed are at individual amplifier inputs and outputs, and the total power combined at the system output. The magnitude of degraded output power, relative to the nominal power, from a lossless N-way power combiner can be calculated as [54]

$$\frac{P_o}{P_n} = \left[1 - \frac{k}{N}\left(1 - \sqrt{P_f}\right)\right]^2, \tag{5.1}$$

where P_o is the output power magnitude with some faulty input(s), P_n the nominal output power magnitude when all inputs are functional, k number of failed inputs, and P_f the power magnitude from a faulty input. This is valid when the inputs all fail in the same way, as would be the case for analysis in this work. A detailed simulation analysis will be done to highlight important benefits of the isolation network.

5.1 Simulation Approach

The set-up used for testing the graceful degradation is shown in Figure 5.1. Each link is a parametrised circuit model that implements the required termination. The simulations will test two combinations of the isolated and non-isolated N-way combiners/dividers. The first combination consists of non-isolated units, and the second is a set of isolated combiners.

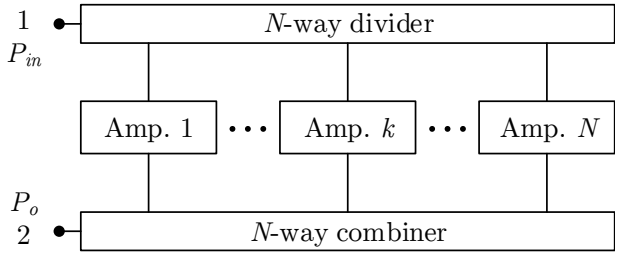

Figure 5.1: Schematic of the set-up used to test various graceful degradation scenarios.

These simulations are based on the final CST models of the power combiners created in Chapters 3 and 4. The isolated combiner model from CST is augmented at the combining port with ideal models of a quadrature coupler and transmission lines from the main unit to this coupler.

A benchmark for each setup will be set using 16 ideal amplifiers of equal gain $G_{dB} = 10\log_{10}(16) \approx 12$ dB, and perfect reverse isolation. Thereafter the degradation will be tested by replacing some amplifiers with (1) a reciprocal 0-dB through connection, (2) an open circuit or (3) a short circuit to ground. A series of tests will be run where the number of simultaneous fault conditions is incremented.

Various arrangements of amplifier conditions will be evaluated at the combiner ports, with up to 8 faulty amplifiers in each arrangement. As will be shown, the improvement in degradation performance can be presented using the chosen subset of arrangements. The faulty amplifiers are (1) all neighbouring elements, (2) at every second position, and (3) spread as symmetrically as possible around the periphery.

With reference to Figure 4.1, the strongest coupling among peripheral ports in the non-isolated prototype exist between any port and its neighbouring ports. When all faulty amplifiers are neighbouring elements, it exposes as few as possible working amplifiers to faulty neighbours. In contrast, the other two arrangements put the maximum number of faulty amplifiers as neighbours to functional amplifiers.

5.2 Degraded Output – Centre Frequency

The first aspect analysed is the overall power degradation at the output of the system, designated as P_o in Figure 5.1, at 4 GHz. The benefit of isolated power combiners over their non-isolated counterparts is illustrated in Figure 5.2. The degradation levels in Figure 5.2 are normalised to the output power of the respective combiner setups when all the amplifiers are operational. The top two cases show how the isolation network mostly restrains the degradation from dropping below the power predicted by (5.1).

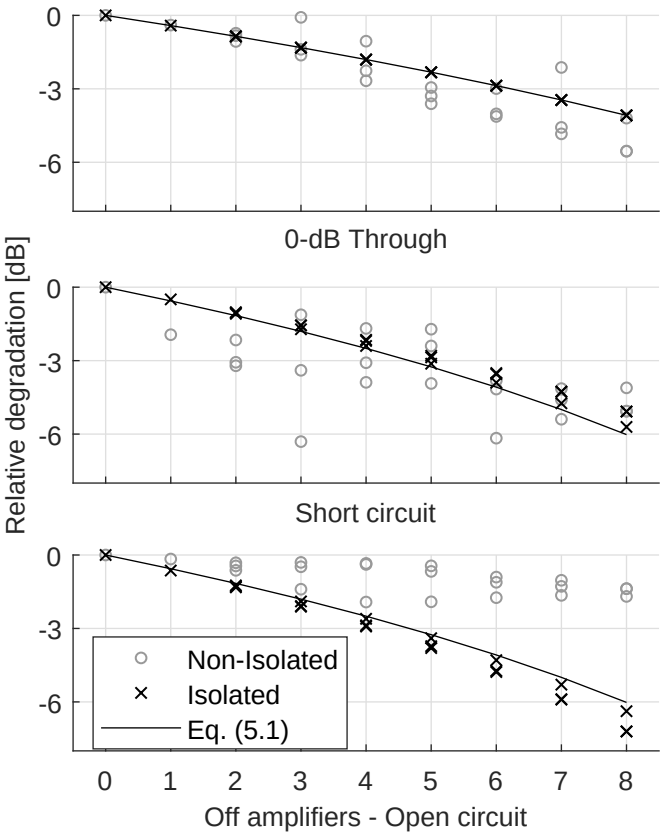

Figure 5.2: Degradation performance with faulty amplifiers implemented as 0 dB through connections, open circuits and short circuits to ground.

The bottom plot in Figure 5.2 highlights another important advantage of the isolation network. The output power of the non-isolated combiner setup is higher than the best case degradation presented by (5.1). This indicates that some of the remaining functional amplifiers are delivering significantly more power into the system than normal. In the next section, where a broadband analysis of the system is done, the possible cause of this unexpectedly high power output is considered.

5.3 Degraded Output – Broadband

In this section, broadband degradation characteristics will be analysed with respect to faults arranged symmetrically around the combiner setup. Plots of the performance for the remaining cases are presented in Appendix A. The degraded performance is similarly improved for all three faults arrangements considered.

The contrast between the erratic failure of the non-isolated combiner setup

and the graceful degradation of the isolated combiner setup is clear from Figure 5.3. Figure 5.3(a) shows spurious resonances that occur in the structure.

For the 0-dB through faults (top panel in Figure 5.3(a)), the effects are particularly interesting. The amplifiers drive power back into the dividing stage through faulty ports. These signals are then amplified again causing oscillation peaks at around 3.25 GHz and 4.2 GHz. The high peaks are due to the ideal amplifiers used, so there is no physical upper limit to the power available at each amplifier. Real amplifiers would have been damaged or destroyed in this scenario. Open and short circuit faults, shown in the bottom and middle panels, cause reflections of all the input power at similar frequencies. The output is then severely attenuated at these frequency points

The analysis in Figure 5.3(b) of the isolated setup shows no such anomalies. Both input reflection, and the output degrades gracefully in proportion to the amount of failed amplifiers across the entire spectrum of interest. The high values (above -10 dB) of input reflection seen are as expected, considering that a significant amount of energy is reflected symmetrically at the short and open circuit faults. Due to the reciprocity of the radial combiners in the system, these reflected modes appear at the input port.

Vast improvements in the phase changes resulting from failed amplifiers are demonstrated in Figure 5.4, where the plots are relative to the output phase of a fully operational setup. The seemingly better power magnitude output from the non-isolated setup appearing in the bottom panel of Figure 5.2 is shown to have a completely altered phase (bottom panel of Figure 5.4) in comparison to nominal operation. This means that, although more power reaches the output, the signal integrity is severely compromised. On the other hand, Figure 5.4 shows the consistency of the output phase degradation of the isolated combiner setup. Except for one case, the isolation network keeps the output phase changes within $\pm 10^{\circ}$ over all types of failures analysed.

The simulations of this section are also repeated using S-parameters of a typical commercial off-the-shelf amplifier module. The results are very similar to what was shown here using the ideal amplifiers. Nonetheless, the amplifier S-parameters and simulation results are included under Appendix A in Figures A.5 to A.11.

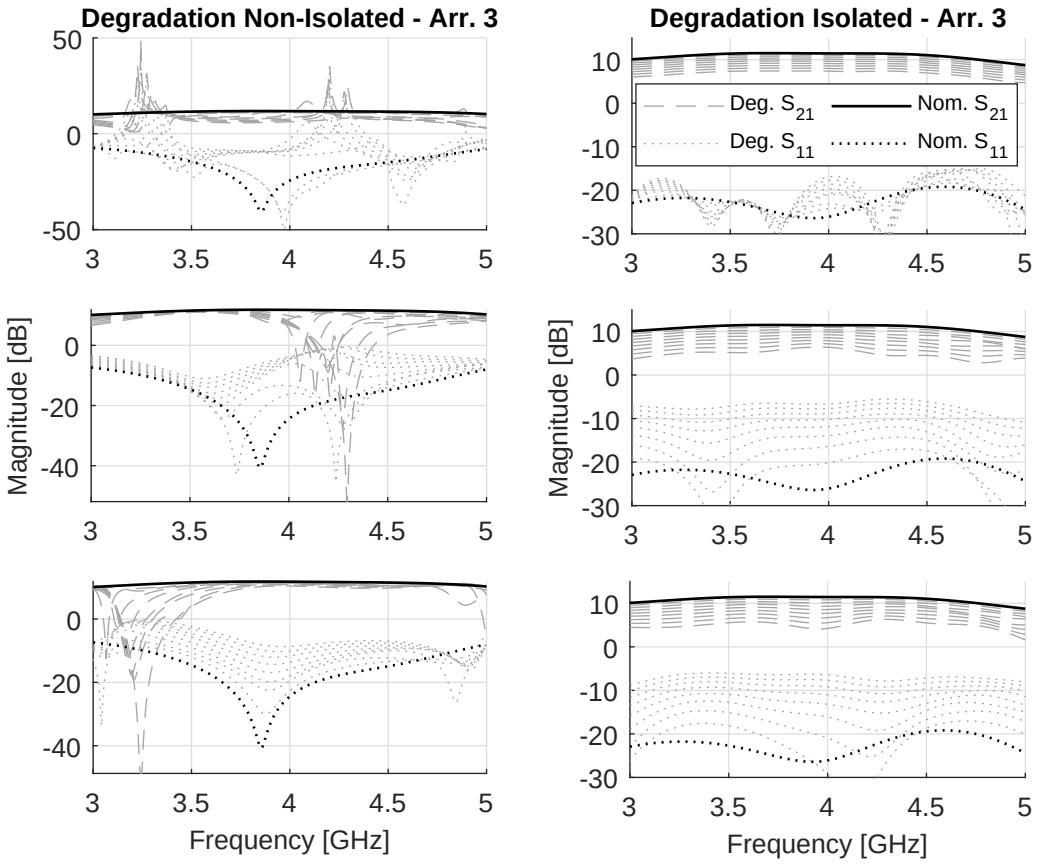

(a) (b)

Figure 5.3: Broadband output magnitude degradation performance of the (a) non-isolated and (b) isolated combiner setups for faults spaced as symmetrically as possible. From top to bottom: 0-dB through, short and open circuit faults.

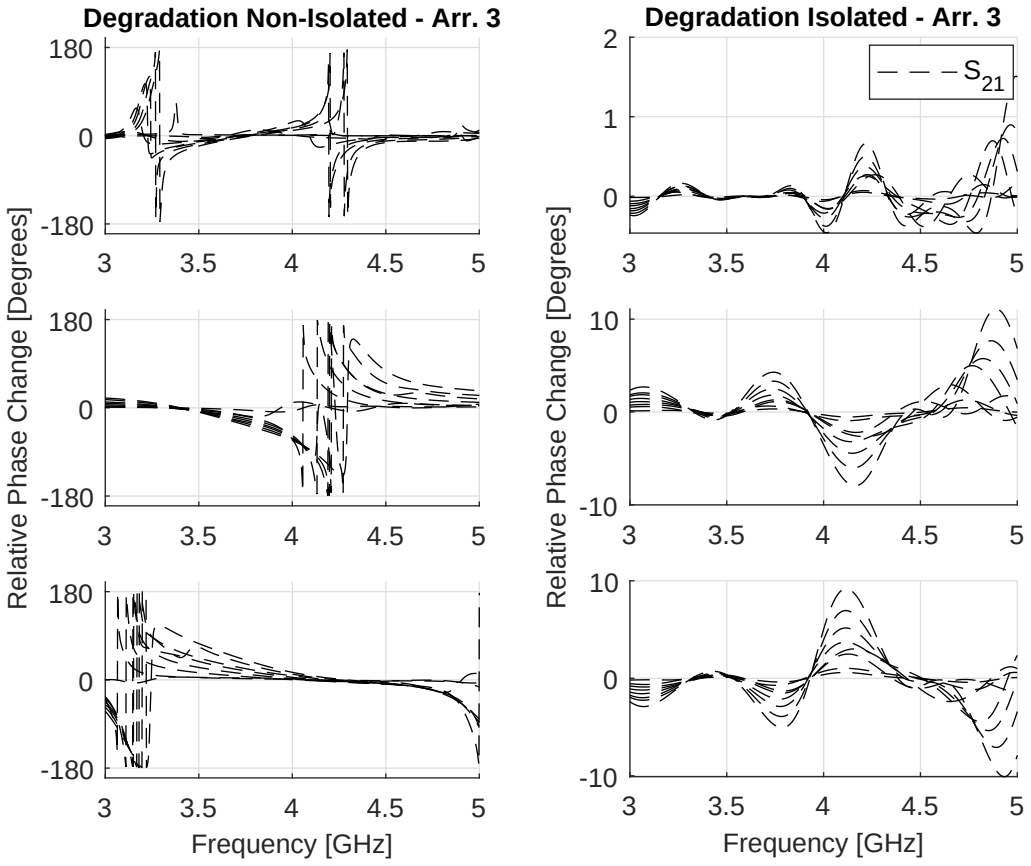

(a) (b)

Figure 5.4: Broadband output phase degradation performance of the (a) non-isolated and (b) isolated combiner setups for faults spaced as symmetrically as possible. From top to bottom: 0-dB through, short and open circuit faults.

5.4 Individual Node Power Levels

Further insight is gained by considering the power at the nodes that link each divider and combiner. This analysis is again done only at 4 GHz. Figure 5.5(a) shows the power balance at the input of the respective nodes, also the output (peripheral) ports of the divider. The three plots per number of failed amplifiers represent, from left to right, the arrangements 1 to 3 as explained in Section 5.1. The errorbars indicate the minimum and maximum power recorded, and the median values are marked by the $\times$ and $\bullet$ markers. These values are normalised to the maximum power delivered to a peripheral port for the system without any amplifier faults. Relative power levels at failed ports are also removed from the results. These analyses should not be interpreted as indicative of the power handling capacity of the structure, but as the relative distribution of power within the structure while in operation.

With an isolation network, the signal balance of the radial combiner is much better preserved in the presence of fault conditions at amplifier locations. For some cases the non-isolated divider exhibits port imbalances of more than 6 dB, whereas the isolated divider mostly maintains a peripheral port imbalance well below 0.5 dB. Only multiple open circuit faults cause the peripheral port balance of the isolated divider to exceed a 1 dB difference.

Simulation results of the power at the outputs of the amplifier nodes, connected to the peripheral input ports of the combiner, are presented in Figure 5.5(b). Given that the amplifiers have perfect reverse isolation, it is expected that the power balance at their outputs should resemble that at their inputs, only uniformly scaled by the amplifier gain. However, interaction inside the non-isolated combiner results in altered power levels present at these points. This effect is observed more prominently for the open and short circuit type faults.

For the isolated combiner however, the power balances at the amplifier outputs are much more consistent with those at the amplifier inputs. This adds to the argument that the isolation network adds significant capability to axially symmetric combiners in terms of peripheral signal balance under fault conditions.

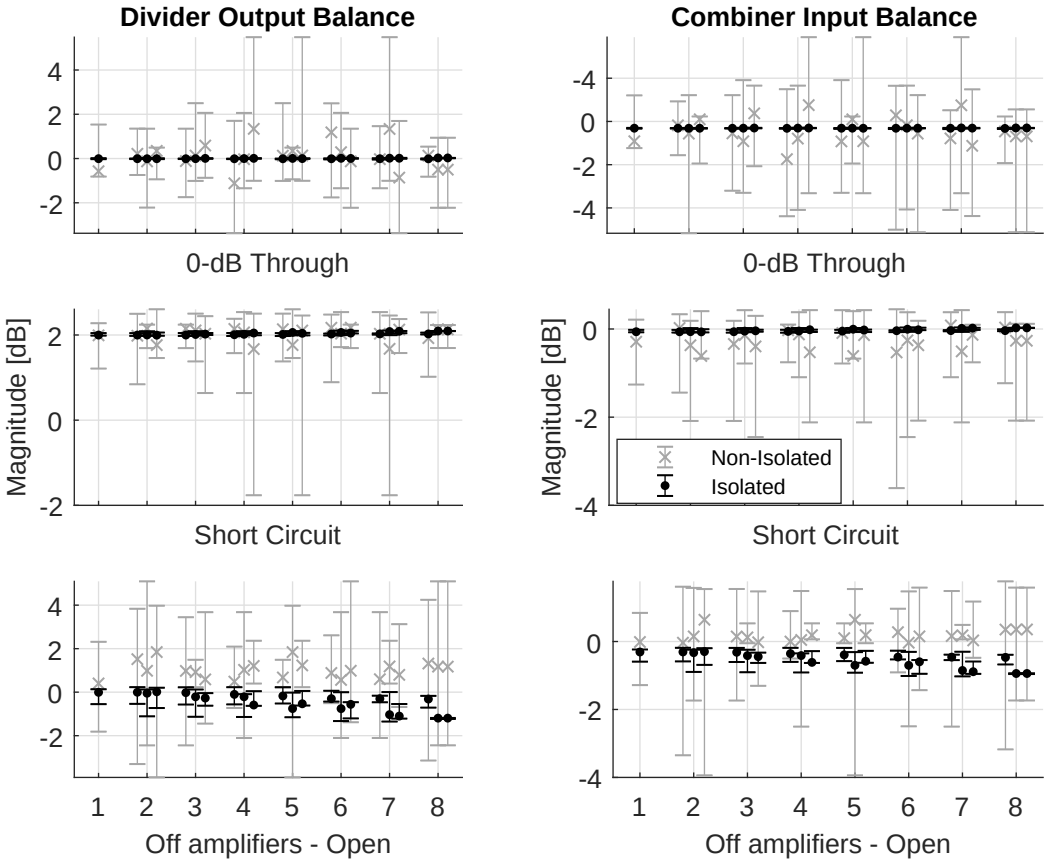

(a) (b)

Figure 5.5: Power magnitude balance at (a) divider and (b) combiner peripheral ports for various fault conditions, relative to the nominal power expected at a peripheral port. The errorbars show the minimum and maximum per fault case, and the markers indicate the median values for each arrangement per number of faulty amplifiers.

5.5 Isolation Load Power Levels

It is also important to consider the power levels dissipated in the termination loads of the isolated combiner. Results of these simulations are shown in Figure 5.6. The errorbars again show the balance, with $\times$ markers at the median values, of power at the peripheral loads. The $\circ$ markers show the power in the load connected to the combining port quadrature coupler. Again, the power levels shown, for both the divider and combiner, are relative to the input power denoted by P_{in} in Figure 5.1.

This analysis highlights how the power is spread among the loads for this work. At no point in Figure 5.6 does the power in a single load exceed the input power. Even for the case of 30 dB gain per amplifier, shown in Figure A.12,

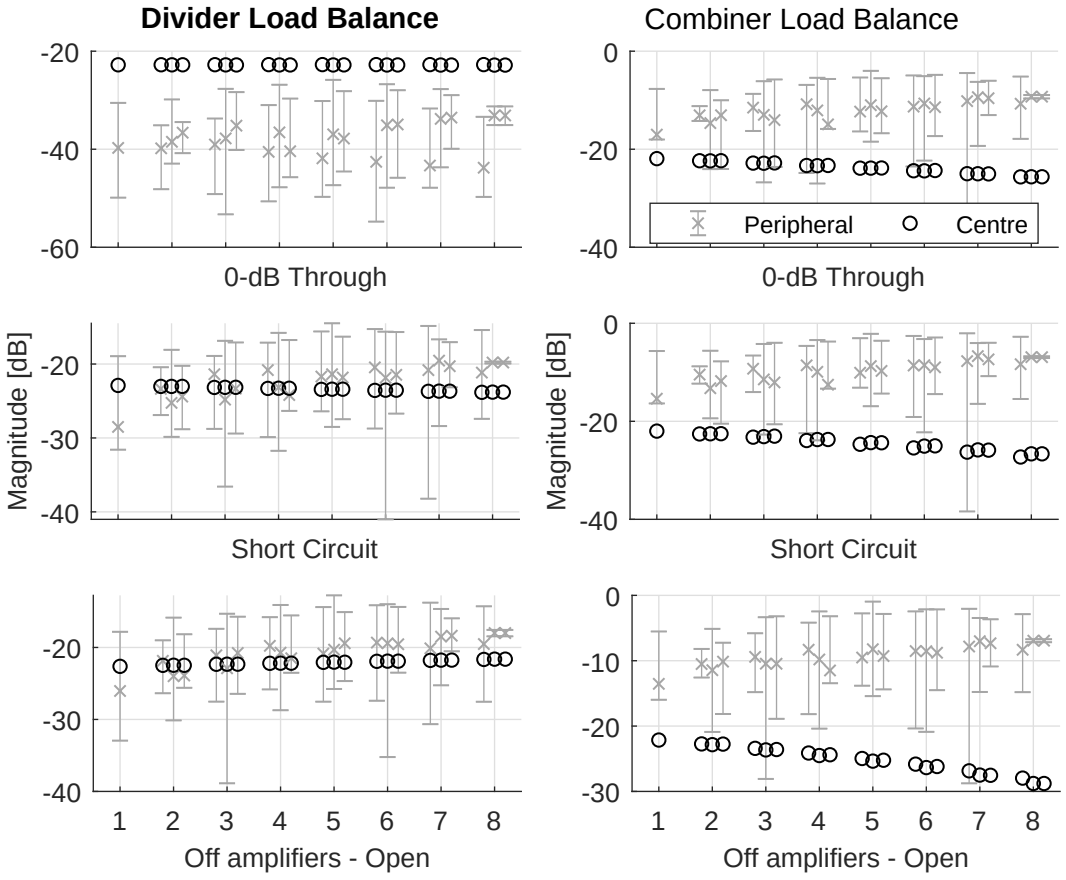

(a) (b)

Figure 5.6: Power dissipated in the isolation loads of the (a) divider and (b) combiner, relative to the input power. The errorbars show the minimum and maximum per fault case, and the markers indicate the median values for each arrangement per number of faulty amplifiers.

the power dissipation per load is still reasonable. In the latter, any single load dissipates at most 10 dB less than the power output from an amplifier.

Another advantage of the isolation network is clear from the total power dissipated in all the peripheral loads. Figure 5.7 shows the cumulative power dissipated in all the peripheral isolation loads for 12-dB amplifiers. For a small number of faults ($k < 5$) the divider loads dissipate up to -7 dB of the input power. The combiner dissipates at least half the input power in loads for just a single fault, and this rapidly increases to more than the input power for more failed amplifiers. This situation is considerably more serious for higher gain amplifiers. As shown in Figure A.13, the least amount of power that would need to be dissipated for a single fault is more than 15 dB higher than the input power.

Other passive isolation methods used in conjunction with axially symmetric

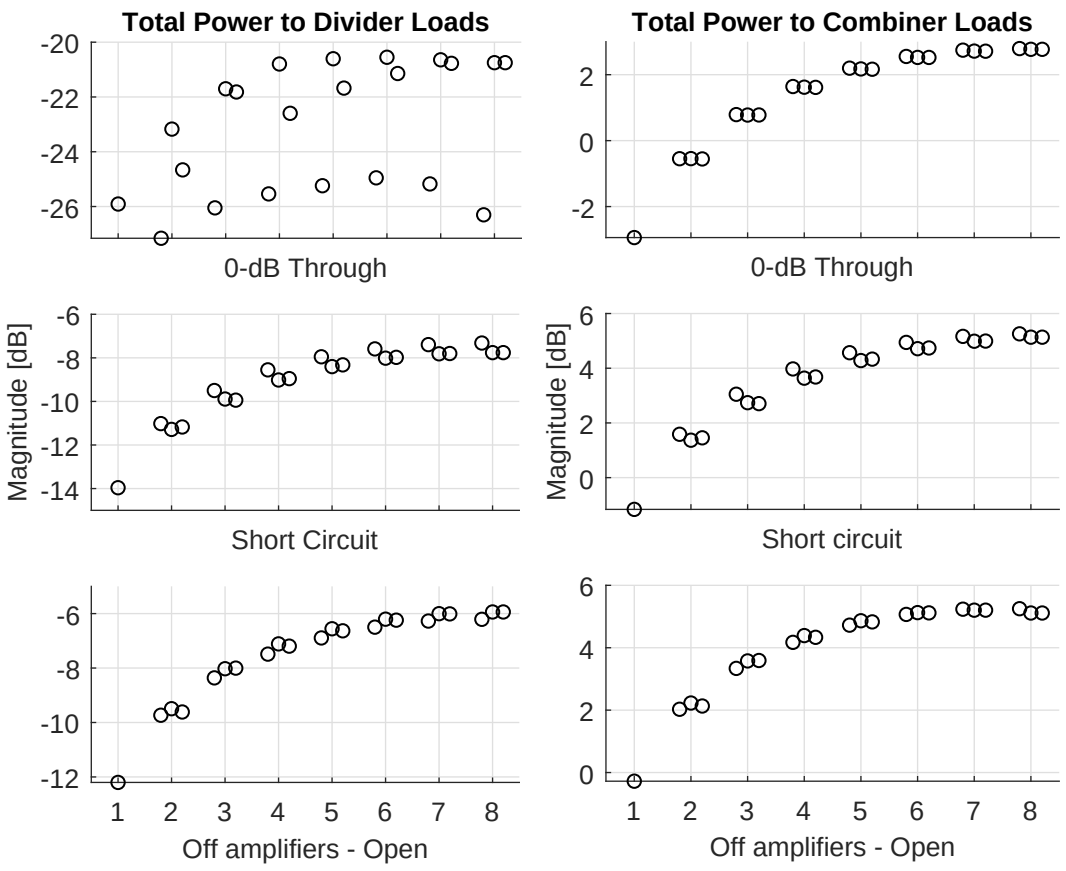

(a) (b)

Figure 5.7: Total power dissipated in all the peripheral isolation loads of the (a) divider and (b) combiner, relative to the input power. Different arrangements are plotted per number of faulty amplifiers

combiners dissipate all this power inside the structure, should a fault occur. Moreover, this is commonly close to the combining port, where the highest field strengths (and heat at high power) already exist. For high power applications, this is especially concerning. However, using the passive isolation network as developed in this work, that power is dissipated in loads that are dispersed relatively well, and can be moved and/or cooled further away from the main structure.

Chapter 6

Conclusion

As seen in Chapter 1, power combiners play a significant role in modern radio frequency engineering applications. In that overview, axially symmetric combiners appear to have uniquely practical significances. Three prominent advantages of these are their closely balanced divided signals, moderate to wide bandwidths, and relatively low insertion losses.

6.1 Overview of Work Done

Conical and coaxial power combiners have input reflection levels below -15 dB recorded over more than 70% bandwidth, but are relatively complex to manufacture. Prototypes have to be manufactured using CNC machining with extremely tight tolerances, which often escalates manufacturing cost and time.

Radial combiners, however, show performance near these. Input reflection bandwidths at -15 dB are significantly narrower, but still wider than 20% for many designs. Signal balances at the peripheral ports are close at approximately ± 0.1 dB amplitude balance and $\pm 1^{\circ}$ phase balance for the various designs reviewed. The advantage that radial combiners pose above coaxial and conical ones, is the possibility of simpler manufacturing techniques.

Some radial combiner designs were therefore explored in more detail in Chapter 2. Specific attention was given to the types of centre port and peripheral port transitions. The more complex radial combiners relied on machining some modified inner conductor for a coaxial line that feeds into the centre of the radial combiner.

With the aim to keep manufacturing relatively simple, the centre transition was chosen to avoid machining a coaxial inner conductor. Simpler designs made use of planar PCB technology to create the transition. This approach was taken for the designs in Chapters 3 and 4.

The decision of adding an air layer to match the characteristic impedance at the centre largely steered the choice of the peripheral port design. A hybrid of inductive posts and microstrip lines are used to couple energy through the

combiner periphery. This allowed the addition of a planar isolation network at the peripheral ports.

Until now, axially symmetric combiners lacked significantly with regard to isolation among the peripheral ports. Unwanted peripheral coupling in the non-isolated radial combiner in this work was as much -10 dB. This means that, for any asymmetric input signals, it is possible that more energy is coupled to another input port than the ideal -12 dB coupled to the combining port. A passive isolation network is therefore implemented and tested on a radial power combiner.

The passive isolation network was chosen due to the performance illustrated in [22], where the largest coupling among input ports was still below -20 dB in the bandwidth of interest. The version in [22] was adapted for implementation around the back-to-back radial combiners. The radial sections were modified and augmented to feature the isolation network, and another prototype was built.

Prototype testing of both designs yielded satisfactory results. The design specifications set out at the start of Chapter 3 were achieved. Both combiners show centre port reflection of less than -15 dB over at least 800 MHz (20% fractional bandwidth). The isolated radial combiner has average peripheral port isolation larger than 27 dB over the 40% bandwidth from 3 to 4.6 GHz. This is a significant improvement from the general performance of axially symmetric combiners.

The resultant improvement in degradation is also evident, as explored in Chapter 5. The midband output magnitude degrade close to that predicted from theory, and peripheral balances are kept below 0.5 dB difference in the event of failing amplifiers. In wideband analyses, the phase difference between a nominal system and a degraded one is less than 10° over the 50% bandwidth analysed. Attention is therefore turned to comparing the results obtained herein with that of similar devices described in literature.

6.2 Comparison of Results with Literature

Comparing favourably to the -15 dB reflection bandwidths of 15% [31] and 19.4% [32], the current design shows a maximum of -15 dB reflection for at least 20% fractional bandwidth. Taking the -10 dB reflection bandwidth, it displays an improvement from 29.5% in [13] to over 37.5%.

The phase and amplitude balance at the peripheral ports did, however, not supersede performance shown in literature. With an amplitude balance of ± 0.1 dB and phase balance of $\pm 1°$, the purely PCB based design in [13] boasts a better peripheral signal balance. The first design presented in this work managed results close to that, namely ± 0.3 dB amplitude and $\pm 2.5°$ phase balances. Likely causes are misaligned peripheral posts, as these are the most notable peripheral elements not present in [13]. The design frequency should

also be taken into consideration. With this work spanning 3 - 5 GHz, it is more sensitive to geometric asymmetries than [13] at 1.5 - 3 GHz.

Table 6.1 presents a comprehensive summary of how the new isolated combiner compares to notable designs in current literature. The media in the combining cavities compared include air, printed circuit board, and partially filled (PF) cavities. The performance metrics considered are the design centre frequency (f_c), fractional bandwidth (BW), center port reflected loss (RL), combining insertion loss (IL), signal balances, peripheral port reflected loss (RL^P) and, most significantly, the isolation. Naturally isolated combiners are designs that do not include any dedicated peripheral port isolation components.

Ref.	Combiner		f_c	BW	RL	IL	Balance ±		RL^P	Min.	Isolation
	N	Med.	(GHz)	(%)	(dB)	(dB)	(dB)	(°)	(dB)	(dB)	Type
[14]	30	PCB	12.5	24	12	0.9	0.5	5	–	16	Resistors
[18]	10	Air	10	74	15	1.1	1	5	–	5	Natural
[24]	16	PF	4	20	15	0.5	0.3	2.5	5	10	Natural
[31]	7	PCB	20	45	10	2.4	–	7.5	–	8	Natural
[34]	8	Air	10	63	15	0.5	–	–	–	7	Natural
[36]	8	Air	14	25	19	–	0.5	–	–	7	Natural
[39]	19	Air	20	25	13	0.7	0.5	–	13	18	Resistive inserts
[40]	20	Air	34	25	10	1	0.5	6	15	12	Resistive inserts
This work	16	PF	4	25	18	1	0.2	2	15	27	Phase cancelling

Table 6.1: Brief comparison of current work with existing axially symmetric combiners.

The addition of the isolation network to the radial combiner improved the centre port input reflection. It is below -18 dB for over 40% relative bandwidth (the 25% shown in Table 6.1 is limited by the 1 dB insertion loss bandwidth). This is better reflection performance than many of the designs considered in Chapter 2. The combiners with significantly better input reflection are the more involved conical and coaxial type combiners [16], [18].

Looking at the amplitude and phase balances, improvement is seen from the non-isolated design. Most of the peripheral port signals of the isolated radial combiner fall within the ranges ±0.1 dB and ±1° of each other. In the 25% bandwidth, the outliers are still within a ±0.2 dB amplitude balance, and

a $\pm 2^{\circ}$ phase balance. This is closer to the performance of other designs in literature

The isolation performance of the isolated radial combiner is most notable. The improvement due to the isolation network over non-isolated combiners is obvious from Table 6.1. Even combiners that have dedicated isolation components trail the new design by approximately 10 dB. Also, since this isolation network dissipates unwanted energy outside the structure, unlike others in literature [39], [40], the degradation would likely not deteriorate in a high power implementation.

The current design, even with the relatively high losses, is well suited to combine signals from a receiving antenna array. At this point the power levels within limits and combiner loss is insignificant compared to the more than 20 dB gain from typical low noise amplifier (LNA) configurations between the antenna elements and the combiner. LNA's are known to occasionally fail in the field by, among others, going into a state of oscillation. Without isolation, such occurrences will completely disrupt the operation of the array. In the case that LNA outputs are combined in an isolated combiner, the effect of a failed LNA will largely be limited to only the failing channel. As such, the receiving beam pattern will experience very little disturbance. For moderate transmission power, the combiner can also be used as a splitter to an antenna array. Here, failure of an element will also disturb the transmission beam pattern to far lesser extent than having very little to no isolation among elements.

6.3 Future Work

It would be useful to estimate and test the power handling capability of an isolated combiner of this nature. Although the external coupler in the current prototype is rated to handle a maximum of 100 W average power, the main structure should be able to operate at a somewhat higher power. This is important information for engineers looking to implement such a design, and would need to be addressed in future work.

Moreover, the general combiner performance can be improved by opting for higher accuracy machining using CNC fabrication. From the prototype testing it is clear that the centre transition used in the design is inconveniently sensitive to pressure exerted on the substrate and misalignment. The air cavity, however, allows that the PCB based centre can be replaced with a CNC manufactured conical transition.

In that case, the PCB periphery can be kept through the peripheral posts. This configuration should combine the wideband transition of a conical transition with the flexibility of PCB at the periphery. For this case, the entire radial combiner housing can then be made by CNC, but it should suffice to only make the central transition in that way. Maintaining looser tolerances elsewhere in the combiner reduces manufacturing time and cost. Also, since

the highest concentration of power is at the centre of the device, a smooth, air-filled transition would be advantageous for high power applications. Should the application favour higher peak power, instead of average power, the transition can be filled with a suitable dielectric in the place of air.

Looking at significantly more complex solutions, a non-planar integrated quadrature coupler between the centres of the radial sections will eliminate the need for the external coupler and transmission lines. This should bring a noticeable reduction of insertion loss at the combining port. A crude version of a possible coupler for this purpose is shown in Figure 6.1. The coupler consists of a mixture of parallel coaxial and radial transmission line sections to implement the classic 3-dB quarter-wavelength branchline coupler in an axially symmetric topology.

A simulation of this model yielded promising results. Without any optimisation, the coupler at midband has an output signal balance close to ± 0.7 dB, with a 89.7° phase difference. The isolated port gets less than -30 dB and the input reflection is below -20 dB.

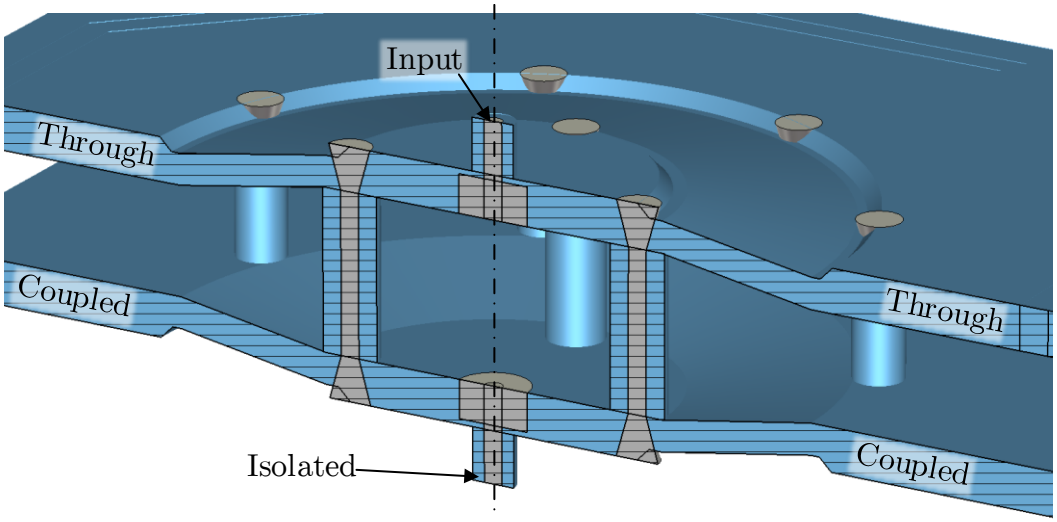

Figure 6.1: 3D model of a prospective coaxial quadrature coupler.

It should also be possible to implement the whole isolated combiner in waveguide structures. Riblet couplers would make an excellent, albeit highly involved, isolation network based on rectangular waveguides. Flipping the layout such that the centre ports of the underlying combiners face toward each other, the isolation network can be implemented between the combining structures. Having the combining port coupler so close to the combiner outputs will also eliminate insertion loss contributed by the dissipation in, and length difference of, the external transmission lines.

An optimal future design, however, would be the combination of an efficient integrated centre coupler and waveguide-based peripheral ports. This should

produce an elegant in-line, high power, fully isolated, passive power combining solution.

Appendix A

Supplementary Graceful Degradation Plots

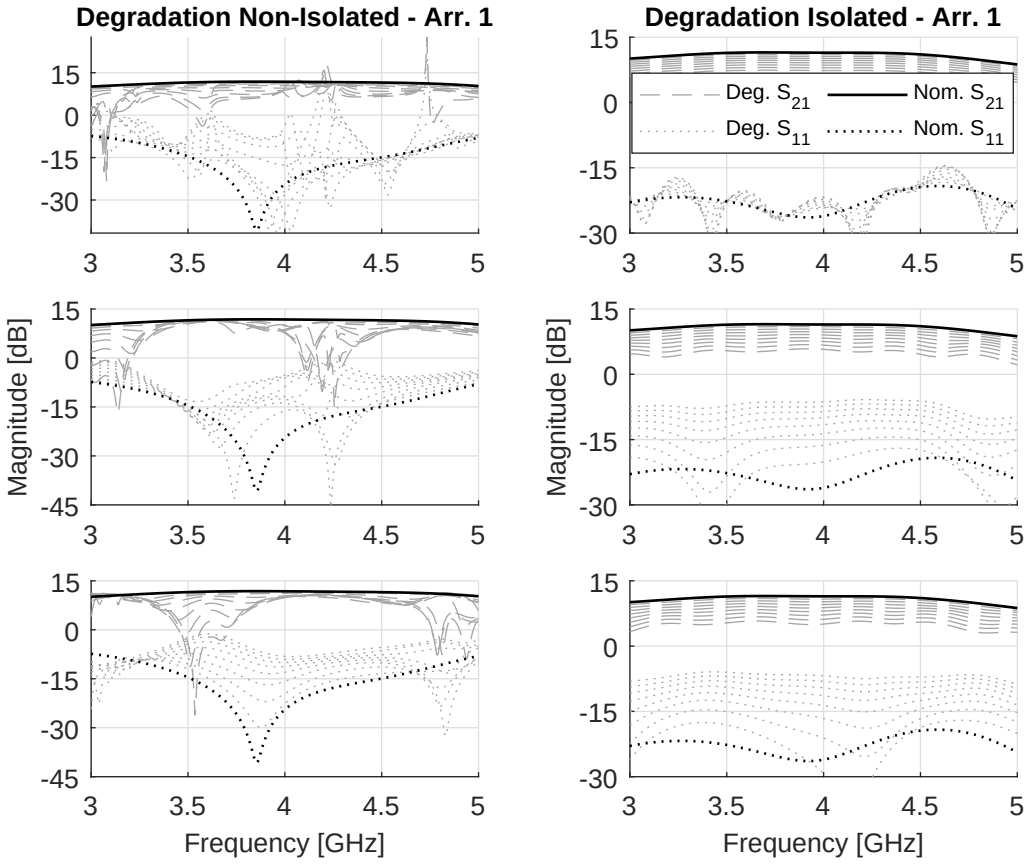

Figure A.1: Broadband output magnitude degradation performance of the (a) non-isolated and (b) isolated combiner setups for faults at neighbouring ports. From top to bottom: 0-dB through, short and open circuit faults.

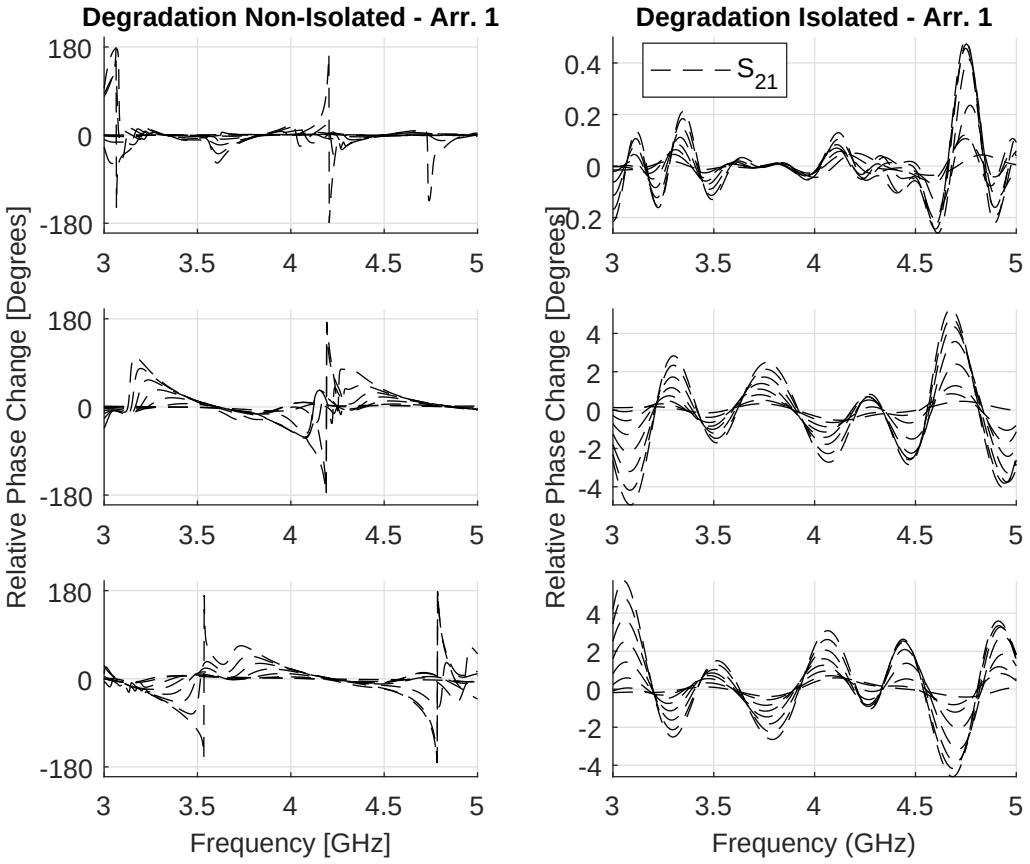

(a) (b)

Figure A.2: Broadband output phase degradation performance of the (a) non-isolated and (b) isolated combiner setups for faults at neighbouring ports. From top to bottom: 0-dB through, short and open circuit faults.

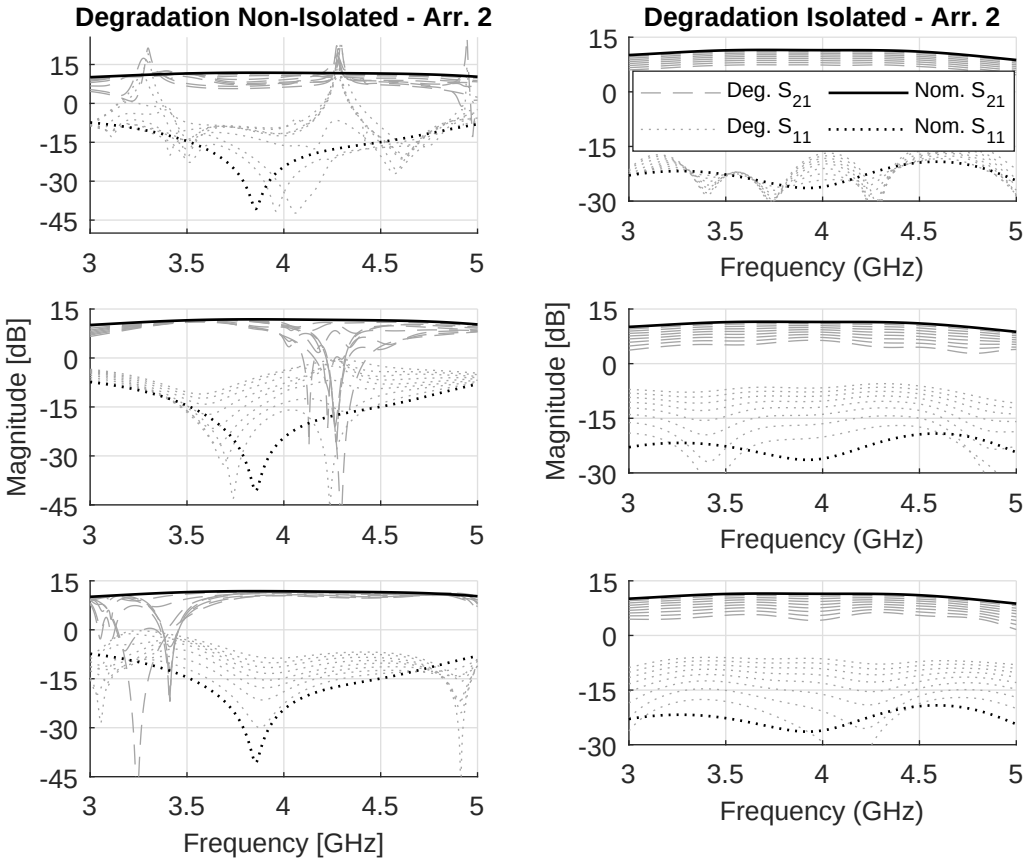

(a) (b)

Figure A.3: Broadband output magnitude degradation performance of the (a) non-isolated and (b) isolated combiner setups for faults at every second port. From top to bottom: 0-dB through, short and open circuit faults.

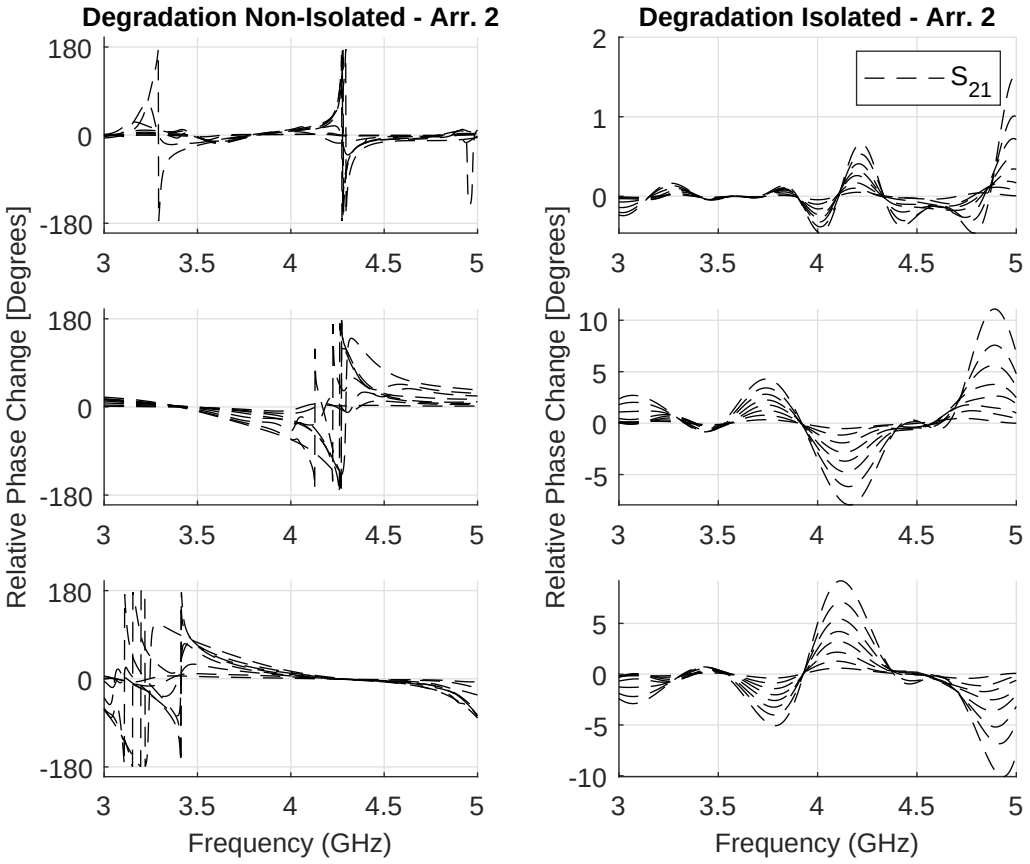

(a) (b)

Figure A.4: Broadband output phase degradation performance of the (a) non-isolated and (b) isolated combiner setups for faults at every second port. From top to bottom: 0-dB through, short and open circuit faults.

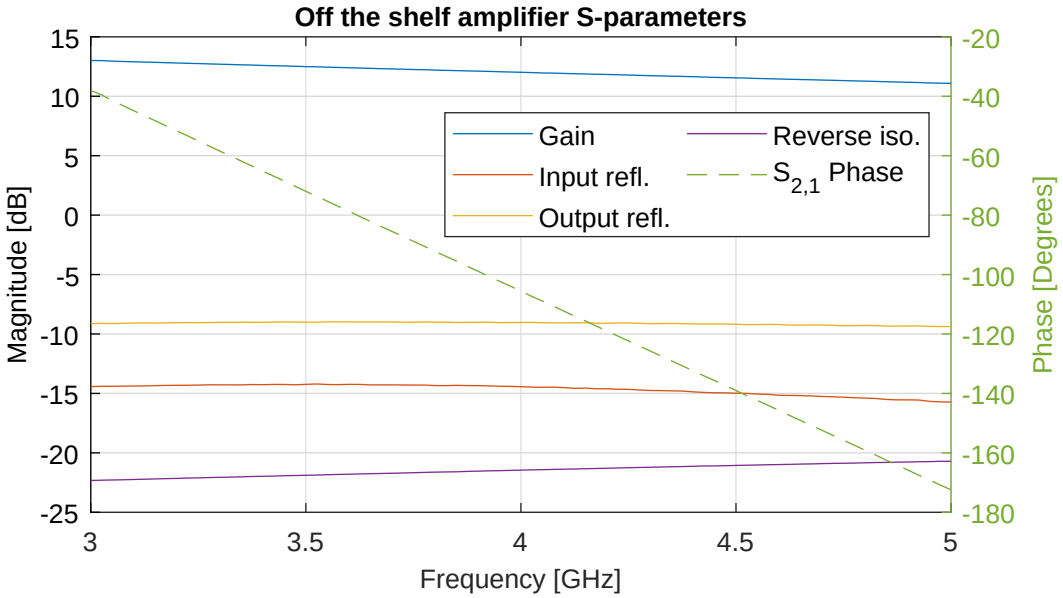

Figure A.5: S-Parameters of the commercial amplifier model used in select simulations.

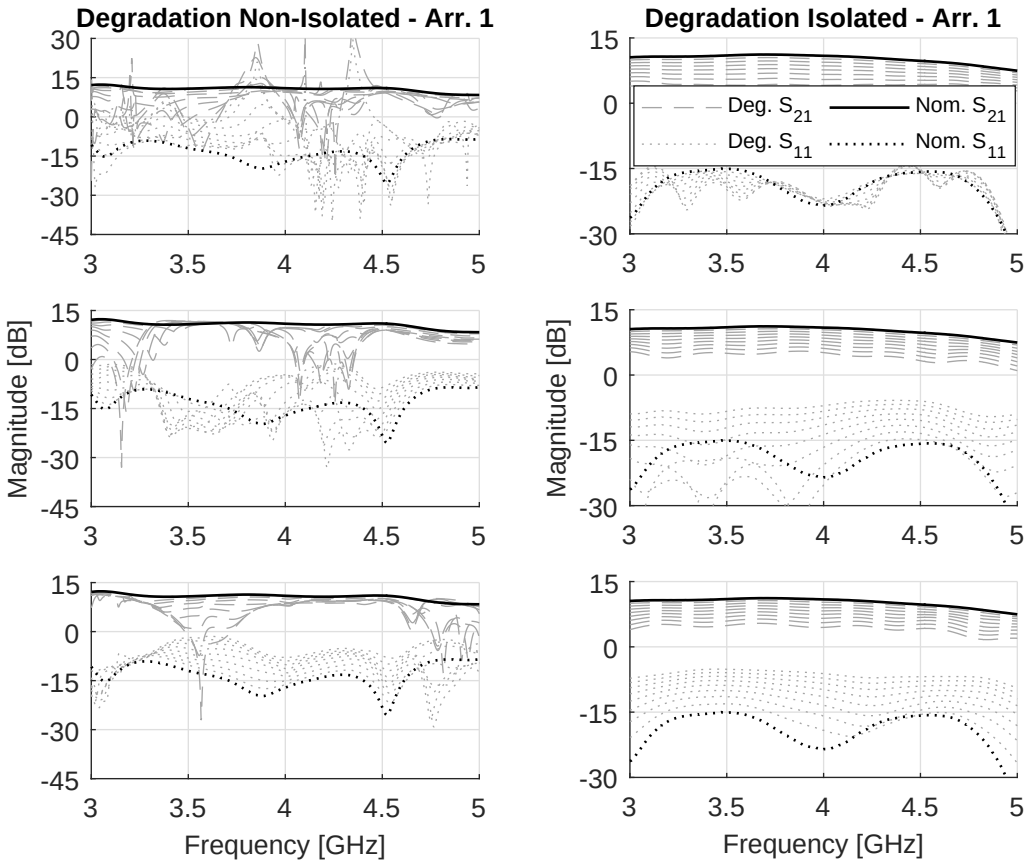

(a) (b)

Figure A.6: Broadband output magnitude degradation performance of the (a) non-isolated and (b) isolated combiner setups, using real amplifier S-parameters, for faults at neighbouring ports. From top to bottom: 0-dB through, short and open circuit faults.

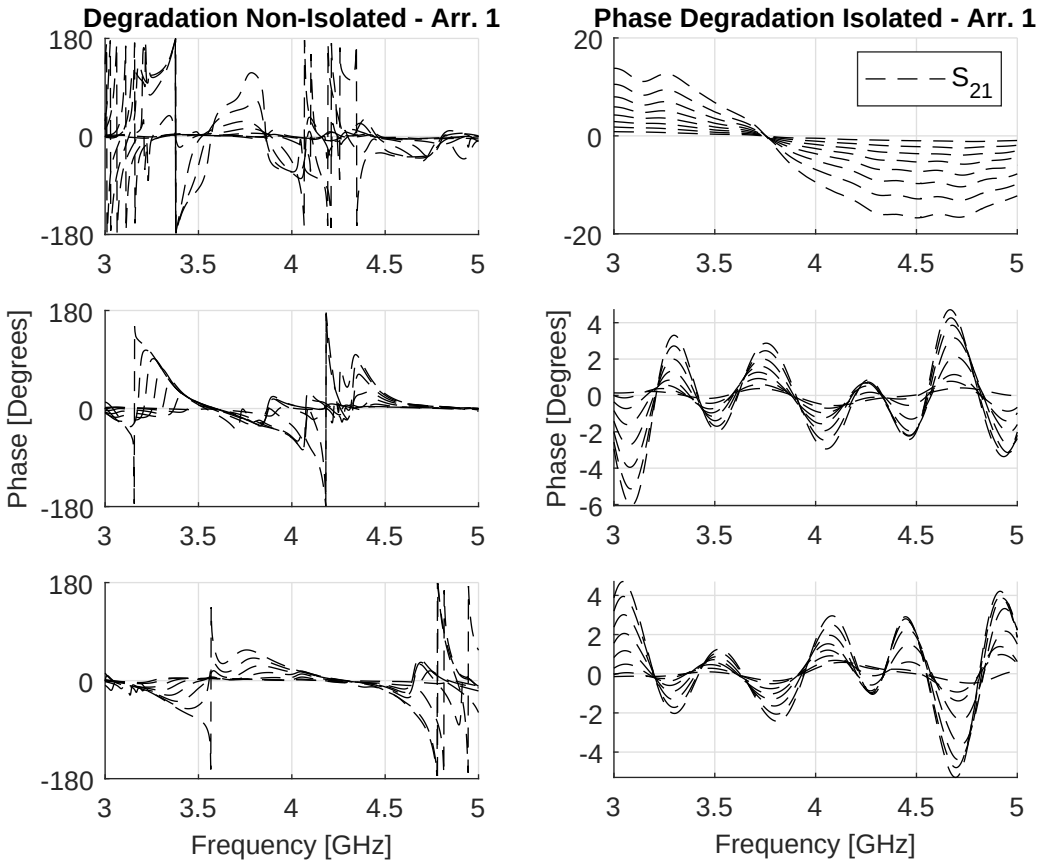

(a) (b)

Figure A.7: Broadband output phase degradation performance of the (a) non-isolated and (b) isolated combiner setups, using real amplifier S-parameters, for faults at neighbouring ports. From top to bottom: 0-dB through, short and open circuit faults.

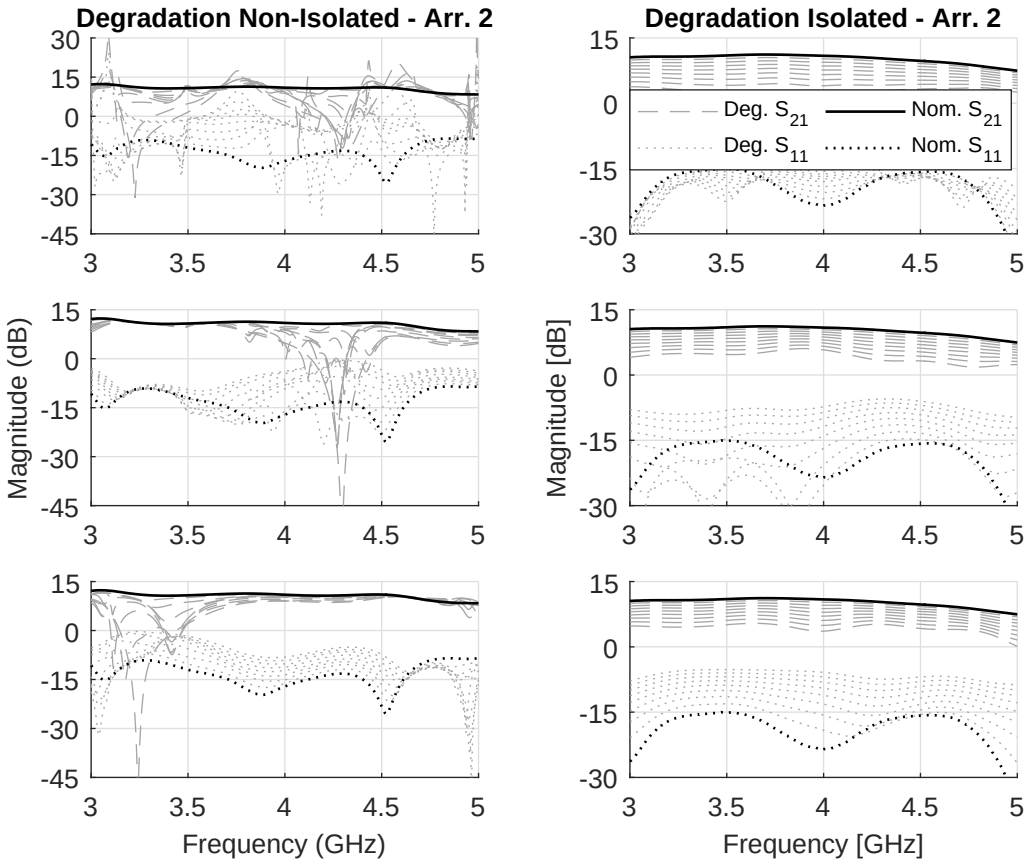

(a) (b)

Figure A.8: Broadband output magnitude degradation performance of the (a) non-isolated and (b) isolated combiner setups, using real amplifier S-parameters, for faults at every second port. From top to bottom: 0-dB through, short and open circuit faults.

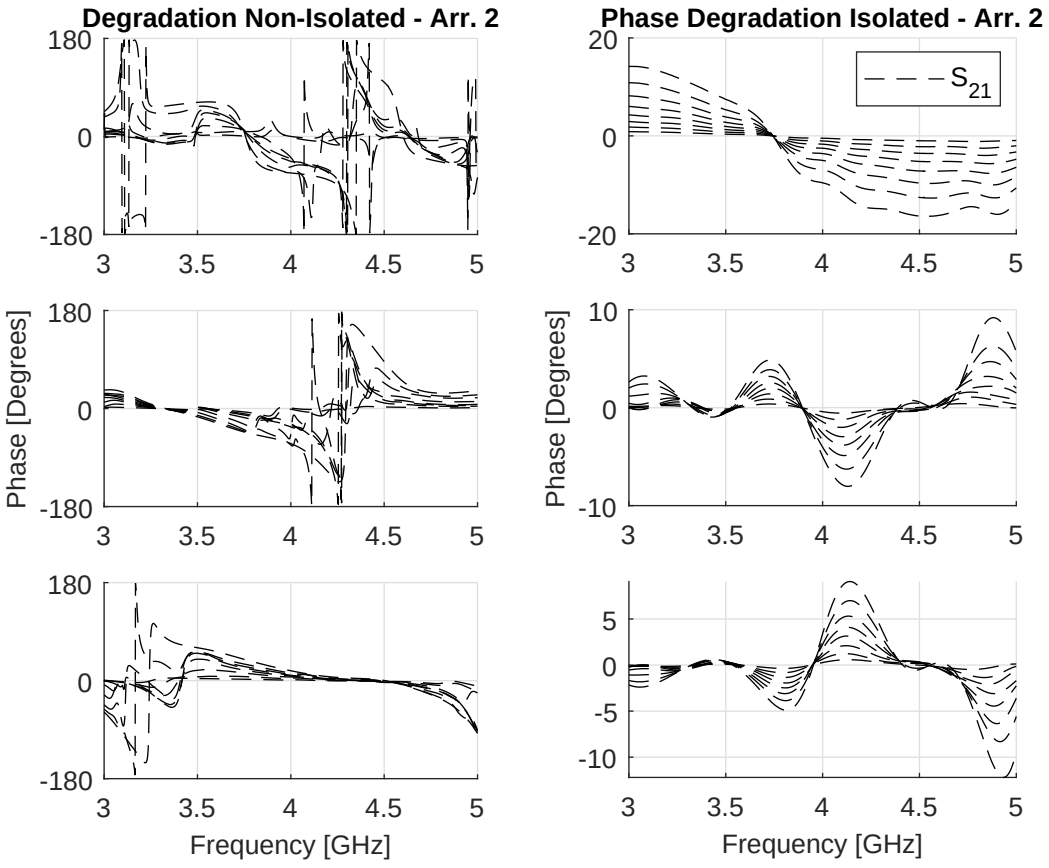

(a) (b)

Figure A.9: Broadband output phase degradation performance of the (a) non-isolated and (b) isolated combiner setups, using real amplifier S-parameters, for faults at every second port. From top to bottom: 0-dB through, short and open circuit faults.

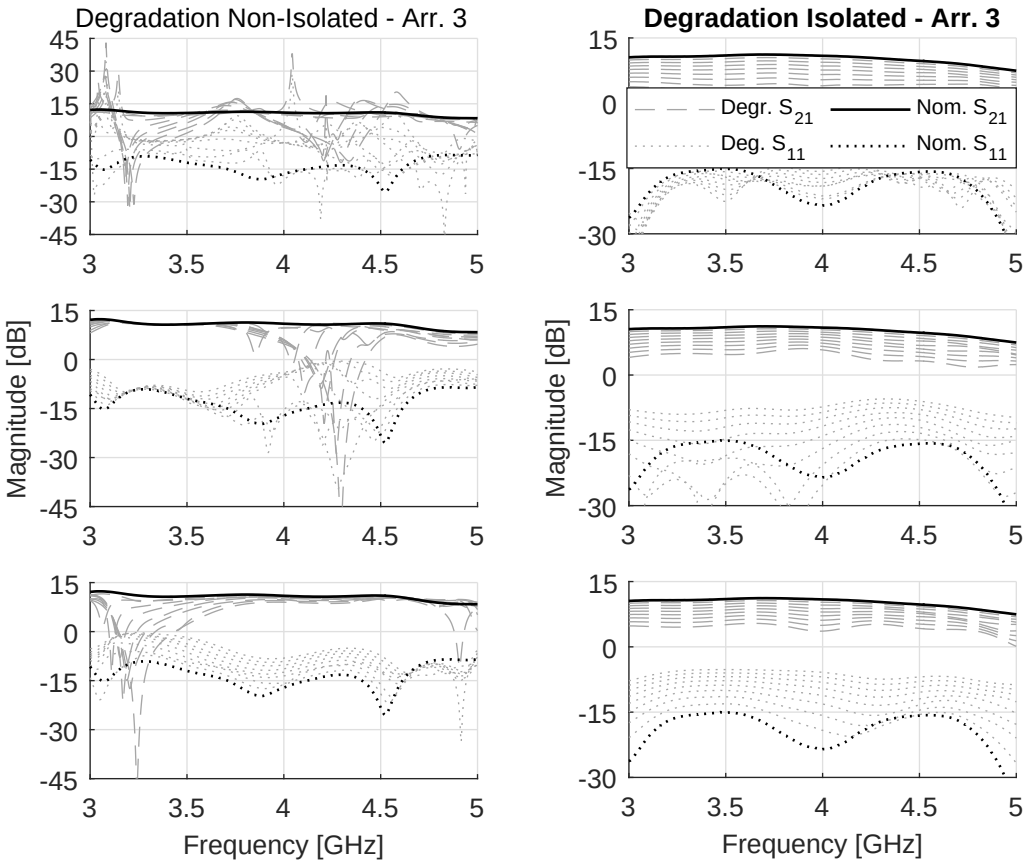

Figure A.10: Broadband output magnitude degradation performance of the (a) non-isolated and (b) isolated combiner setups, using real amplifier S-parameters, for faults spaced as symmetrically as possible. From top to bottom: 0-dB through, short and open circuit faults.

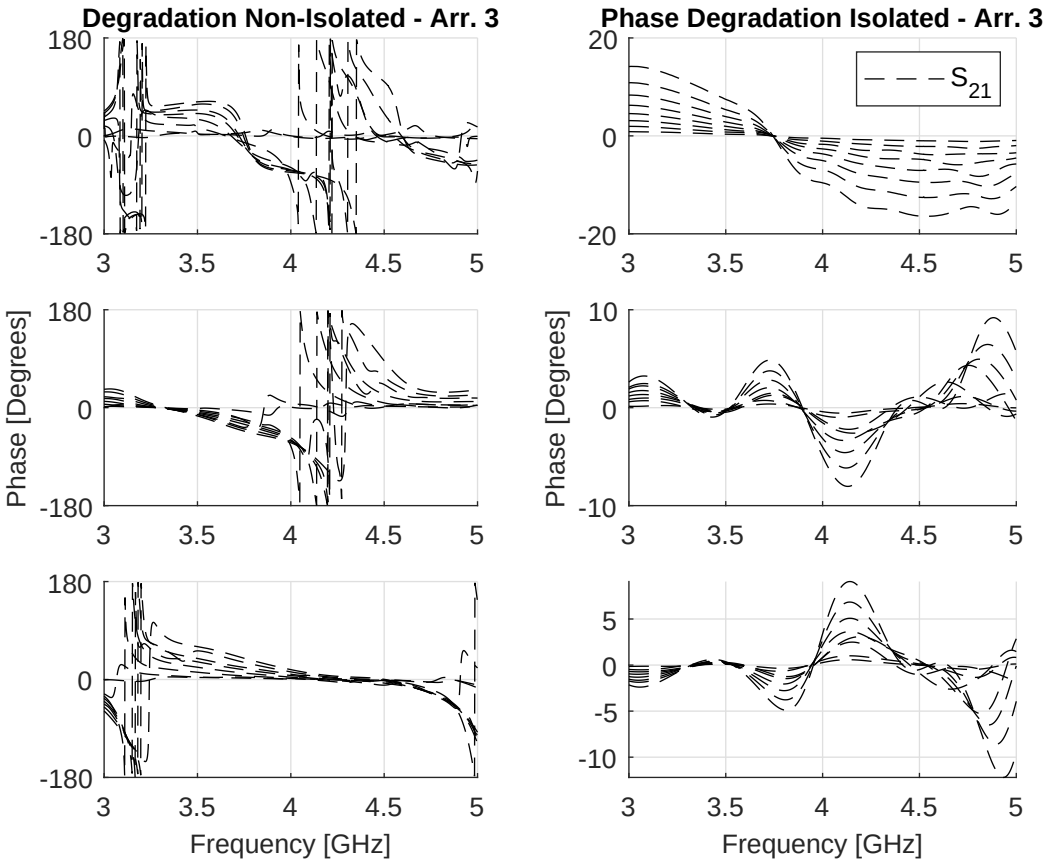

(a) (b)

Figure A.11: Broadband output phase degradation performance of the (a) non-isolated and (b) isolated combiner setups, using real amplifier S-parameters, for faults spaced as symmetrically as possible. From top to bottom: 0-dB through, short and open circuit faults.

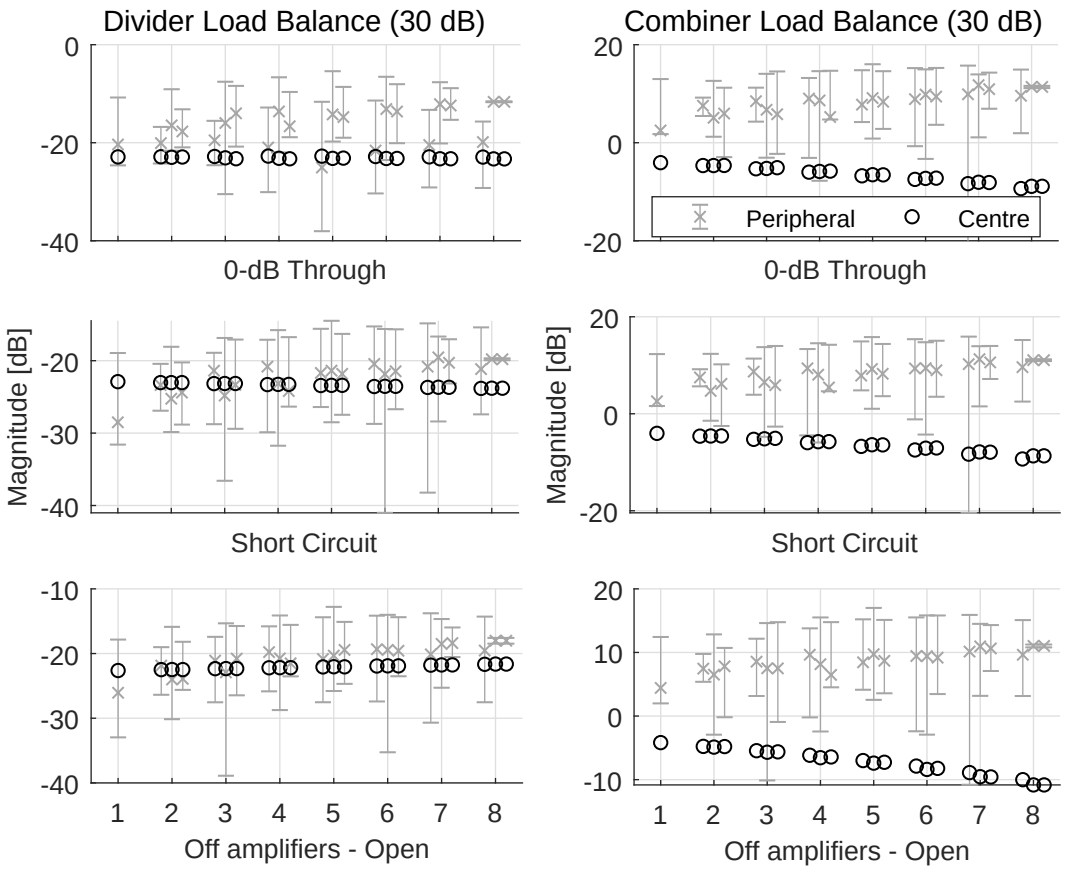

(a) (b)

Figure A.12: Power dissipated in the isolation loads of the (a) divider and (b) combiner with 30 dB gain per amplifier. The errorbars show the minimum and maximum per fault case, and the markers indicate the median values.

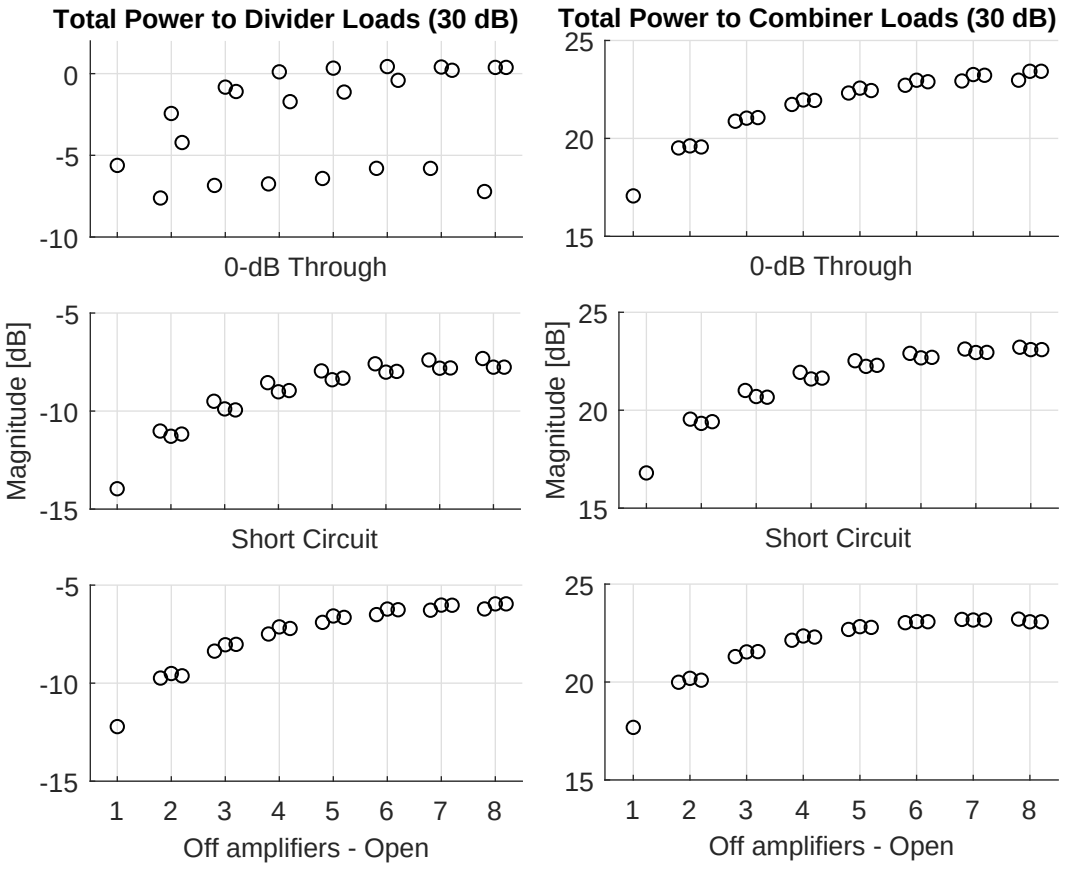

Figure A.13: Total power dissipated in the peripheral isolation loads of the (a) divider and (b) combiner with 30 dB gain per amplifier.

Bibliography

[1] E. J. Wilkinson, "An N-way Hybrid Power Divider", *IEEE Transactions on Microwave Theory and Techniques*, vol. 8, no. 1, pp. 116–118, 1960.

[2] S. Tsitsos, H. Anastassiu, and A. Papatsoris, "3-way Wide-Band Planar Power Divider", in *22nd Telecommunications Forum (TELFOR)*, Belgrade, Serbia, Nov. 2014, pp. 629–632.

[3] U. H. Gysel, "A New N-way Power Divider/Combiner Suitable for High-Power Applications", in *IEEE-MTT-S International Microwave Symposium*, Palo Alton, CA, USA, May 1975, pp. 116–118.

[4] F. Ardemagni, "An Optimized L-Band Eight-Way Gysel Power Divider-Combiner", *IEEE Transactions on Microwave Theory and Techniques*, vol. 31, no. 6, pp. 491–495, 1983.

[5] M. Jobs, D. Dancila, J. Eriksson, and R. Ruber, "An 8-1 Single-Stage 10-kW Planar Gysel Power Combiner at 352 MHz", *IEEE Transactions on Components, Packaging and Manufacturing Technology*, vol. 8, no. 5, pp. 851–857, 2018.

[6] M. M. Fahmi, J. A. Ruiz-Cruz, and R. R. Mansour, "Compact Ridge Waveguide Gysel Combiners for High-Power Applications", *IEEE Transactions on Microwave Theory and Techniques*, vol. 67, no. 3, pp. 968–977, 2019.

[7] H. Fan, X. Liang, J. Geng, L. Liu, and R. Jin, "An N-Way Reconfigurable Power Divider", *IEEE Transactions on Microwave Theory and Techniques*, vol. 65, no. 11, pp. 4122–4137, Nov. 2017.

[8] C. Tang and Z. Hsieh, "Design of a Planar Dual-Band Power Divider With Arbitrary Power Division and a Wide Isolated Frequency Band", *IEEE Transactions on Microwave Theory and Techniques*, vol. 64, no. 2, pp. 486–492, 2016.

[9] X. Wang, K. Wu, and W. Yin, "A Compact Gysel Power Divider With Unequal Power-Dividing Ratio Using One Resistor", *IEEE Transactions on Microwave Theory and Techniques*, vol. 62, no. 7, pp. 1480–1486, 2014.

[10] M. D. Abouzahra and K. C. Gupta, "Multiport Power Divider-Combiner Circuits Using Circular-Sector-Shaped Planar Components", *IEEE Transactions on Microwave Theory and Techniques*, vol. 36, no. 12, pp. 1747–1751, 1988.

[11] K. Song, S. Hu, F. Zhang, and Y. Zhu, "Four-way Chained Quasi-Planar Power Divider Using Rectangular Coaxial Waveguide", *IEEE Microwave and Wireless Components Letters*, vol. 25, no. 6, pp. 373–375, 2015.

[12] D. Akinwande and I. Martinez-Garcia, "The superplanar combiner: A novel parallel combiner and divider", in *Proceedings 57th Electronic Components and Technology Conference*, Reno, NV, USA, May 2007, pp. 154–157.

[13] F. Fan, W. Wang, and Z. Yan, "A novel 1:19 microstrip radial power divider design for the application in antenna array", in *International Workshop on Microwave and Millimeter Wave Circuits and System Technology*, Chengdu, China, Oct. 2013, pp. 17–19.

[14] A. E. Fathy, S. W. Lee, and D. Kalokitis, "A Simplified Design Approach for Radial Power Combiners", *IEEE Transactions on Microwave Theory and Techniques*, vol. 54, no. 1, pp. 247–255, 2006.

[15] P. Jia and R. A. York, "A Compact Coaxial Waveguide Combiner Design for Broadband Power Amplifiers", in *IEEE MTT-S International Microwave Sympsoium Digest*, vol. 1, Phoenix, AZ, USA, May 2001, 43–46 vol.1.

[16] R. D. Beyers and D. I. L. de Villiers, "A General Impedance Tapered Transition for N-way Conical and Coaxial Combiners", *IEEE Transactions on Microwave Theory and Techniques*, vol. 64, no. 12, pp. 4482–4490, 2016.

[17] Q. Wang, Y. Ning, Y. Zhang, W. Jiang, J. Liu, and W. Zhu, "Ultra-Wideband 20-way Coaxial Power Combiner", in *IEEE 6th International Symposium on Microwave, Antenna, Propagation, and EMC Technologies (MAPE)*, Shanghai, China, Oct. 2015, pp. 495–499.

[18] D. I. L. de Villiers, P. W. van der Walt, and P. Meyer, "Design of a Ten-way Conical Transmission Line Power Combiner", *IEEE Transactions on Microwave Theory and Techniques*, vol. 55, no. 2, pp. 302–308, 2007.

[19] V. Zavodny and M. Dvorsky, "16-Port Power Combiner", in *Conference on Microwave Techniques (COMITE)*, Brno, Czech Republic, Apr. 2017.

[20] G. L. Huang, S. G. Zhou, and T. H. Chio, "A Compact Wideband 16-way Power Combiner Implemented via 3-D Metal Printing", in *IEEE 5th Asia-Pacific Conference on Antennas and Propagation, Conference Proceedings*, Kaohsiung, Taiwan, Jul. 2017, pp. 51–52.

[21] H. J. Riblet, "The Short-Slot Hybrid Junction", *Proceedings of the IRE*, vol. 40, no. 2, pp. 180–184, 1952.

[22] R. D. Beyers and D. I. L. de Villiers, "A General Isolation Network for N-way Power Combiners/Dividers", in *IEEE MTT-S International Microwave Symposium*, Phoenix, AZ, USA, May 2015.

[23] C. H. Tseng and Y. C. Hsiao, "A New Broadband Marchand Balun Using Slot-Coupled Microstrip Lines", *IEEE Microwave and Wireless Components Letters*, vol. 20, no. 3, pp. 157–159, 2010.

[24] H. J. du Toit, D. I. L. de Villiers, and R. D. Beyers, "A Simple Low Loss Partially-Filled 16-way Radial Power Combiner", in *IEEE MTT-S International Microwave Symposium (IMS)*, Boston, MA, USA, Jun. 2019, pp. 440–443.

[25] H. J. du Toit and D. I. L. de Villiers, "A Fully Isolated 16-way Radial Power Combiner", *submitted, IEEE Transactions on Microwave Theory and Techniques*, 2019.

[26] Z. Yin, Z. Shao, L. Liu, and X. Zhu, "Design of a Novel Broadband Power Divider Based on Oversized-Coaxial and Radial Waveguide", in *International Conference on Computational Problem-Solving*, Chengdu, China, Oct. 2011, pp. 255–257.

[27] S. H. Lee, D. H. Lee, and J. H. Chang, "X-band 1kW SSPA Using 20-way Hybrid Radial Combiner for Accelerator", in *Asia-Pacific Microwave Conference Proceedings, APMC*, New Delhi, India, 2017.

[28] R. Kazemi, G. Hegazi, and A. E. Fathy, "X-band All-waveguide Radial Combiner for High Power Applications", in *IEEE MTT-S International Microwave Symposium (IMS)*, Phoenix, AZ, USA, 2015.

[29] R. C. Allison, R. L. Eisenhart, and P. T. Greiling, "A Matched Coaxial-Radial Transmission Line Junction", in *IEEE-MTT-S International Microwave Symposium Digest*, Ottawa, ON, Canada, Jun. 1978, pp. 44–46.

[30] E. Belohoubek, R. Brown, H. Johnson, A. Fathy, D. Bechtle, D. Kalokitis, and E. Mykietyn, "30-way Radial Power Combiner for Miniature GaAs FET Power Amplifiers", in *IEEE MTT-S International Microwave Symposium Digest*, Baltimore, MD, USA, Jun. 1986, pp. 515–518.

[31] C. Rave and A. F. Jacob, "A Wideband Radial Substrate Integrated Power Divider at K-band", in *German Microwave Conference*, Nuremberg, Germany, Mar. 2015, pp. 84–87.

[32] S. M. Roy, I. Balbin, and N. C. Karmakar, "Novel N-way Power Divider and Array Configuration for RFID Readers Operating at 5.8 GHz", in *IEEE International Conference on RFID*, Las Vegas, NV, USA, Apr. 2008, pp. 89–96.

[33] X. Li, G. Chen, M. Zhan, and R. Xu, "A New Planar Compatible Power Combiner Based on Radial Waveguide", in *IEEE International Conference on Communiction Problem-Solving*, Beijing, China, Dec. 2014, pp. 147–149.

[34] K. Song, Y. Fan, and Z. He, "Broadband Radial Waveguide Spatial Combiner", *IEEE Microwave and Wireless Components Letters*, vol. 18, no. 2, pp. 73–75, 2008.

[35] Y. He and Q. Chu, "A Ka-band Radial Power-Combiner with Broadband Probes and Resistive Slots", in *IEEE International Workshop on Electromagnetics: Applications and Student Innovation Competition (iWEM)*, Nanjing, China, May 2016, pp. 1–2.

[36] X. Shan and Z. Shen, "A Suspended-substrate Ku-band Symmetric Radial Power Combiner", *IEEE Microwave and Wireless Components Letters*, vol. 21, no. 12, pp. 652–654, 2011.

[37] S. B. Erekson, W. J. D. Johnson, and D. Peroulis, "Design of an Airline Coax Radial Power Combiner with Enhanced Isolation", in *IEEE MTT-S International Microwave Symposium (IMS)*, Honololu, HI, USA, Jun. 2017, pp. 455–458.

[38] C. Haifeng and Z. Bin, "A Design of C-band Improved Radial Power Combiner", in *9th International Conference on Solid-State and Integrated Circuits Technology Proceedings, ICSICT*, vol. 1, Beijing, China, 2008, pp. 1415–1417.

[39] M. H. Chen, "A 19-Way Isolated Power Divider Via the TE_{01} Circular Waveguide Mode Transition", in *IEEE MTT-S International Microwave Symposium Digest*, Baltimore, MD, USA, USA, Jun. 1986, pp. 511–513.

[40] Q. X. Chu, D. Y. Mo, and Q. S. Wu, "An Isolated Radial Power Divider via Circular Waveguide TE_{01}-Mode Transducer", *IEEE Transactions on Microwave Theory and Techniques*, vol. 63, no. 12, pp. 3988–3996, 2015.

[41] T.-H. Chio, G.-L. Huang, and S.-G. Zhou, "Application of Direct Metal Laser Sintering to Waveguide-Based Passive Microwave Components, Antennas, and Antenna Arrays", *Proceedings of the IEEE*, vol. 105, no. 4, pp. 632–644, 2017.

[42] R. D. Beyers, "Circuit Model Design of Conical Transmission Line Power Combiners and Isolation of Reactive Combiners", PhD thesis, Stellenbosch University, 2015.

[43] G. R. Simpson, "A Generalized n-Port Cascade Connection", in *IEEE MTT-S International Microwave Symposium Digest*, Los Angeles, CA, USA, Jun. 1981, pp. 507–509.

[44] A. A. M. Saleh, "Theorems on Match and Isolation in Multiport Networks (Short Papers)", *IEEE Transactions on Microwave Theory and Techniques*, vol. 28, no. 4, pp. 428–429, 1980.

[45] D. I. L. de Villiers, "Analysis and Design of Conical Transmission Line Power Combiners", PhD thesis, Stellenbosch University, 2007.

[46] C. A. Balanis, *Advanced Engineering Electromagnetics*. Hoboken, NJ, USA: John Wiley & Sons, Inc., 1989.

[47] N. Marcuvits, Ed., *Waveguide Handbook*. New York, USA: Dover Publications, Inc., 1965.

[48] S. Ramo, J. Whinnery, and T. Van Duzer, *Fields and Waves in Communication Electronics*. Hoboken, NJ, USA: John Wiley & Sons. Inc., 1994.

[49] Dassault Systèmes, CST Studio Suite, 2019. [Online]. Available: `https://www.3ds.com/products-services/simulia/products/cst-studio-suite/` (visited on Nov. 22, 2019).

[50] Huber+Suhner AG, *RF Coaxial Connectors - General Catalogue*. [Online]. Available: `http://literature.hubersuhner.com/Technologies/Radiofrequency/RFConnectorsEN/` (visited on Nov. 22, 2019).

[51] AGC-Nelco, *Mercurywave ® 9350, RF and Microwave Laminate and Prepreg*. [Online]. Available: `https://agc-nelco.com/products/mercurywave-9350/` (visited on Nov. 22, 2019).

[52] T. Tanaka, K. Tsunoda, and M. Aikawa, "Slot-Coupled Directional Couplers Between Double-Sided Substrate Microstrip Lines and Their Applications", *IEEE Transactions on Microwave Theory and Techniques*, vol. 36, no. 12, pp. 1752–1757, 1988.

[53] National Instruments, AWR, 2019. [Online]. Available: `https://www.awr.com/` (visited on Nov. 22, 2019).

[54] R. L. Ernst, R. L. Camisa, and A. Presser, "Graceful Degradation Properties of Matched N-Port Power Amplifier Combiners", in *IEEE MTT-S International Microwave Symposium Digest*, San Diego, CA, USA, Jun. 1977, pp. 174–177.